UNIVERSITY OF COPENHAGEN
FACULTY OF SCIENCE

M.Sc. Thesis

Modelling of Thouless pumping in one dimensional Josephson junction arrays

Stavros Athanasiou

Supervision: Michele Burrello and Matteo Michele Wauters

June 21, 2023

"When you change the way you look at things, the things you look at change."

Max Planck,
The Father of Quantum Physics

Acknowledgements

I would like to express my deepest gratitude to my advisors Assoc. Prof. Michele Burrello and Dr. Matteo Wauters for their invaluable guidance, constant support and continuous encouragement throughout the entire duration of this thesis project. Their expertise, patience and insightful feedback have been essential in shaping the direction and quality of this project.

I am thankful to colleagues and fellow researchers from both the theoretical and experimental sectors of the Center for Quantum devices, for engaging in intellectual discussions and collaborations. Their shared enthusiasm has greatly enhanced the enjoyment of this journey.

I am deeply grateful to my family for their unconditional love, the endless and constant support and the encouragement, not only during the completion of this thesis but throughout my entire career and life. Their presence and belief in me have been invaluable.

Finally, I am grateful to my beloved, with whom I share not only my happiest moments but also my most challenging ones. Her support was immense and unwavering.

Thank you all for being an integral part of this incredible journey.

Abstract

This thesis focuses on analog quantum simulation, specifically studying topological quantum pumping in a superconducting network known as the Josephson junctions array. The Josephson junctions array provides a versatile and highly tunable platform for simulating quantum many-body phenomena. The main objective of this study is to investigate topological pumping in the presence of external superconducting leads.

In condensed matter physics, one way of studying quantum many-body phenomena and emergent collective behaviors is through the use of analog devices. Our study specifically explores the analog quantum simulation of topological quantum pumping in a Josephson junctions array. The choice of superconducting networks is motivated by their tunability and the research orientations of the Center for Quantum Devices. The thesis investigates the implementation of the Rice-Mele model, one of the simplest examples of Thouless pumping, on the Josephson junctions array, which becomes possible by exploiting the quantum limit $E_{C_0} \gg E_{J_0}$ and the hardcore boson approximation. The study showcases the underlying mechanisms of quantized pumping in the Rice-Mele model with periodic boundary conditions through Berryology and Floquet theory. The quantization of particle transport is expressed in terms of the Chern number and/or equivalently as the nontrivial winding of the Floquet band over the Floquet-Brillouin zone. The influence of various effects such as finite size effects, nonadiabaticity and disorder on the quantized current is also explored.

The investigation extends to studying pumping in the presence of external superconducting leads. The presence of the superconducting phase difference is accounted for by establishing a connection to twisted boundary conditions. The study demonstrates that transport is quantized when the winding of the many-body quasienergy over the Floquet-Brillouin zone, as the superconducting phase difference varies, is nontrivial. The quantization remains robust against disorder and nearest-neighbor interactions for specific parameter choices. The thesis also discusses the potential for future research, including the exploration of other models, relaxation of assumptions, and the inclusion of next-nearest-neighbor interactions.

In conclusion, this thesis contributes to the understanding of topological quantum pumping in the context of the Josephson junctions array. The study reveals the robustness of quantization against disorder and the influence of the superconducting phase difference on the system's evolution. The findings open up possibilities for further research in different system conditions and the validation of approaches used for external leads. Overall, this work highlights the potential of analog quantum simulation for studying quantum many-body phenomena.

Contents

List of Figures

Chapter 1

Introduction

'...nature isn't classical ..., and if you want to make a simulation of nature, you'd better make it quantum mechanical, and by golly it's a wonderful problem, because it doesn't look so easy...'

Richard Feynman, 1981

The simulation of quantum many-body systems is considered to be a difficult computational task [1], especially if done with classical means. It becomes a real challenge when dealing with large-sized and strongly interacting systems, which require a large amount of memory to store quantum states, growing exponentially with the system size. In addition, this also means that the computational time grows at this trend. In the case of strong correlations, even the most elaborate classical computers fail to do the task [2]. Feynman proposed a different approach to this problem: '..let the computer itself be built of quantum mechanical elements which obey quantum mechanical laws' [3], in accordance to his statement above. Let us talk then about quantum simulations!

There are two forms of quantum simulations, digital and analog. The former correspond to programmable, general purposed quantum devices [2]. We can think of them as the quantum 'version' of a classical computer, in which the classical bits are replaced by elements of quantum nature, the qubits. An important feature of a digital quantum computer is that it has to be universal, promising great flexibility on the models to be solved. In contrast, analog quantum simulations [1] are problem-specific machines. Analog devices are typically highly controllable platforms, which are able to mimic the dynamical evolution or properties of the original system. The interest on quantum simulation has been grown the last couple of decades, primarily because the domain of application is wide [1], involving scientific areas such as low-energy physics, high-energy physics, chemistry etc, and secondly because of the technological advancements, making the fabrication of devices accessible and straighforward.

In condensed matter physics, we are interested in studying quantum many-body phenomena and emergent collective behaviors with unique and intriguing features. Typical analog devices used for this cause, among others are ultra-cold atoms in optical lattices [4, 5], photonics [6], solid-state devices with quantum dots [7, 8] and superconducting circuits [9, 10, 11].

In the current work, we focus on analog quantum simulation of a phenomenon called **topological quantum pumping** [12] in a superconducting network, the **Josephson**

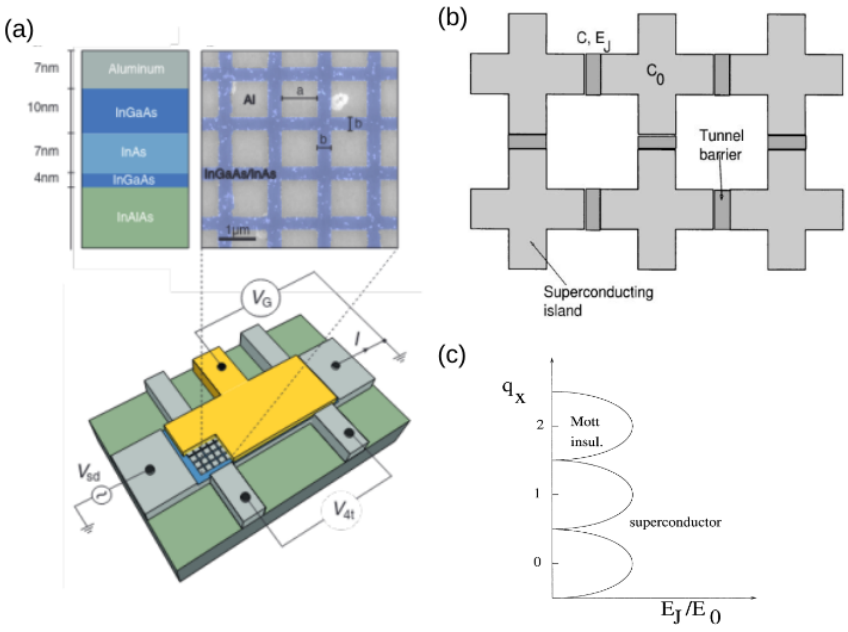

Figure 1.1: Josephson junctions array (JJA) (a) The experimental setup of realizing a 2D JJAs, showing the layers of the heterostructure used for the device. The superconducting islands are fabricated in the shape of a square. Adapted from [14] (b) A sketch of a 2D superconducting network. Adapted from [15] (c) The phase diagram of the tunable parameters of a JJA, q_x (induced charge - associated with the charging Hamiltonian) and E_J/E_{C_0} (ratio between the Josephson and charging energy). Adapted from [10].

junctions array [13]. The focus on superconducting networks is inspired by the research orientations of the Center for Quantum Devices, where they realize such devices [14]. These systems are currently under development, aiming to achieve the ability to fine-tune individual junctions rather than entire arrays. Moreover, the incorporation of external superconducting leads allows for current measurements for transport purposes and maintains the coherent dynamical evolution of the system. Indeed, tunability, coherence and the ability to investigate transport are three key features of these systems.

In the subsequent sections, we delve into the two central themes of this thesis: Josephson junction arrays and topological quantum pumping. Additionally, we provide an outline of the thesis.

1.1 Josephson junctions arrays

In the context of analog quantum simulations, the engineering of systems with a high degree of tunability is crucial. Quantum devices emerge as strong candidates for achieving this goal. Such devices allow the experimentalist to indirectly control the parameters of the target system, enabling the capability of studying the physics of the system in various regimes. In particular, hybrid semiconducting-superconducting devices represent a versatile platform that merges the advantages of superconducting systems, such as coherence, with the strengths offered by semiconductors, such as control via electrostatic gates.

Superconducting networks have in particular drawn most of the attention. A prominent example is the Josephson junctions array [16] (see Figure 1.1b), first established in the early 1980s [13], with the prospect of realizing electronic devices with superconducting materials.

From that point onward, such devices were greatly used for simulating many-body systems in both the classical and quantum regimes [10, 11, 14], at a mesoscopic level.

Originally, such superconducting networks were built on insulating substrates, and lacked the tunability to be proper simulators. Hybrid semiconducting-superconducting devices represent the modern iterations of such systems [17], the fabrication of which involves the deposition of aluminum on a semiconducting substrate. Then the aluminum is etched to form the superconducting islands, in some periodic formation (for instance see Figure 1.1a). In principle, the superconducting islands and the Josephson junctions can be both tuned by individual voltage gates. In practice, this can be cumbersome for large devices, however today one can employ machine learning algorithms to achieve this individual tuning [18].

In the regime where superconductivity is well-established $T \ll T_c$, there are two characteristic energy scales in a Josephson junctions array, the charging energy E_{C_0} and the Josephson energy E_{J_0}. The charging energy of the system is typically determined by its geometry and cannot be easily adjusted. In contrast, the Josephson energy can be controlled using voltage gates, which depletes the semiconducting regions between superconductors. By adjusting the ratio of the two, one can exploit different physical regimes, thus different phases and properties (see Figure 1.1c). On one hand, the classical regime is obtained when $E_{J_0} \gg E_{C_0}$, in which the phase fluctuations are suppressed and a global phase coherence is established, corresponding to a superconducting phase. In the opposite limit, we have the quantum limit $E_{C_0} \gg E_{J_0}$; this limit corresponds to strong phase fluctuations and thus well-defined particle number, ultimately resulting in the formation of a Mott insulating phase. However, for special values of the chemical potential the Mott lobes may vanish even in the strong charging energy limit - see Figure 1.1c.

Although significant progress has been made in the fabrication of these devices, we expect disorder to be present. Therefore, to establish these hybrid platforms as a novel architectures for analog quantum simulations, it is interesting to design systems that display phenomena robust against disorder. Due to this reason, Thouless pumping is explored in this work; being a topological phenomenon it is expected to display a certain robustness against disorder. In practical terms, the implementation of Thouless pumping can turn an insulating systems as the JJA in the quantum limit with weak disorder, into a superconducting system, characterized by coherent and quantized transport of Cooper pairs.

1.2 Thouless pumping

One of the simplest, yet intriguing phenomena to study is the topological quantum pump [12].

Naturally, when we think about the notion of pumping, our minds associate it with some physical process that we have seen or interacted with in the real world. Take for instance the famous Archimedean screw (see Fig. 1.2a), which was used to pump water from low-lying areas to high ones by turning a screw [1]. Admittedly, however, the quantum 'version' of the pump is a bit more intriguing. The example of Figure 1.2b provides an insight into the idea of quantum pumping, in which we pump exactly N electrons after a pumping period.

[1] Remarkably, despite advances in technology, the concept remains highly applicable today.

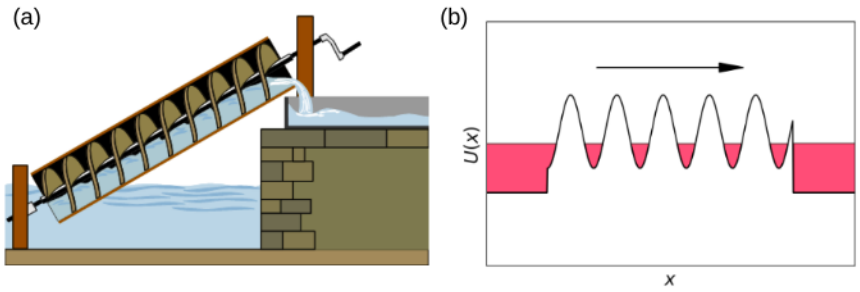

Figure 1.2: Classical pump and the 'quantum' version. (a) The classical water pump of Archimedes, used to transfer water from low-lying areas up to high ones. The water was technically pumped by turning a screw-shaped surface inside the pipe. Adapted from [20]. (b) A sinusoidal confining potential is applied to a 1D system coupled to two electrodes on both sides (and no external bias). Under certain conditions ('high' enough confining potential and low chemical potential compared to that height such that N electrons are confined in each trough), we pump N electrons per driving period. Adapted from [21].

In general, a quantum pump is defined as a device in which a particle current is generated by slowly modulating the parameters of the system, without having an external bias [19]. In contrast, in usual mesoscopic transport, a system is connected to external leads, with some non-zero voltage bias across to allow for a particle current to flow. The topological quantum pump is device in which the induced particle current (in units of the particle charge) is quantized by an integer number. This number is linked to the underlying nontrivial topology of the system and corresponds to the first Chern number of the occupied dynamical bands, parametrized by (k, t).

By establishing the topological quantum pump, we have admitted ourselves into a new realm of physical phenomena, systems possessing a nontrivial topological structure. Topological properties have been understood within the framework of the geometrical theory of Berry [22], who showed that a quantum mechanical phase can have physical implications.

The introduction of topology in condensed matter physics and the association of some observables of the system with a topological invariant is by itself very powerful [23], especially for practical applications. It has been demonstrated that in such systems these observables are robust against local perturbations such as disorder [24] [25], as long as the energy gap remains open [2] (see Fig. 1.3a). The initial surge of these promising discoveries captivated a significant portion of the scientific community, leading to a widespread interest in the study of these systems. The prospect of incorporating such systems into building a quantum computer is far from random.

The topological quantum pump adopts some of these features, like topologically protected observables and robustness against perturbations. David Thouless first introduced the notion of a topological pump, also referred to as Thouless pumping, for a one-dimensional band insulator in the **thermodynamic limit**, in which the potential is varied **periodically in time**, in an **adiabatic manner** and the **Fermi level lies within the energy gap** at all times.. He showed that the resulting pumped charge per period is quantized in terms of the first Chern number, exploiting the geometry of the induced 2D Brillouin-zone of (k, t). It was shown later that the quantized pumped charge is linked to the Berry phase acquired by the state after the

[2] In dynamical systems like Thouless pumping, the significant gap refers to the minimum gap observed throughout the evolution.

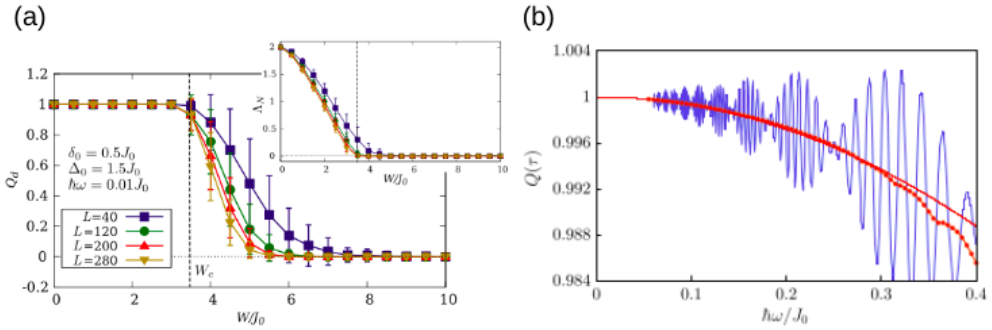

Figure 1.3: Consequences of disorder and driving with finite speed on pumping. (a) The pumped charge is quantized for weak disorder, as long as the energy gap remains opens. When the latter is violated, then quantized transport ceases. Adapted from [27]. (b) The pumped charge as a function of the driving frequency. As the driving frequency grows, the quantized value of 1 is affected by ω^2 and sinusoidal corrections. Adapted from [28].

time evolution of a single period [3] [26]. Equivalently, the pumped charge can be expressed as the integral of the Berry curvature (of occupied bands) over the Brillouin zone formed by (k, t). The latter has the geometry of a torus and proper integration of the Berry curvature - of the filled bands - over the surface is equal to a topological invariant named the Chern number and it is an integer number. This statement corresponds to the physical implementation of the Gauss-Bonnett-Chern theorem [4]. We will revisit this topic in Chapter 4.

Typically, in a two-dimensional band insulator (like in the case of the quantum Hall effect), one expects that quantities such as the linear response to an external electric field, are written in terms of the Chern number obtained by the integral of the Berry curvature of occupied bands over the two-dimensional Brillouin zone formed by (k_x, k_y) [23]. Therefore, Thouless pumping is sometimes referred to as the dynamical version of the 2D quantum Hall effect.

Thouless pumping is realized under the conditions of adiabaticity and the Fermi level lying in the energy gap (the gap between occupied and unoccupied bands), as well as the thermodynamic limit. Adiabaticity requires that the energy gap is much larger than the driving frequency to avoid particle-hole excitations, and thus start populating the higher bands. Away from the adiabatic limit $\omega \to 0$, deviations from perfect quantization start to appear (see Fig. 1.3b), because of non-adiabatic corrections [28]. The thermodynamic limit is necessary for the Chern number to be defined, however, in practice one is concerned with finite-size systems. Typically, we can choose a system size large enough to mimic the effects of the thermodynamically infinite system, apart from some minor corrections.

The simplest example, resembling an adiabatic charge pump, is the time-dependent version of the Rice-Mele model [29], a tight-binding model, with staggered on-site potential forming two sublattice types. It requires the time modulation of the hopping parameters and the staggered potential under some proper protocol that leads to a quantized current. This follows the guidelines set by Thouless's pioneering work on adiabatic pumps.

[3] This is exactly a consequence of the Berry theory, in which the Berry phase can have physical consequences, rather than being just a phase.

[4] The Gauss-Bonnett-Chern theorem states that integration of the Gaussian curvature over the surface of some manifold of 2N dimension is expressed in terms of the genus (roughly, the number of holes). It is the generalization of the Gauss-Bonnett theorem, which is limited only to 2D manifolds.

Thouless pumping is considered the first example of a topological phase that emerges from a periodically driven system, hence its significance is great. By understanding the underlying mechanisms, this finding opens the portal towards topological nonequilibrium phases of matter, with remarkable features. It is noteworthy that by driving a system periodically in time, we can access exotic out-of-equilibrium phases of matter that may have or not static counterparts [5]. The Floquet theory is greatly employed to understand the underlying mechanisms of the system.

1.3 Outline of this thesis

This work is focused on the theoretical realization of the Rice-Mele model, the simplest example of a Thouless pump, in a one-dimensional Josephson junctions array, connected to external, superconducting leads. The conditions under which quantized transport takes place are examined.

Firstly, in Chapter 2 we present the theoretical model of the Josephson junctions array, and we discuss the mapping of the JJA Hamiltonian to the Rice-Mele one by virtue of the hardcore boson approximation. This is in fact the principle behind analog quantum simulation. Ultimately, the resulting quadratic Hamiltonian is mapped from a bosonic description to a free fermionic one via the Jordan-Wigner transformation. This transformation establishes the form of the time-dependent Rice-Mele model.

Before delving into the physics of pumping, in Chapter 3 we introduce concepts from the Floquet theory that are instrumental in understanding the mechanism of pumping. We also discuss the mapping from a dynamical to an effective static system. Additionally, we explore the phenomenon of pumping within the framework of Floquet theory.

In Chapter 4, we discuss the physics of the Rice-Mele model and the conditions under which we observe quantized transport, such as half-filling, adiabaticity and finite size effects. We view the quantization from the Berry and Floquet perspectives, which in the adiabatic limit are equivalent.

In Chapter 5, we add static, on-site disorder to the Rice-Mele model. We study the breakdown of pumping and the disorder-driven phase transition to an insulating phase, using diagnostic tools such as the local Chern marker and the strange correlation function. These require the mapping to an effective two-dimensional static problem and it is done in the context of the Floquet theory. Unexpectedly, we observe the breakdown of the strange correlation function in the strong disorder regime.

In Chapter 6, we introduce the superconducting leads in the setup. The Hamiltonian now depends on the phase difference between the external leads and we study how a quantized current is obtained. Importantly, the transferred charge requires a phase average, however we find a sweet spot in the parameters choice in which the transferred charge does not require phase averaging for finite system size. On this basis, we include disorder and nearest neighbour interactions, in which we observe a notable robustness.

Lastly, we present our final thoughts and findings in Chapter 7.

[5] Such examples are Floquet topological insulators [30], tha anomalous Floquet insulators [31] and systems in a many-body localization phase, which under periodic driving do not thermalize [32]

Chapter 2

Josephson junctions array and the mapping to the Rice-Mele model

In Chapter 1, we have introduced the Josephson junctions array, an experimenal platform to simulate many-body systems at the mesoscopic level. The basic idea of analog quantum simulations lies on the fact that one can start from the Hamiltonian of the mesoscopic system, and using proper arguments, this can be mapped to the target model, the one we are interested in simulating. The other important element is to be able to tune the physical parameters of the system in the considered device. In the JJA, this is indeed crucial to obtain the time modulation of the parameters one needs for the Rice-Mele model. Thus, in this chapter we present the Hamiltonian of a one-dimensional Josephson junctions array, and we show how one can obtain the Hamiltonian of the Rice-Mele model in the hardcore bosonic limit. Notably, the mapping to free fermions is achieved by the Jordan-Wigner transformation. The discussion of the properties of the Rice-Mele model is left for Chapter 4.

2.1 The Quantum Phase Model

Josephson junctions arrays (JJA) consist of superconducting islands, of the conventional BCS type. The islands are arranged periodically, such as in a 1D or 2D square array. Typically, we are interested in the physics of this system in temperatures way below the critical BCS temperature, at which the superconducting gap has been fully developed and thus the quasiparticle excitations are suppressed. As a result, only Cooper pairs are allowed to move freely. A sketch of a 1D superconducting network is displayed in Figure 2.1.

Each superconducting island is characterized by its own phase operator $\hat{\varphi}_i$ and its conjugate variable, the particle number operator $\hat{N}_i$. In the context of the coherent states theory, the aforementioned operators satisfy the following commutation relation:

$$\left[\hat{N}_i, \hat{\varphi}_j\right] = i\delta_{ij} \tag{2.1.1}$$

In a BCS superconductor, the state of the system corresponds to a coherent state $|BCS\rangle$, with a well-defined phase [1]. Thus, the particle number is maximally undetermined given the uncertainty relation arising from the commutation relation of 2.1.1.

Cooper pairs are allowed to hop to adjacent islands via a Josephson junction. In experimental setups, the supeconducting islands are fabricated on a semiconducting substrate,

[1] The phase symmetry is broken in the superconducting phase, establishing a unique, well-defined phase for a particular state.

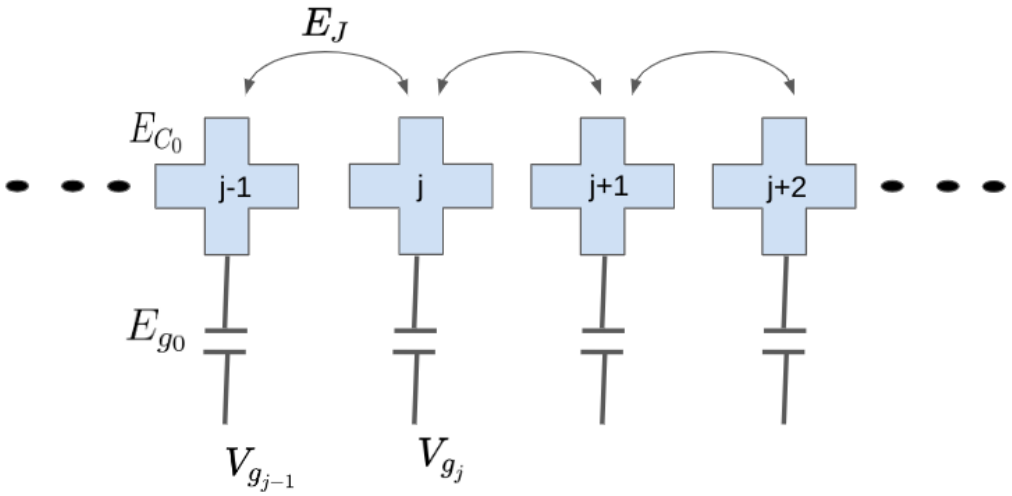

Figure 2.1: A sketch of a one-dimensional array of Josephson junctions. The superconducting islands are represented by a cross shape. E_J is the Josephson energy associated with the hopping of Cooper pairs between islands while V_{g_j} is the gate voltage of the island, and by adjusting it we can access specific states. The charging energy E_{C_0} is the energy required to add a Cooper pair on the island, and E_{g_0} is the energy associated with the island-gate capacitance, discussed in the text.

and the junction is of the SNS (superconductor-normal-superconductor) type. The energy associated with the effect is given by the Beenakker formula [33], valid for $T \ll T_c$.

$$E(\phi) = \sum_i \Delta_0 \sqrt{1 - t_i \sin^2(\phi/2)} \tag{2.1.2}$$

where Δ_0 is the superconducting gap, t_i are the transmission coefficients of the SN interface for an Andreev state, and ϕ is the superconducting phase difference of the involved superconductors. It is assumed that tunneling of Cooper pairs occurs through the Andreev process. The summation index i runs over the number of channels corresponding to Andreev states. We recover the familiar cosine form if we assume that the transmission coefficient , which is associated with a superconductor-insulator interface, is small, i.e. $t_i \ll 1$,

$$E(\phi) \approx \frac{\Delta_0 t}{4} \cos\varphi \tag{2.1.3}$$

where $t = \sum_i t_i$. For a one-dimensional array of Josephson junctions and in second quantization, the contribution to the Hamiltonian from the tunneling of Cooper pairs is given by,

$$\hat{H}_J = -\sum_j E_{J_{j,j-1}} \cos(\hat{\varphi}_j - \hat{\varphi}_{j-1}) \tag{2.1.4}$$

and the summation index j runs over the number of junctions within the array. In the above expression we assumed that all the junctions are identical, and hence they are characterized by a single Josephson energy.

One also has to consider the electrostatic effects due to Coulomb interactions. In electronic devices, usually one considers the electrostatics in terms of the capacitance matrix C_{ij}^{-1},

$$\hat{H}_C = \frac{1}{2} \sum_{ij} (\hat{Q}_i - q_{g_i}) C_{ij}^{-1} (\hat{Q}_j - q_{q_j}) \tag{2.1.5}$$

where the summation indices run over the number of superconducting islands. The operator $\hat{Q}_i$ is called the charge operator and is directly related to the particle (Cooper pair) operator $\hat{N}_i$ via $\hat{Q}_i = Q\hat{N}_i = -2e\hat{N}_i$, and $q_{g_i} = Qn_{g_i}$ is the induced charge which allows us to access specific states of the system, and it is controlled by voltage gates [2]. The induced charge number is related to the gate voltage as follows,

$$n_{g_i} = \frac{1}{Q}\sum_k C_{g_{ik}} V_{g_k} \tag{2.1.6}$$

where $C_{g_{ij}}$ are the capacitances associated with the islands and the gates and V_{g_k} are the gate voltages.

We note that the capacitance matrix C_{ij}^{-1} describes the interactions between islands, and depends on the geometry of the device. Roughly, the island-island capacitance decreases with increasing distance. There is another set of capacitances that develop between the islands and the gates, $C_{g_{ij}}$. These are the ones involved in the expression for the induced charge. In general, the induced charge in a given island is affected by all voltage gates. However, as a first approximation we consider the capacitance between an island j and a gate $k \neq j$ to be small, and thus we have,

$$n_{g_i} \approx \frac{1}{Q} C_{g_{ii}} V_{g_i} \tag{2.1.7}$$

We now re-write 2.1.5 in terms of the particle number operator.

$$\hat{H}_C = \sum_{ij} E_{C_{ij}} (\hat{N}_i - n_{g_i})(\hat{N}_j - n_{q_j}) \tag{2.1.8}$$

where $E_{C_{ij}} = Q^2 C_{ij}^{-1}/2$ is the charging energy involving two interacting Cooper pairs. Finally, the Hamiltonian of the Quantum phase model (QPM) involves two terms, the Josephson Hamiltonian 2.1.4 and the charging Hamiltonian 2.1.8,

$$\hat{H}_{QPM} = \hat{H}_J + \hat{H}_C \tag{2.1.9}$$

2.2 The road map towards the Rice-Mele model

The QPM Hamiltonian given by Eq. 2.1.9, describes an array of Josephson junctions in a quite general setup, assuming that only Cooper pairs can be involved in the dynamics. Our goal for the rest of the chapter is to identify the energy regimes and apply simplifications and/or approximations in order to deduce the problem towards the target model, the Rice-Mele (RM) model. The RM model is a one-dimensional lattice with a two-site unit cell, in which fermions are allowed to tunnel. The Hamiltonian is,

$$\begin{aligned}\hat{H}_{RM}(t) = &-E_{J_1}(t)\sum_j \left(\hat{c}^\dagger_{2j-1}\hat{c}_{2j} + h.c.\right) - E_{J_2}(t)\sum_j f_j\left(\hat{c}^\dagger_{2j}\hat{c}_{2j+1} + h.c.\right) \\ &+ \sum_j \left(\mu_A(t)\hat{c}^\dagger_{2j-1}\hat{c}_{2j-1} + \mu_B(t)\hat{c}^\dagger_{2j}\hat{c}_{2j}\right)\end{aligned} \tag{2.2.1}$$

[2] A superconducting island contains a large (macroscopic) number of Cooper pairs, however if we want to deal with states of the system with a few Cooper pairs, we tune the system to this regime by applying appropriate gate voltages.

where the time-dependent hopping parameters $E_{J_{1/2}}(t)$ and on-site potential $\mu_{A/B}(t)$ have the following form,

$$E_{J_{1/2}}(t) = E_{J_0} \pm \delta E \cos \omega t, \quad \mu_{A/B}(t) = \pm\mu(t) = \pm\Delta \sin \omega t \tag{2.2.2}$$

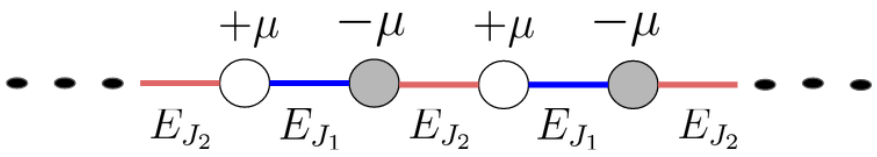

Figure 2.2: The Rice-Mele lattice model of staggering potential μ and hopping parameters $E_{J_{1/2}}$.

We will delve into the properties of this model in Chapter 4. We expect the hopping term to be deduced from the Josephson Hamiltonian and similarly the on-site staggered potential terms from the charging Hamiltonian. Let us start with the Josephson Hamiltonian of Eq. 2.1.4, which we re-write as follows,

$$\hat{H}_J = -\sum_i E_{J_{i,i-1}} \left(e^{-i\hat{\varphi}_i} e^{i\hat{\varphi}_{i-1}} + h.c. \right) \tag{2.2.3}$$

The phase operators in the exponential form correspond to the creation and annihilation operators of the Cooper pairs, i.e. $\hat{\Delta}_i^\dagger \sim e^{-i\hat{\varphi}_i}$ and $\hat{\Delta}_{i-1} \sim e^{i\hat{\varphi}_{i+1}}$, and they are bosonic. Thus the Josephson Hamiltonian corresponds to a hopping term, expressing the tunneling of Cooper pairs between adjacent islands, and reads (apart from $|\Delta|^2$),

$$\hat{H}_J = -\sum_i E_{J_{i,i-1}} \left(\hat{\Delta}_i^\dagger \hat{\Delta}_{i-1} + h.c. \right) \tag{2.2.4}$$

In its current form, the Josephson Hamiltonian does not resemble the hopping term in the Rice-Mele model because the operators live in a much larger Hilbert space of a macroscopic number of Cooper pairs. However, the approximation scheme we develop in the next section will enable the reduction of this Hilbert space to a much smaller one. Before we establish this scheme, we assume that the island-island interactions $E_{C_{i\neq j}}$ are very small compared to the charging energy E_{C_0} [3]. We discuss the effect of interactions in Chapter 6. Therefore, Eq. 2.1.8 reduces to,

$$\hat{H}_C \approx \sum_i E_{C_0} \left(\hat{N}_i - n_{g,i} \right)^2 \tag{2.2.5}$$

where E_{C_0} is the charging energy of the island, and expresses the amount of energy needed to add a Cooper pair to the island. We silently assumed that all the islands are identical, that is of the same size and geometry, i.e. $E_{C,ii} = E_{C_0}$.

Up to this point, the two-part Hamiltonian has taken the form given by Eq. 2.2.4 and Eq. 2.2.5. It is clear now that the dynamics of it is dictated by two energy scales, the Josephson energy E_J and the charging energy E_{C_0}. As we have discussed briefly in the introduction, the case $E_{C_0} \gg E_J$ corresponds to the quantum limit. Large charging energy corresponds to localized states. Localization is translated into having a well-defined particle number, and

[3] It is a valid assumption if we consider that the island-island capacitance decreases with the distance, and this has the same effect on the associated energies.

thus by virtue of the uncertainty relation of $\hat{\varphi}, \hat{N}$ [4], the phase is also characterized by strong quantum phase fluctuations. We thus summarize the energy hierarchy at the problem at hand,

$$T \ll E_J \ll E_{C_0} \ll \Delta_{BCS} \tag{2.2.6}$$

In the next section, we exploit the hardcore bosonic limit, starting from the charging Hamiltonian, and treating the Josephson Hamiltonian as a perturbation.

2.3 The Hardcore boson approximation

In this section, we study the approximation scheme that takes us from a macroscopic description of the island to a two-level system. At the end of this section, we will end up with a quadratic Hamiltonian which resembles that of Eq. 2.2.1. The basis of this approximation lies in the energy hierarchy, and in particular $E_{C_0} \gg E_J$. We will initially focus solely on $\hat{H} \approx H_C$. Later on, we include the Josephson Hamiltonian and study its impact to the approximation scheme.

2.3.1 The charging Hamiltonian

We start by looking the form of Eq. 2.2.5, and we write it as follows:

$$\hat{H}_C = E_{C_0} \sum_j \hat{H}_j, \quad \hat{H}_j = \left(\hat{N}_j - n_{g_j}\right)^2 \tag{2.3.1}$$

where the Hamiltonian $\hat{H}_j$ is the same for any island j. We focus on the spectrum of the Hamiltonian $\hat{H}_j$ of an individual island. Because the latter commutes with the particle number operator $\hat{N}_j$, they share common eigenstates. Therefore, the spectrum is trivially obtained as a function of the induced charge, parametrized by the particle number.

$$E(n_g; N) = E_{C_0}\left(N - n_g\right)^2 \tag{2.3.2}$$

The spectrum is shown in Figure 4.5a for a few parabolas, each one corresponding to a different particle number, as a function of the induced charge. The parabolas intersect at several values of n_g, where we have degeneracy in energy. At these intersections, transitions are allowed between states of different particle number for some tunneling energy E_J. In Figure 4.5a, transitions between states of up to a difference of two particles are displayed. At $n_g \approx N + 1/2$, we identify the degeneracy point of energy $E_{C_0}/4$, which involves two particles states that differ by a particle, and correspond to the ground state of the system at zero temperature. The first excited state corresponds to the degeneracy point involving the states $|N-1\rangle$ and $|N+2\rangle$. The energy difference between the first excited state and the ground state is $E(N-1 \leftrightarrow N+2) - E(N \leftrightarrow N+1) = 9E_{C_0}/4 - E_{C_0}/4 = 2E_{C_0}$. If the charging energy is large compared to some hopping parameter that mixes particle states, then we can only regard single particle transitions at energies $E \sim E_{C_0}/4$.

We fine-tune our system at the near-degeneracy point of $n_g \approx N + 1/2$ (or any other equivalent point), such that we reduce the Fock space of the individual island to two particle states $\{|N\rangle, |N+1\rangle\}$ (see Figure 4.5b). At the vicinity of this point, the spectrum behaves linearly as a function of the induced charge. If we assume a background of some Cooper pair

[4] The uncertainties σ_φ, σ_N of the phase and number operators follow $\sigma_\varphi \sigma_N \sim 1$, arising from the commutation relation of the involved operators.

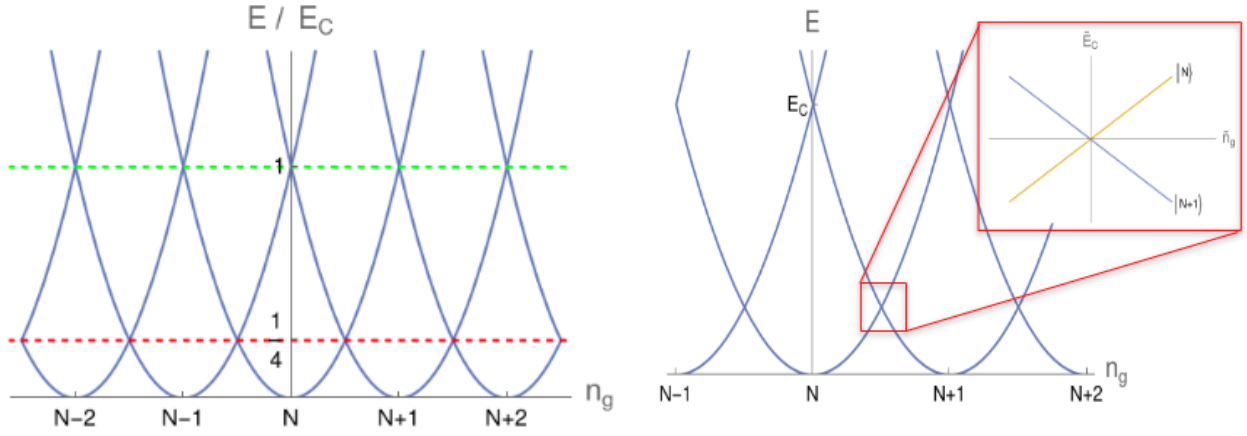

(a) (b)

Figure 2.3: The hardcore boson approximation scheme established in the limit $E_{C_0} \gg E_J$. (a) The spectrum of the charging Hamiltonian Eq. 2.3.2 consists of parabolas, each corresponding to a different particle number N. These parabolas intersect at multiple values of the induced charge n_g. The dashed red line indicates the degeneracy points at which the involved particle states differ by one particle. Similarly, the dashed green line indicate those states that differ by two particles. (b) A closeup view of the spectrum, in which we focus at the near-degeneracy point at $n_g \approx N + 1/2$. At the vicinity of this point, the spectrum is linear in terms of the induced charge, as shown in the inset plot.

number N_0, this choice of n_g allows us to view the system as an effective two-level system and we identify $|N\rangle \to |0\rangle\,, |N+1\rangle \to |1\rangle$. The resulting particle number operator is given in this reduced basis as

$$N_j = \begin{pmatrix} 0 & 0 \\ 0 & 1 \end{pmatrix} \tag{2.3.3}$$

with the property $N_j^2 = N_j$. At the same time, we define new creation and annihilation operators in this reduced basis:

$$a_j^\dagger = \begin{pmatrix} 0 & 0 \\ 1 & 0 \end{pmatrix}, \quad a_j = \begin{pmatrix} 0 & 1 \\ 0 & 0 \end{pmatrix} \tag{2.3.4}$$

which partly resemble bosonic operators,

$$\left[\hat{a}_i^\dagger, \hat{a}_j\right] = \left[\hat{a}_i^\dagger, \hat{a}_j^\dagger\right] = [\hat{a}_i, \hat{a}_j] = 0, \quad i \neq j \tag{2.3.5}$$

and partly resemble fermionic operators,

$$\{\hat{a}_i^\dagger, \hat{a}_i\} = \mathbb{1}, \quad \{\hat{a}_i^\dagger, \hat{a}_i^\dagger\} = \{\hat{a}_i, \hat{a}_i\} = 0 \tag{2.3.6}$$

We commonly refer to these particles which are described by this set of operators, as hardcore bosons, and the approximation scheme we presented becomes the hardcore boson approximation. Under this assumption, the individual charging Hamiltonian admits the following simplification, using the fact that $\hat{N}^2 = \hat{N}$.

$$\hat{H}_j = (\hat{N}_j - n_{g_j})^2 \approx (1 - 2\tilde{n}_{g_j})\hat{N}_j \tag{2.3.7}$$

where $\tilde{n}_{g_j} = n_g - N \approx \frac{1}{2}$. The overall charging Hamiltonian becomes a on-site potential term.

$$\hat{H}_C = \sum_j \mu_j \hat{N}_j, \quad \mu_j = E_{C_0}(1 - 2\tilde{n}_{g_j}) \tag{2.3.8}$$

2.3.2 The role of the Josephson Hamiltonian

At this point, let us briefly demonstrate the implications of adding a hopping term on the linear spectrum at the near-degeneracy point. Such term allows for the transitions to different particle states, and in our work it resembles the tunneling of Cooper pairs between adjacent islands via the Josephson effect. A hopping term mixes the particle states, and we also expect a gap opening at the crossing of the energies.

To demonstrate this, we consider the effect on a single island. The coupling term is,

$$H_J = -E_J(|N\rangle \langle N+1| + h.c.) \tag{2.3.9}$$

such that the total Hamiltonian contains this term and the chemical potential terms obtained from the hardcore boson approximation, in the newly-defined basis $\{|0\rangle, |1\rangle\}$,

$$H = \epsilon_1 |0\rangle \langle 0| + \epsilon_2 |1\rangle \langle 1| - E_J(|0\rangle \langle 1| + h.c.) \tag{2.3.10}$$

where $\epsilon_{1/2}$ are the energies associated with each particle state.

$$\epsilon_{1/2} = \frac{E_{C_0}}{4} \pm E_{C_0}\left(\tilde{n}_g - \frac{1}{2}\right) \tag{2.3.11}$$

The Hamiltonian in the reduced basis of $\{|0\rangle, |1\rangle\}$ adopts the following matrix form,

$$H \to \begin{pmatrix} \epsilon_1 & -E_J \\ -E_J & \epsilon_2 \end{pmatrix} \tag{2.3.12}$$

The hopping term mixes the particle states and following diagonalization, the resulting eigenstates are superpositions of $\{|0\rangle, |1\rangle\}$. The corresponding energies are obtained.

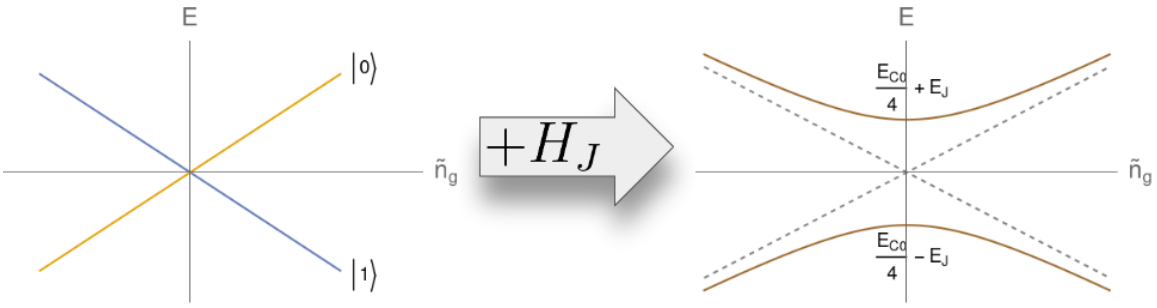

Figure 2.4: A gap opening due to the coupling term H_J at the near-degeneracy point $n_g \approx 1/2$.

$$E_\pm = \frac{\epsilon_1 + \epsilon_2 \pm \sqrt{(\epsilon_2 - \epsilon_1)^2 + 4E_J^2}}{2} = \frac{E_{C_0}}{4} \pm \sqrt{E_{C_0}^2\left(\tilde{n}_g - \frac{1}{2}\right)^2 + E_J^2} \tag{2.3.13}$$

and the gap is given when $n_g = 1/2$,

$$E_g = 2|E_J|^2 \tag{2.3.14}$$

Figure 2.4 demonstrates a gap opening at $n_g = 1/2$, when we consider a coupling term like Eq. 2.3.9.

To make this rigorous, one should consider two neighbouring islands both tuned at the near-degeneracy, with a general state $|n_1, n_2\rangle$ and apply a similar treatment.

2.4 Embracing the Rice-Mele model

The JJA Hamiltonian within the hardcore boson approximation, has been cast into a quadratic Hamiltonian in terms of the newly defined hardcore bosonic operators $\hat{a}_i^\dagger, \hat{a}_i$,

$$\hat{H} = \sum_j \mu_j \hat{N}_j - \sum_j E_{J_{j,j+1}} \left(\hat{a}_j^\dagger \hat{a}_{j+1} + h.c.\right) \tag{2.4.1}$$

where $\mu_j = E_{C_0}(1 - 2n_{g_j})$ and $\hat{N}_j = \hat{a}_j^\dagger \hat{a}_j$. Eq. 2.4.1 resembles the form of the Rice-Mele Hamiltonian, however we still need to show how the parameters $\mu_j, E_{J_{j,j+1}}$ are modulated in time through voltage gates.

Let us begin with the on-site potential μ_j. Recall that the induced charge of a given island j is expressed in terms of the gate voltage associated with that island,

$$n_{g_j} \approx \frac{1}{Q} C_{g_{jj}} V_{g_j} \tag{2.4.2}$$

Assuming that the geometry of the island-gate capacitor is identical to all islands, then we define a unique island-gate capacitance $C_{g_{jj}} = C_{g_0}$.

Therefore, by tuning the gate voltage, we effectively tune the on-site potential term of the Rice-Mele model. To create a bipartite lattice with sublattice indices $\{A, B\}$, we apply an AC voltage over a DC voltage,

$$V_{g_{A/B}}(t) = V_{g_0} \mp \delta V \sin \omega t \tag{2.4.3}$$

Then Eq. 2.4.2 becomes,

$$n_{g_{A/B}}(t) = \frac{C_{g_0} V_{g_0}}{Q} \mp \frac{C_{g_0} \delta V}{Q} \sin \omega t \tag{2.4.4}$$

At this point recall that the foundation of the hardcore boson approximation is the fine-tuning of the induced charge at $n_g \approx 1/2$. Then, we identify $V_{g_0} = \frac{Q}{2C_{g_0}}$, and since $E_{g_0} = \frac{Q^2}{2C_{g_0}}$, we obtain,

$$n_{g_{A/B}}(t) = \frac{1}{2} \mp \frac{Q\delta V}{2E_{g_0}} \sin \omega t \tag{2.4.5}$$

We are required to remain in the vicinity of $n_g = 1/2$ for our two-level system to hold, therefore we should only allow for a small modulation of the induced charge. This is taken care of when $\frac{Q\delta V}{E_{g_0}} \ll 1$. Since the chemical potential is provided by $\mu_j = E_{C_0}(1 - 2n_{g_j})$, then in combination with Eq. 2.4.5, we obtain,

$$\mu_{A/B}(t) = \pm \Delta \sin \omega t, \quad \Delta \equiv Q\delta V \frac{E_{C_0}}{E_{g_0}} \tag{2.4.6}$$

Given the assumption of small modulations of the induced charge, the parameter Δ should be much smaller than the charging energy E_{C_0}, i.e. $\Delta \ll E_{C_0}$. Now, let us discuss the tunneling term. In the experimental setup we propose, the driving of the Josephson energies is attributed to voltage gates placed on the junctions [34]. These gates essentially control the transmission

coefficient of the SN interface by depleting or attracting electrons. The explicit analysis of the modulation of the Josephson energies through gate voltages is beyond the scope of this thesis. The gate voltages can be tuned appropriately as to induce two types of hopping; the intra-cell E_{J_1} (hopping between sites of the same unit cell) and inter-cell E_{J_2} (hopping between sites of adjacent unit cells) hoppings,

$$E_{J_{1/2}}(t) = E_{J_0} \pm \delta E \cos \omega t \tag{2.4.7}$$

After combining everything, the Hamiltonian resembles that of the Rice-Mele model,

$$\begin{aligned} \hat{H}(t) = &\sum_j \mu_A(t) \hat{a}^\dagger_{2j-1} \hat{a}_{2j-1} + \sum_j \mu_B(t) \hat{a}^\dagger_{2j} \hat{a}_{2j} \\ &- \sum_j E_{J_1}(t) \big(\hat{a}^\dagger_{2j-1} \hat{a}_{2j} + h.c. \big) - \sum_j E_{J_2}(t) \big(\hat{a}^\dagger_{2j} \hat{a}_{2j+1} + h.c. \big) \end{aligned} \tag{2.4.8}$$

and the summation runs over the number of unit cells, and the time-dependent parameters are given by Eq. 2.4.6 and Eq. 2.4.7. Still, there is one more thing we need to account for, and that is the operators themselves. Because of the mixed algebra of the hardcore bosonic operators, we are not able to find a proper unitary transformation to diagonalize it (in a single-particle basis). In physical terms, the Hamiltonian of Eq. 2.4.8 actually corresponds to infinitely interacting bosons. This can be understood from the fact that a single site cannot accommodate more than one boson, and this is attributed to strongly interacting bosons. In fermionic systems, only one fermion can be accommodated on a single orbital, because of their particle nature, of them obeying the Pauli exclusion principle. But in hardcore bosons, we somehow enforce this behavior. Nevertheless, we will exploit a technique in the section that maps the hardcore bosonic system to a free fermionic one, and thus we can work with it in a straighforward manner.

2.5 The mapping to free fermions

This section exploits the Jordan-Wigner (JW) transformation [35] which allows us to map a spin Hamiltonian to a fermionic one. Thus, we show how an alternative description of the system in terms of spins can be established, and then apply the JW transformation to map to a free fermionic system.

2.5.1 A spin description of JJA Hamiltonian

We consider a mapping from hardcore bosons to a spin-1/2 representation. The hardcore bosonic commutation/anticommutation algebra is similar to the one obeyed by the ladder operators in the spin picture. In the hardcore boson approximation, we consider two energy levels at the near-degeneracy point. If we make the following identification of the basis kets of the two representations,

$$|0\rangle \leftrightarrow |\uparrow\rangle\,, \quad |1\rangle \leftrightarrow |\downarrow\rangle \tag{2.5.1}$$

then the ladder spin operators and annihilation/creation hardcore bosonic operators are associated with each other as follows,

$$a^\dagger_j \leftrightarrow \sigma^-_j\,, \quad a_j \leftrightarrow \sigma^+_j \tag{2.5.2}$$

The resulting Hamiltonian in the spin representation is trivially obtained:

$$H_{spin}(t) = \sum_j \mu_A(t)\sigma^-_{2j-1}\sigma^+_{2j-1} + \sum_j \mu_B(t)\sigma^-_{2j}\sigma^+_{2j} - E_{J_1}(t)\sum_j \left(\sigma^-_{2j-1}\sigma^+_{2j} + h.c.\right) - E_{J_2}(t)\sum_j \left(\sigma^-_{2j}\sigma^+_{2j+1} + h.c.\right) \tag{2.5.3}$$

We are able now to demonstrate the mapping to free fermions using the Jordan-Wigner transformation.

2.5.2 The Jordan-Wigner transformation

The Jordan-Wigner transformation offers an alternative description of a system in terms of fermionic operators [35], [36]. The fundamental concept underlying the Jordan-Wigner (JW) transformation is to find a transformation that maps a given set of operators, obeying some commutation/anticommutation relations, to a set of fermionic operators, that obey the usual anticommutation relations,

$$\{\hat{c}_i^\dagger, \hat{c}_j\} = \mathbb{1}\delta_{ij}, \quad \{\hat{c}_i^\dagger, \hat{c}_j^\dagger\} = \{\hat{c}_i, \hat{c}_j\} = 0, \ \forall i, j \tag{2.5.4}$$

We seek a unitary transformation $\mathcal{L}_j$,

$$\mathcal{L}_j^\dagger : \hat{\sigma}_j^- \mapsto \hat{c}_j^\dagger, \quad \mathcal{L}_j : \sigma_j^+ \mapsto \hat{c}_j \tag{2.5.5}$$

such that the spin operator transform as follows,

$$\sigma_j^- = \mathcal{L}_j^\dagger \hat{c}_j^\dagger, \quad \sigma_j^+ = \mathcal{L}_j \hat{c}_j \tag{2.5.6}$$

The transformation $\mathcal{L}_j$ is expressed in terms of the fermionic particle number,

$$\mathcal{L}_j^\dagger = e^{-i\pi \sum_{k<j} \hat{c}_k^\dagger \hat{c}_k}, \quad \mathcal{L}_j = e^{i\pi \sum_{k<j} \hat{c}_k^\dagger \hat{c}_k} \tag{2.5.7}$$

and it is called the string operator. The sum on the exponent contains all fermion occupancies at sites before site j, hence the 'string' name. Evidently, it is a non-local transformation. This transformation is unitary, i.e. $\mathcal{L}_j^\dagger \mathcal{L}_j = \mathbb{1}$, and because of that, it preserves the spectrum. Given this explicit map, we are in a position to entirely write Eq. 2.5.3 in terms of fermions.

The on-site staggering potential terms transform as follows:

$$\sigma^-_{2j}\sigma^+_{2j} \mapsto \hat{c}^\dagger_{2j}\hat{c}_{2j}, \quad \sigma^-_{2j-1}\sigma^+_{2j-1} \mapsto \hat{c}^\dagger_{2j-1}\hat{c}_{2j-1}, \tag{2.5.8}$$

where we have exploited the unitarity of the transformation. The Josephson tunneling term for hopping between sites of the same unit cell, transforms as follows:

$$\sigma^-_{2j-1}\sigma^+_{2j} \mapsto \mathcal{L}^\dagger_{2j-1}\hat{c}^\dagger_{2j-1}\mathcal{L}_{2j}\hat{c}_{2j} = \hat{c}^\dagger_{2j-1}\mathcal{L}^\dagger_{2j-1}\mathcal{L}_{2j}\hat{c}_{2j} = \hat{c}^\dagger_{2j-1}e^{i\pi\hat{c}^\dagger_{2j-1}\hat{c}_{2j-1}}\hat{c}_{2j} \tag{2.5.9}$$

where we have used the fermionic anticommutation relations of Eq. 2.5.4. The transformation resulted into an additional phase which can be removed. Consider the sites $2j-1$ and $2j$ and the particle product state $|\psi\rangle = |n_1\rangle_{2j-1} \otimes |n_2\rangle_{2j}$, where $n_1, n_2 \in \{0, 1\}$, as imposed by the Pauli exclusion principle. Let us define the operator:

$$\hat{\mathcal{K}} \equiv \hat{c}^{\dagger}_{2j-1} e^{i\pi \hat{c}^{\dagger}_{2j-1}\hat{c}_{2j-1}} \otimes \hat{c}_{2j} \tag{2.5.10}$$

which is the fermionized version of $\sigma^{-}_{2j-1}\sigma^{+}_{2j}$. Now, let the new operator act on the particle state $|\psi\rangle$,

$$\hat{\mathcal{K}}\,|\psi\rangle = \big(\hat{c}^{\dagger}_{2j-1} e^{i\pi \hat{c}^{\dagger}_{2j-1}\hat{c}_{2j-1}} \otimes \hat{c}_{2j}\big)\big(\,|n_1\rangle \otimes |n_2\rangle\,\big) = \big(\hat{c}^{\dagger}_{2j-1} e^{i\pi \hat{c}^{\dagger}_{2j-1}\hat{c}_{2j-1}}\,|n_1\rangle_{2j-1}\,\big) \otimes \big(\hat{c}_{2j}\,|n_2\rangle_{2j}\,\big)$$

There are four possible combinations for $\{n_1, n_2\} = \{00, 01, 10, 11\}$. Only one of these give a non-zero $\hat{\mathcal{K}}\,|\psi\rangle$, the combination $(c_1 = 0, c_2 = 1)$. For this case, we get:

$$\hat{\mathcal{K}}\,|\psi\rangle = \big(\hat{c}^{\dagger}_{2j-1} e^{i\pi \hat{c}^{\dagger}_{2j-1}\hat{c}_{2j-1}}\,|0\rangle_{2j-1}\,\big) \otimes \big(\hat{c}_{2j}\,|1\rangle_{2j}\,\big) = e^{i\pi 0}\hat{c}^{\dagger}_{2j-1}\,|0\rangle_{2j-1} \otimes \hat{c}_{2j}\,|1\rangle_{2j} = \hat{c}^{\dagger}_{2j-1}\hat{c}_{2j}\,|\psi\rangle$$

where we used $\hat{n}_{2j-1}\,|n\rangle_{2j-1} = \hat{c}^{\dagger}_{2j-1}\hat{c}_{2j-1}\,|n\rangle_{2j-1} = n\;\,|n\rangle_{2j-1}$. The obtained result involves the same product of fermionic operators as initially, but without the phase. The Josephson term that involves tunneling between sites of different unit cells, transforms in exactly the same way, where the argument of omitting the phase still holds. The total fermionic Hamiltonian reads:

$$\begin{aligned}\hat{H}_f(t) = &\sum_j \mu_A(t)\hat{c}^{\dagger}_{2j-1}\hat{c}_{2j-1} + \sum_j \mu_B(t)\hat{c}^{\dagger}_{2j}\hat{c}_{2j} \\ &- \sum_j E_{J_1}(t)\big(\hat{c}^{\dagger}_{2j-1}\hat{c}_{2j} + h.c.\big) - {\sum_j}' E_{J_2}(t)\big(\hat{c}^{\dagger}_{2j}\hat{c}_{2j+1} + h.c.\big)\end{aligned} \tag{2.5.11}$$

where ${\sum_j}'$ runs over the number of unit cells minus one. The fermionized Hamiltonian of Eq. 2.5.11 applies specifically to open boundary conditions. The case of periodic boundary conditions is slightly subtle because of the boundary term, which has to be considered separately. The boundary term, between the $2N$ site and the first one is:

$$H_{boundary} = -E_{J_2}\big(\sigma^{-}_{2N}\sigma^{+}_{1} + h.c.\big) \tag{2.5.12}$$

First, we make the identification, $\sigma^{-}_{2N}\sigma^{+}_{1} = \sigma^{-}_{2N}\sigma^{+}_{2N+1}$. This form helps us to treat this term virtually as any other term that involves tunneling between unit cells. We apply the Jordan-Wigner transformation on the spin operator of the virtual site,

$$\sigma^{+}_{2N+1} = \mathcal{L}_{2N+1}\hat{c}_{2N+1} = e^{i\pi \sum_{k<2N-1}\hat{c}^{\dagger}_{k}\hat{c}_{k}}\hat{c}_{2N+1} = e^{i\pi\hat{n}}\hat{c}_{2N+1} \tag{2.5.13}$$

where the number operator $\hat{n} = \sum_{k<2N-1}\hat{c}^{\dagger}_{k}\hat{c}_{k}$ gives the total number of fermions in the system. At the same time, we have $\sigma^{+}_{1} = \hat{c}_1$ and since $\sigma^{+}_{1} = \sigma^{+}_{2N+1}$, then:

$$\hat{c}_1 = e^{i\pi\hat{n}}\hat{c}_{2N+1} \tag{2.5.14}$$

Therefore, the fermionized version of the boundary term is:

$$\sigma^{-}_{2N}\sigma^{+}_{1} = \hat{c}^{\dagger}_{2N}e^{-i\pi\hat{n}}\hat{c}_1 \tag{2.5.15}$$

Consider a particle state of N_e electrons, $|N_e\rangle$ which describes the system under consideration. Let us apply the fermionized operator of 2.5.15 to the aforementioned particle state.

$$\hat{c}^{\dagger}_{2N}e^{-i\pi\hat{n}}\hat{c}_1\,|N_e\rangle = \hat{c}^{\dagger}_{2N}e^{-i\pi\hat{n}}\,|N_e - 1\rangle \tag{2.5.16}$$

assuming that there is a fermion on site 1, otherwise the whole expression is zero. Now, we proceed as follows:

$$\hat{c}_{2N}^{\dagger} e^{-i\pi\hat{n}} \left|N_e - 1\right\rangle = \hat{c}_{2N}^{\dagger} e^{-i\pi(N_e-1)} \left|N_e - 1\right\rangle = -\hat{c}_{2N}^{\dagger} e^{-i\pi N_e} \left|N_e - 1\right\rangle = -e^{-i\pi N_e} \hat{c}_{2N}^{\dagger} \hat{c}_1 \left|N_e\right\rangle \tag{2.5.17}$$

where we have used $\left|N_e - 1\right\rangle = \hat{c}_1 \left|N_e\right\rangle$. Thus, we find:

$$\hat{c}_{2N}^{\dagger} e^{-i\pi\hat{n}} \hat{c}_1 \left|N_e\right\rangle = -e^{-i\pi N_e} \hat{c}_{2N}^{\dagger} \hat{c}_1 \left|N_e\right\rangle = (-1)^{N_e-1} \hat{c}_{2N}^{\dagger} \hat{c}_1 \left|N_e\right\rangle \tag{2.5.18}$$

and the overall sign depends on the parity of the particle number. If we have an odd particle number, then we obtain an additional minus sign in front. On the other hand, having an even number of particles does not yield an extra minues sign. This additional term does not introduce any peculiarities to the system, from a physical point of view. However, it does impact the mathematical side of things. If the parity of the particle number is odd, then this corresponds to the minus sign and the system is treated as having ordinary periodic boundary conditions. However, if the parity of the particle number is even, then the boundary term switches to a plus sign. This can be translated into a complex phase $+1 = -e^{i\pi}$. We can think about it as the effect of a magnetic flux penetrating the ring. It results to a shift of the Brillouin zone in momentum space, which however does not impact the observable quantities for large system sizes.

The fermionized Hamiltonian for periodic boundary conditions reads,

$$\begin{aligned} \hat{H}_f(t) = &\sum_j \mu_A(t) \hat{c}_{2j-1}^{\dagger} \hat{c}_{2j-1} + \sum_j \mu_B(t) \hat{c}_{2j}^{\dagger} \hat{c}_{2j} - E_{J_2}(t)(-1)^{N_e-1} \left(\hat{c}_{2N}^{\dagger} \hat{c}_1 + h.c.\right) \\ &- \sum_j E_{J_1}(t) \left(\hat{c}_{2j-1}^{\dagger} \hat{c}_{2j} + h.c.\right) - {\sum_j}' E_{J_2}(t) \left(\hat{c}_{2j}^{\dagger} \hat{c}_{2j+1} + h.c.\right) \end{aligned} \tag{2.5.19}$$

where ${\sum_j}'$ runs over the number of unit cells minus one. Because of the quadratic form of the Hamiltonian, we can write it in a more compact form in the real space basis:

$$H_f = C^{\dagger} \mathcal{H} C, \quad C = \begin{pmatrix} \hat{c}_1 & \hat{c}_2 & \hat{c}_3 & \cdots & \hat{c}_{2N} \end{pmatrix}^T \tag{2.5.20}$$

and

$$\mathcal{H} = \begin{pmatrix} \mu_A & -E_{J_1} & 0 & 0 & 0 & \cdots & -E_{J_2}(-1)^{N_e-1} \\ -E_{J_1} & \mu_B & -E_{J_2} & 0 & 0 & \cdots & 0 \\ 0 & -E_{J_2} & \mu_A & -E_{J_1} & 0 & \cdots & 0 \\ 0 & 0 & -E_{J_1} & \mu_B & 0 & \cdots & 0 \\ 0 & & & \ddots & \ddots & & \vdots \\ \vdots & & & & & \ddots & -E_{J_1} \\ -E_{J_2}(-1)^{N_e-1} & 0 & 0 & \cdots & & -E_{J_1} & \mu_B \end{pmatrix} \tag{2.5.21}$$

where the size of the matrix $\mathcal{H}$ is $2N \times 2N$. In principal, because of translational invariance, we can map to momentum space and work there. However, we will consider the real-space formalism once we introduce disorder in the system in Chapter 5.

Chapter 3

Floquet Theory in Quantum Systems

Before diving deep into the physics of the Rice-Mele model and the extension thereof with the introduction of superconducting leads, let us present some basic notions and concepts of the theory of periodically time-dependent quantum systems, the Floquet theory. The latter will be of great importance in the study of dynamics of the system of interest. For this reason, we ought to devote a whole chapter, on which we emphasize on the implications of a periodically driven system, arising within the context of Floquet theory.

3.1 The mathematical setup

The dynamics of a quantum system are governed by the time-dependent Schrödinger equation:

$$i\frac{\mathrm{d}}{\mathrm{d}t}\left|\psi(t)\right\rangle = H(t)\left|\psi(t)\right\rangle \tag{3.1.1}$$

Alternatively, the ket state of the system can be obtained by applying the unitary time evolution operator to an initial state,

$$\left|\psi(t)\right\rangle = U(t,t_0)\left|\psi(t_0)\right\rangle \tag{3.1.2}$$

thus we just have to determine the time evolution operator, which also obeys the time-dependent Schrödinger equation.

$$\dot{U}(t,t_0) = -iH(t)U(t,t_0) \tag{3.1.3}$$

where we use the dot above the operator to denote differentiation with respect to time, and we have transferred the imaginary unit to the RHS. Eq. 3.1.3 constitutes a system of linear first-order ordinary differential equations, of the general form $\dot{U} = AU$ where both U and A are $n \times n$ matrices, and in our case $A = A(t) = -iH(t)$.

Since we are dealing with periodically driven systems in which $H(t+\tau) = H(t)$ where τ is the period of the drive, t hen $A(t+\tau) = A(t)$ as well. Thus, we want to solve $\dot{U}(t) = A(t)U(t)$ with $A(t+\tau) = A(t)$. This situation was tackled first mathematically by Gaston Floquet [37]. Then, his theory was adopted by physicists to study classical and quantum systems under the influence of a periodic drive [1] [38].

[1] Similar considerations to the Floquet theory were adopted by Bloch a few decades later when developing his theory for systems with particles under the influence of a periodic potential, $V(x+a) = V(x)$ where a characterizes the lattice periodicity. The resulting theorem was therefore named after him.

3.2 Periodically driven systems

In this section, we introduce the theory of periodically driven systems, the Floquet theory. One who is already familiar with the Bloch theorem will find out that the two theories share several similarities, but in a different context. The Bloch theorem applies to systems with space periodicity, i.e. $H(\vec{x}+\vec{R}) = H(\vec{x})$, where $\vec{R}$ is a linear combination of the primitive lattice vectors. The space periodicity implies conservation of the crystal momentum (or quasi-momentum) within a reciprocal lattice vector [39].

In Floquet theory, we are concerned with a similar situation. The Hamiltonian of the system possesses discrete time translation symmetry since $H(t+T) = H(t)$, where $T = m\tau$ is an integer multiple of the driving period τ. Then, as one should expect this leads in some form of energy conservation, perhaps in the same way as in the Bloch theorem. We note that, in general, the Hamiltonian does not commute with itself at different time moments, i.e. $[H(t'), H(t'')] \neq 0$.

Given a time-dependent Hamiltonian $H(t)$, the state of the system obeys the time-dependent Schrödinger equation of Eq. 3.1.1. Equivalently, the time-evolved state is obtained by applying the unitary time evolution operator $U(t, t_0)$, to an initial state.

$$\hat{U}(t,t_0) : \mathcal{H} \to \mathcal{H} \times [0,t], \quad \hat{U}(t,t_0) : |\psi_0\rangle \mapsto |\psi(t)\rangle = \hat{U}(t,t_0)\,|\psi_0\rangle \tag{3.2.1}$$

and $U(t_0, t_0) = \mathbb{1}$. The time evolution operator solves the time-dependent Schrödinger equation,

$$i\frac{\mathrm{d}}{\mathrm{d}t}U(t) = H(t)U(t), \quad U(t) = \mathcal{T}\exp\left\{-i\int_0^t H(t')dt'\right\} \tag{3.2.2}$$

where $\mathcal{T}$ is the time-ordering operator. At time $t = \tau$, we obtain the so-called Floquet operator:

$$U(\tau) \equiv F(\tau) = \mathcal{T}\exp\left\{-i\int_0^\tau H(t')dt'\right\} \tag{3.2.3}$$

We define the effective or Floquet Hamiltonian which provide us with an effective description of the system over a period of the drive.

$$F(\tau) = \exp\{-iH_F\tau\}, \quad H_F = \sum_{k=0}^{\infty} H_F^{(k)} \tag{3.2.4}$$

The Floquet Hamiltonian is written as an infinite sum over integrals and commutators of the original time-periodic Hamiltonian over a period of the drive, in accordance to the Magnus expansion. The first two expansion coefficients are provided.

$$H_F^{(1)} = \frac{1}{\tau}\int_0^\tau H(t_1)dt_1 \tag{3.2.5}$$

$$H_F^{(2)} = \frac{-i}{2\tau}\int_0^\tau dt_1 \int_0^{t_1} dt_2\,[H(t_1), H(t_2)] \tag{3.2.6}$$

The first term $H_F^{(1)}$ of the expansion is the time-averaged Hamiltonian.

Having determined the time evolution operator and obtained the Floquet operator at $t = \tau$, we can diagonalize it by applying an appropriate unitary (basis) transformation U_F.

$$U_F : F(\tau) \mapsto U_F F(\tau) U_F^\dagger = D \tag{3.2.7}$$

where D is a diagonal matrix containing the eigenvalues. The basis transformation U_F contain the corresponding eigenvectors which are called Floquet states $|\phi_\nu(\tau)\rangle$ and they form a complete, orthonormal set with the following resolution of identity $\sum_\nu |\phi_\nu(\tau)\rangle \langle\phi_\nu(\tau)| = \mathbb{1}$. The eigenvalues lie on the unit circle $\lambda_\nu = e^{i\gamma_\nu}$, due to the unitarity of the Floquet operator. Conventioanlly, we choose the parametrization $\gamma_\nu = -i\varepsilon_\nu \tau$ and ε_ν are the quasienergies.

Regarding the quasienergies, one might be tempted to write [38],

$$H_F |\phi_\nu\rangle = \varepsilon_\nu |\phi_\nu\rangle \tag{3.2.8}$$

however, this statement is only a part of the whole story. By taking into account that the Floquet operator is a complex exponential, we should treat it accordingly when we take the logarithm.

$$\log F(\tau) = -i\big(H_F \tau + 2\pi n\big) = -i\big(H_F + \omega n\big)\tau, \quad n \in \mathbb{Z} \tag{3.2.9}$$

and ω is the frequency of the drive. Then, if we express Eq. 3.2.9 with the Floquet Hamiltonian on the LHS, then the eigenvalues will be:

$$\varepsilon_{(\nu,m)} = \varepsilon_\nu + \omega m, \quad m \in \mathbb{Z} \tag{3.2.10}$$

which implies multivaluedness of the quasienergies. For a given ν, the quasienergy $\varepsilon_{\nu,m}$ is multi-valued across the whole energy axis. The original quasienergies ε_ν are uniquely defined within a finite interval, identified as the first Floquet-Brillouin zone (FBZ), of width ω.

$$-\omega/2 \leq \varepsilon_\nu \leq \omega/2 \tag{3.2.11}$$

This redundancy in the Floquet spectrum arises due to the discrete time-translation invariance of the system. The quasienergy periodicity implies that under the effect of a periodic drive, the system's energy is conserved up to the absorption or emission of integer multiples of the driving field quanta energy. Likewise, a similar situation occurs in the Bloch theorem with the crystal momentum, as we briefly discussed in the beginning of the section.

Let us now discuss about the implications of the time periodicity in the time evolution of the system. The time evolution operator at any time t is expressed as a product of itself defined within a driving period and the Floquet operator.

$$U(t + n\tau, t_0) = U(t, t_0)[F(\tau)]^n \tag{3.2.12}$$

where $F(\tau)$ is the Floquet operator we introduced earlier. The knowledge of the unitary operator within a driving period suffices to evolve the system in time $\forall t \geq 0$. This statement may appear somewhat obvious, given the transparent semigroup property. One needs to show that the time evolution operator defined within a driving period obeys the same Schrödinger equation as the full time evolution operator and also the same initial condition [40]. Let us pause and think about this decomposition of the total time evolution operator. We can distinguish two types of periodic motion, the micromotion and the stroboscopic motion. The former expresses the motion of the system during a period of the drive and is affiliated with $U(t, t_0)$. The latter is represented by the Floquet operator $F(\tau)$ and describes the system at times $t = m\tau,\ m \in \mathbb{N}$.

An alternative form of the time evolution operator can be defined by exploiting the form of the Floquet operator. We write the time evolution operator within a single period as a product of a periodic unitary operator $P(t)$ and the exponential $\exp\{-iH_F t\}$.

$$U(t) = P(t)e^{-iH_F t}, \quad P(t+\tau) = P(t) \tag{3.2.13}$$

Now, let us evolve in time the initial ket state by applying the time evolution operator of Eq. 3.2.13. We project the initial state on the Floquet basis, i.e. $|\psi_0\rangle = \sum_\nu |\phi_\nu\rangle \langle\phi_\nu|\psi_0\rangle = \sum_\nu c_n |\phi_\nu\rangle$.

$$|\psi(t)\rangle = U(t)|\psi_0\rangle = P(t)e^{-iH_F t}|\psi_0\rangle = \sum_\nu c_n e^{-i\varepsilon_\nu t}|u_n(t)\rangle \tag{3.2.14}$$

where we have defined $|u_\nu(t)\rangle \equiv P(t)|\phi_\nu\rangle$ and we called these states Floquet modes and they possess the time periodicity of the system, inherited by $P(t)$. We also used the fact that $e^{-iH_F t}|\phi_\nu\rangle = e^{-i\varepsilon_\nu t}|\phi_\nu\rangle$. Eq. 3.2.14 states that any state can be expanded with respect to the Floquet states, and the coefficients c_n that depend on the initial state are time-dependent. Importantly, $|c_n|^2$ corresponds to occupation probabilities to the Floquet states, which are preserved throughout the time evolution.

We can go further and defined the time-dependent Floquet states $|\psi_\nu(t)\rangle \equiv e^{-i\varepsilon_\nu t}|u_\nu(t)\rangle$ which also form a complete, orthonormal set. The time-dependent Floquet states are decomposed into a plane wave and a function with the periodicity of the driving field. A similar decomposition is encountered in the Bloch theorem, in which the periodic function inherits the periodicity of the real lattice. Note that the states $|\psi_\nu\rangle(t)$ are not periodic in time themselves. Instead, a phase factor arises

$$|\psi_\nu(t+\tau)\rangle = e^{-i\varepsilon_\nu \tau}|\psi_\nu(t)\rangle \tag{3.2.15}$$

As a final remark, notice that the phase factors $e^{-i\varepsilon_\nu t}$ appearing throughout this analysis, resemble the usual factors $e^{-iE_n t}$ associated with the time evolution of the eigenstates of a time independent Hamiltonian. Hence, the quantities ε_ν are called quasienergies.

3.3 The mapping to an effective, static description

In the following lines, we describe a different approach of treating a time-periodic system using Fourier expansion. This approach is sometimes referred to as the Shirley-Floquet approach [38]. This approach is the basis of the mapping of a dynamic system to a static one by creating a synthetic dimension.

Given a time-periodic Hamiltonian $H(t+\tau) = H(t)$ with τ being the driving period, then we can Fourier expand as follows:

$$\hat{H}(t) = \sum_m e^{-im\omega t}\hat{H}^{(m)} \tag{3.3.1}$$

where $\omega = 2\pi/T$ is the driving frequency. The summation index m covers the whole set of integers. The coefficients $\hat{H}^{(m)}$ are obtained by the inverse Fourier transformation.

$$\hat{H}^{(m)} = \frac{1}{\tau}\int_0^\tau dt\ \hat{H}(t)e^{im\omega t} \tag{3.3.2}$$

From the Floquet theorem, the time-dependent Floquet states are expressed as a product of a plane wave and a periodic function $|\psi_n(t)\rangle = e^{-i\epsilon_n t}|u_n(t)\rangle$. The Floquet modes $|u_n(t)\rangle$ are periodic functions of time and hence they can be Fourier expanded.

$$|u_n(t)\rangle = \sum_m e^{-im\omega t}\left|u_n^{(m)}\right\rangle \tag{3.3.3}$$

The Floquet states are solutions of the time-dependent Schrödinger equation,

$$i\frac{\partial}{\partial t}|\psi_n(t)\rangle = \hat{H}(t)|\psi_n(t)\rangle \tag{3.3.4}$$

and thus we can use the product form of it to obtain:

$$\left[\varepsilon_n + i\partial_t\right]|u_n(t)\rangle = \hat{H}(t)|u_n(t)\rangle \tag{3.3.5}$$

We use the expansion of the Floquet modes, Eq. 3.3.3, and of the Hamiltonian, Eq. 3.3.1, to expand Eq. 3.3.5.

$$\sum_{l,m} e^{-i(l+m)\omega t}H^{(l)}\left|u_n^{(m)}\right\rangle - \sum_m m\omega e^{-im\omega t}\left|u_n^{(m)}\right\rangle = \varepsilon_n \sum_m e^{-im\omega t}\left|u_n^{(m)}\right\rangle \tag{3.3.6}$$

Let us work with the first term. Allow the change of variables $l+m \to m$ to occur for the sum over m.

$$\sum_l\sum_m e^{-i(l+m)\omega t}H^{(l)}\left|u_n^{(m)}\right\rangle \;\to\; \sum_l\sum_m e^{-im\omega t}H^{(l)}\left|u_n^{(m-l)}\right\rangle \tag{3.3.7}$$

and the sum over m still runs over the infinite integer value set. We can now change the order of the summations without consequences, and allow a change of variables $m-l \to l$ for the summation over l.

$$\sum_m e^{-im\omega t}\sum_l H^{(l)}\left|u_n^{(m-l)}\right\rangle \;\to\; \sum_m e^{-im\omega t}\sum_l H^{(m-l)}\left|u_n^{(l)}\right\rangle \tag{3.3.8}$$

and the sum over l still runs over the infinite integer value set. After this small step, we return back to 3.3.6. This procedure leads to the following result, in which we left out the summation over m and the complex exponentials.

$$\sum_l\left[H^{(m-l)} - l\omega\delta_{m,l}\right]\left|u_n^{(l)}\right\rangle = \varepsilon_n\left|u_n^{(m)}\right\rangle \tag{3.3.9}$$

Now, this is an eigenvalue equation of the form:

$$\mathcal{H}u_n = \varepsilon_n u_n \tag{3.3.10}$$

and the quasienergies ε_n form the spectrum of the extended Hamiltonian $\mathcal{H}$, which is represented by infinite copies of the Floquet-Brillouin zone (extended spectrum) [41]. The extended Hamiltonian $\mathcal{H}$ and the Fourier coefficients u_n are given by,

$$\mathcal{H} = \begin{pmatrix} \ddots & H^{(-1)} & H^{(-2)} & \\ H^{(1)} & H_0 - m\omega & H^{(-1)} & H^{(-2)} \\ H^{(2)} & H^{(1)} & H_0 - (m+1)\omega & H^{(-1)} \\ & H^{(2)} & H^{(1)} & \vdots \end{pmatrix}, \quad u_n = \begin{pmatrix} \vdots \\ \left|u_n^{(m)}\right\rangle \\ \left|u_n^{(m+1)}\right\rangle \\ \vdots \end{pmatrix} \tag{3.3.11}$$

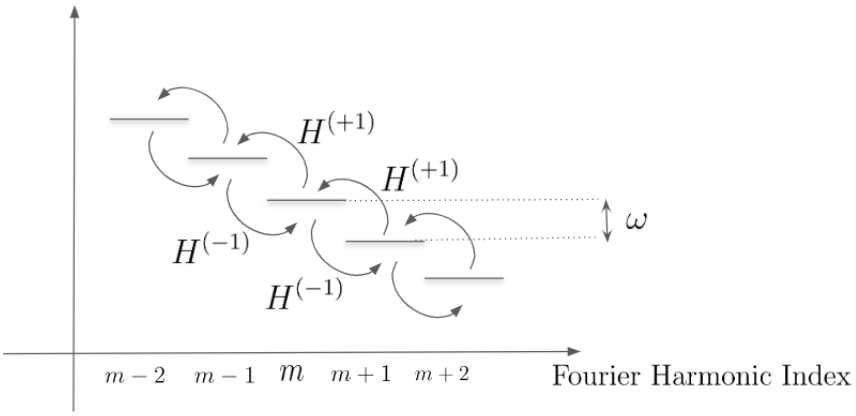

Figure 3.1: A representation of the extended Floquet Hamiltonian (y-axis corresponds to the energy). $H^{(0)}$ (not shown) describes the physics on a single level characterized by the frequency index m and $H^{(\pm 1)}$ couple states of frequency indices, which differ by 1. Couplings of higher order $|\Delta m| > 1$ represented by $H^{(|\Delta m|)}$ are not displayed. Levels of different m are shifted with respect to each other by the driving frequency ω, resembling energy shifts because of a static electric field [42].

From now on, m is the frequency index. The extended Floquet Hamiltonian is block structured, since each Fourier component of the Hamiltonian $H^{(m)}$ is a $d \times d$ matrix, where d is the dimension of the original Hilbert space. $H^{(0)}$ is the time-averaged Hamiltonian, defined on each frequency index and $H^{(\Delta m)}, \Delta m \neq 0$ couple different frequency indices. In the case of a driving of sinusoidal form, we have $H^{(\Delta m)} = 0,\ |\Delta m| > 1$. The driving field appears here as a shift in energy, proportional to the frequency index, and resembles an applied, constant electric field. In Figure 3.1, the energy levels of a few values of the frequency index are shown, along with the associated nearest-neighbour couplings. The levels are shifted relative to each other by the driving frequency ω.

Because of the infinite size of the objects in Eq. 3.3.10, one has to truncate the total space, reducing to an effective, finite system of algebraic equations. In the case of an adiabatic driving in which $\omega \to 0$, the truncation can be chosen arbitrarily since effetively the shift between energy levels because of ω is negligible in this regime.

Notably, this feature highlights the importance of driven systems of topological character, and especially the prospect of understanding higher order topological phases [43], that cannot be accessed with experiments in real space.

3.4 Charge pumping in the Floquet picture

In this section, we discuss adiabatic quantum pumping in the context of Floquet theory. Floquet theory allows us to study a system dynamically, for long times. Importantly, by exploiting Eq. 3.2.12, one can study the system at any arbitrary time since all we need is to determine the Floquet operator and the time evolution operator within a driving period. In contrast, this can become a cumbersome task if we choose to solve the Schrödinger equation directly. In the following subsection, we show how we obtain the transferred charge in the infinite-time limit. This is only possible if we work explicitly in the Floquet representation. Furthermore, we also touch the issue of adiabaticity later on.

3.4.1 The infinite time limit

Given a many-body system with time-dependent Hamiltonian $H(t)$ under the influence of a periodic drive, we are interested in the charge Q transferred over a driving period, which is given as the time integral over the expectation value of the current operator $\mathcal{J}(t)$,

$$Q = \frac{1}{\tau}\int_0^\tau dt\, \langle \mathcal{J}(t)\rangle\,, \quad \langle \mathcal{J}(t)\rangle = \mathrm{tr}\{\rho(t)\mathcal{J}(t)\} \tag{3.4.1}$$

where $\rho(t)$ is the state of the system at time t. Usually we are interested in the behavior of the system at a later time in the distant future, so we consider the infinite-time limit,

$$Q_\infty = \lim_{m\to\infty}\frac{1}{m}\int_0^{m\tau} dt\ \langle \mathcal{J}(t)\rangle \tag{3.4.2}$$

Let us start by addressing the time evolution of the state of the system. The system is initialized in the ground state of the Hamiltonian $H(t)$ at time $t = 0$.

$$\rho_0 = |GS\rangle\langle GS| \tag{3.4.3}$$

The initial density matrix is then mapped to the Floquet basis via the basis transformation U_F established in Section 3.2, $U_F : \rho_0 \mapsto \tilde{\rho}_0 = U_F\rho_0 U_F^\dagger$,

$$\tilde{\rho}_0 = \sum_{\mu,\nu}\mathcal{C}_{\mu\nu}\,|\Phi_\mu\rangle\langle\Phi_\nu| \tag{3.4.4}$$

where the coefficients $\mathcal{C}_{\mu\nu} = \langle\Phi_\mu(\tau)|\rho_0|\Phi_\nu(\tau)\rangle = \langle\Phi_\mu|GS\rangle\langle GS|\Phi_\nu\rangle$ correspond to the overlaps of the ground state to the Floquet states. The states $\{|\Phi\rangle_\nu\}$ are the many-body Floquet states, obtained by diagonalizing the Floquet operator. The transformed density matrix $\tilde{\rho}_0$ is evolved in time by applying the time evolution operator $U(t,t_0) : \tilde{\rho}_0 \mapsto \tilde{\rho}(t) = U(t,t_0)\tilde{\rho}_0 U^\dagger(t,t_0)$.

$$\tilde{\rho}(t) = \sum_{\mu,\nu}\mathcal{C}_{\mu\nu}\,U(t,t_0)\,|\Phi_\mu(\tau)\rangle\langle\Phi_\nu(\tau)|\,U^\dagger(t,t_0) \tag{3.4.5}$$

Since the expectation value of the current operator is the trace of the product of the density matrix and the current, then for $t + m\tau,\ m \in \mathbb{N}$,

$$\langle \mathcal{J}(t+m\tau)\rangle = \sum_{\mu,\nu}\mathcal{C}_{\mu\nu}\,e^{-i(\mathcal{E}_\mu-\mathcal{E}_\nu)m\tau}\,\langle\Phi_\nu(t)|\,\mathcal{J}(t)\,|\Phi_\mu(t)\rangle \tag{3.4.6}$$

where $|\Phi_\nu(t)\rangle = U(t,t_0)\,|\Phi_\nu(\tau)\rangle$ are the time-evolved Floquet states. Note that the matrix element $\langle\Phi_\nu(t)|\,\mathcal{J}(t)\,|\Phi_\mu(t)\rangle$ is time-periodic since both the time-evolved Floquet states and the current operator are periodic in time. Additionally, we have used the fact that

$$U(t+m\tau)\,|\Phi_\mu(\tau)\rangle = U(t)[F(\tau)]^m\,|\Phi_\mu(\tau)\rangle = e^{-i\mathcal{E}_\mu m\tau}U(t)\,|\Phi_\mu\rangle \tag{3.4.7}$$

and $\mathcal{E}_\mu$ is the many-body quasienergy. Now, using Eq. 3.4.6 the pumped charge in the infinite-time limit admits the following form,

$$Q_\infty = \lim_{m\to\infty}\frac{1}{m}\int_0^{m\tau} dt'\sum_{\mu,\nu}\mathcal{C}_{\mu\nu}e^{-i\Omega_{\mu\nu}(m-1)\tau}\,\langle\Phi_\nu(t')|\,\mathcal{J}(t')\,|\Phi_\mu(t')\rangle \tag{3.4.8}$$

where $\Omega_{\mu\nu} = (\mathcal{E}_\mu - \mathcal{E}_\nu)$. The time parameter $t' \geq 0$ is expressed as $t' = t + (m-1)\tau$ where $t \in [0,\tau)$ and $m \in \mathbb{N}$. In the Appendix B, we show how to deal with this expression. After some manipulations, the pumped charge in the infinite-time limit is expressed as the sum of

integrals of the expectation value of the current operator in a Floquet state $|\Phi_\mu\rangle$, weighted by the associated occupation number $\mathcal{N}_\mu$,

$$Q_\infty = \sum_\mu \mathcal{N}_\mu \int_0^\tau dt \, \langle \Phi_\mu(t)| \, \mathcal{J}(t) \, |\Phi_\mu(t)\rangle \tag{3.4.9}$$

This equation allows us to view the system after a very long time, essentially telling us where the system will end up. All we have to do is use the knowledge provided to us within a driving period such as the time evolution operator, the Floquet operator and the occupations of the Floquet states. We can take it a step further by taking advantage of the properties of the time evolution operator and that the current can be written as the derivative of the Hamiltonian with respect to a fictitious flux ϕ, i.e. $\mathcal{J} = \partial_\phi H|_{\phi=0}$ - the latter is discussed in detail in Section 4.3 in Chapter 4. Then, it is shown in the Appendix B that the charge is re-written in terms of the derivative of the quasienergy,

$$Q_\infty = \tau \sum_\mu \mathcal{N}_\mu \partial_\phi \mathcal{E}_\mu|_{\phi=0} \tag{3.4.10}$$

We will return to this expression in Chapter 6 in which ϕ will play a significant role. But at the moment, let us admire the elegant form that the pumped charge takes in the infinite-time limit in terms of the quasienergy and the occupations of the Floquet states. Admittedly, this expression will allow us to interpret the quantized particle transport in the Rice-Mele model in the presence of superconducting leads in Chapter 6.

3.4.2 Adiabatic limit

We complete our discussion on quantum pumping in the Floquet picture by exploring the adiabatic limit. We consider a gapped Hamiltonian $H(t)$ with $H(t+\tau) = H(t)$ where τ is the driving period and ω the driving frequency. The adiabatic regime is characterized by $\omega \to 0$. The Hamiltonian can be diagonalized at each instant of time, obtaining thus the instantaneous eigenstates $\{|\chi_n(t)\rangle\}$ and energies $\{E_n(t)\}$.

$$\hat{H}(t) \, |\chi_n(t)\rangle = E_n(t) \, |\chi_n(t)\rangle \tag{3.4.11}$$

In the Floquet formalism, we have introduced the time dependent Floquet states, which can be decomposed in a plane wave and a periodic function $|u_\nu(t)\rangle$ - the Floquet modes,

$$|\psi_\nu(t)\rangle = e^{-i\varepsilon_\nu t} \, |u_\nu(t)\rangle \tag{3.4.12}$$

and these states are solutions to the time-dependent Schrödinger equation.

$$i\partial_t \, |\psi_\nu(t)\rangle = \hat{H}(t) \, |\psi_\nu(t)\rangle \, , \quad |\psi_\nu(t)\rangle = U(t) \, |\psi_\nu(0)\rangle \tag{3.4.13}$$

where $|\psi_\nu(0)\rangle = |u_\nu(0)\rangle$ [2] and $U(t)$ is the time evolution operator. If the evolution is slow enough, the adiabatic theorem states that after one period, the state of the system returns to the initial state and acquires a phase α_n, i.e.

$$|\chi_n(\tau)\rangle \approx e^{i\alpha_n} \, |\chi_n(0)\rangle \tag{3.4.14}$$

This is the zeroth-order correction in the adiabatic perturbation theory [44]. This phase is a sum of the dynamical phase δ_n and the geometrical (Berry) phase γ_n,

[2] We identify the Floquet modes $|u_\nu(\tau)\rangle = |u_\nu(0)\rangle$ as the Floquet states $|\phi_\nu(\tau)\rangle$, the eigenstates of the Floquet operator, since at time $t = \tau$ we have $|\psi_\nu(\tau)\rangle = e^{-i\varepsilon_\nu \tau} \, |u_\nu(\tau)\rangle$ and $|\psi_\nu(\tau)\rangle = F(\tau) \, |u_\nu(0)\rangle$.

$$\alpha_n = \delta_n + \gamma_n, \quad \delta_n = -\int_0^\tau dt\, E_n(t), \quad \gamma_n = i\int_0^\tau dt\, \langle \chi_n(t)|\partial_t \chi_n(t)\rangle \tag{3.4.15}$$

Acting with the Floquet operator on the instantaneous eigenstate $|\chi_n(0)\rangle$ yields

$$|\chi_n(\tau)\rangle = U(\tau)\,|\chi_n(0)\rangle \approx e^{i\alpha_n}\,|\chi_n(0)\rangle \tag{3.4.16}$$

where we have exploited Eq. 3.4.14. At the same time, we recall the action of the Floquet operator on the Floquet mode at $t = 0$ (or equivalently Floquet states),

$$|\psi_\nu(\tau)\rangle = U(\tau)\,|u_\nu(0)\rangle = e^{-i\varepsilon_\nu \tau}\,|u_\nu(0)\rangle \tag{3.4.17}$$

Comparing Eq. 3.4.16 and Eq. 3.4.17, we conclude that the instantaneous eigenstates of the Hamiltonian $|\chi_n(0)\rangle$ coincide with the Floquet modes $|u_\nu(0)\rangle$ [3]. At the same time, the quasienergy ε_ν is associated with the geometrical and dynamical phases,

$$\varepsilon_\nu = -\frac{1}{\tau}\big(\delta_n + \gamma_n\big) \tag{3.4.18}$$

These results are essential when we discuss about quantized pumping of the Rice-Mele model.

[3] We note that we keep separate sets of indices for the Hamiltonian eigenstates and the Floquet modes. This is actually done to avoid confussion. Let us provide an example to illustrate this. The Hamiltonian ground state $n = 0$ does not necessarily correspond to $\nu = 0$ (even though we sort energies in increasing order), because the quasienergies are energies folded within a finite window of certain width. Thus, $\varepsilon_{\nu=0}$ does not trivially correspond to the ground state.

Chapter 4

Rice-Mele Model

The Rice-Mele model is one of the simplest examples of topological quantum pumping. Its significance is central because of the elegance and simplicity of the model in studying various perturbations and how topological systems respond to such effects [45, 28, 27]. The original Rice-Mele model [29] is actually a static model and is used to study excitations in diatomic polymers. The extension of it to a time-periodic system has profound consequences, which we will explore in this chapter, primarily the case of periodic boundary conditions. We study some key aspects of the Rice-Mele model which have topological character, and have an impact on observables.

4.1 Brief discussion on the concept of Thouless pumping

Topological quantum pump was first established by David Thouless [12]. In his remarkable paper, he showed that under a slow modulation of the potential $V(x,t)$ of a one-dimensional lattice of infinite size, the current is quantized in terms of the Chern number, which is associated to the system energy bands evolving in time. Importantly, the Fermi level must lie inside a gap that separates the filled and empty bands at all times. The expression for the current originates from a first-order correction within the adiabatic perturbation theory.

$$Q = -\frac{i}{2\pi}\sum_{n\in occ}\int_0^\tau dt\int_{BZ} dk\left[\left\langle\frac{\partial\psi_{n,k}}{\partial k}\middle|\frac{\partial\psi_{n,k}}{\partial t}\right\rangle - c.c.\right] \tag{4.1.1}$$

The quantity

$$\mathcal{B}^n_{kt} = i\left[\left\langle\frac{\partial\psi_{n,k}}{\partial k}\middle|\frac{\partial\psi_{n,k}}{\partial t}\right\rangle - c.c.\right] \tag{4.1.2}$$

is identified as the Berry curvature from Berryology [22]. The double integral of the Berry curvature of an occupied band over the surface of the torus formed by (k,t) is the Chern number, and it is reminiscent of the Gauss-Bonnett theorem in Mathematics [1]. This treatment resembles the one given in the original TKNN paper [23], where the linear response to an electric field is quantized in a similar fashion, and the two periodic parameters were (k_x, k_y). That is the reason that Thouless pumping is considered the dynamical 1D analog of the 2D static Hall effect.

[1]The Gauss-Bonnett theorem states that the integral of the Gaussian curvature over a two-dimensional manifold depends on a universal invariant, the genus (the number of holes on the manifold). It is because of this theorem that we can say a mug is topologically equivalent to a doughnut. We can map between the two geometries by continously deforming one into the other.

Essentially, each band is assigned a Chern number by integrating the associated Berry curvature. If the Fermi level lies within the gap, separating the occupied from the empty states, then the pumped charge is simply (minus) the sum of the Chern numbers of the bands.

It must be emphasized that the evolution must be slow enough that we avoid inducing excitations. Typically the driving frequency ω should be much smaller than the energy gap. If one fails to preserve adiabaticity, contributions from higher energy bands are considered to the current.

4.2 The driving protocol of the Rice-Mele model

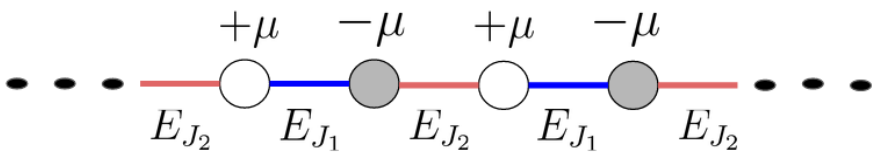

Figure 4.1: The Rice-Mele lattice model of staggering potential μ and hopping parameters $E_{J_{1/2}}$.

The Rice-Mele (RM) model resembles a one-dimensional lattice of N units cells and two sites per unit cell, with a total of $L = 2N$ sites. Particles, in particular fermions, are allowed to hop between different sites. There are two types of hoppings, intra-cell hopping E_{J_1} which involves particle hopping within the unit cell, and inter-cell hopping E_{J_2} which involves particle hopping between adjacent unit cells. The tunneling parameters and the on-site stagggered potential are varied periodically in time. The RM Hamiltonian reads,

$$\begin{aligned}\hat{H}_{RM}(t) = -E_{J_1}(t)\sum_{j=1}^{N}\left(\hat{c}^{\dagger}_{2j-1}\hat{c}_{2j} + h.c.\right) - E_{J_2}(t)\sum_{j=1}^{N} f_j\left(\hat{c}^{\dagger}_{2j}\hat{c}_{2j+1} + h.c.\right) \\ + \sum_{j=1}^{N}\left(\mu_A(t)\hat{c}^{\dagger}_{2j-1}\hat{c}_{2j-1} + \mu_B(t)\hat{c}^{\dagger}_{2j}\hat{c}_{2j}\right)\end{aligned} \tag{4.2.1}$$

where the summation index j runs over the number of unit cells. For completeness, we also define the coefficient f_j which depends on the boundary conditions of the system.

$$f_j = \begin{cases} 1 & PBC \\ 1 - \delta_{j,N} & OBC \end{cases} \tag{4.2.2}$$

We will mainly focus on the case of periodic boundary conditions, and thus $f_i = 1, \forall i \in \{1, 2, ...N\}$ [2], which is the most interesting and leads to quantized pumping. However, we will briefly discuss the OBC at the end of the chapter, because the associated Hamiltonian will be the relevant one when we study the coupling of the RM model with external leads in Chapter 6.

The parameters $E_{J_{1/2}}, \mu_{A/B}$ are varied periodically in time with driving frequency ω and period $\tau = 2\pi/\omega$. These admit the following form,

$$E_{J_{1/2}}(t) = E_{J_0} \pm \delta E \cos\omega t, \quad \mu_{A/B}(t) = \pm\mu = \pm\Delta \sin\omega t \tag{4.2.3}$$

[2]Note that for $j = N$, $\hat{c}_{2N+1} = \hat{c}_1$.

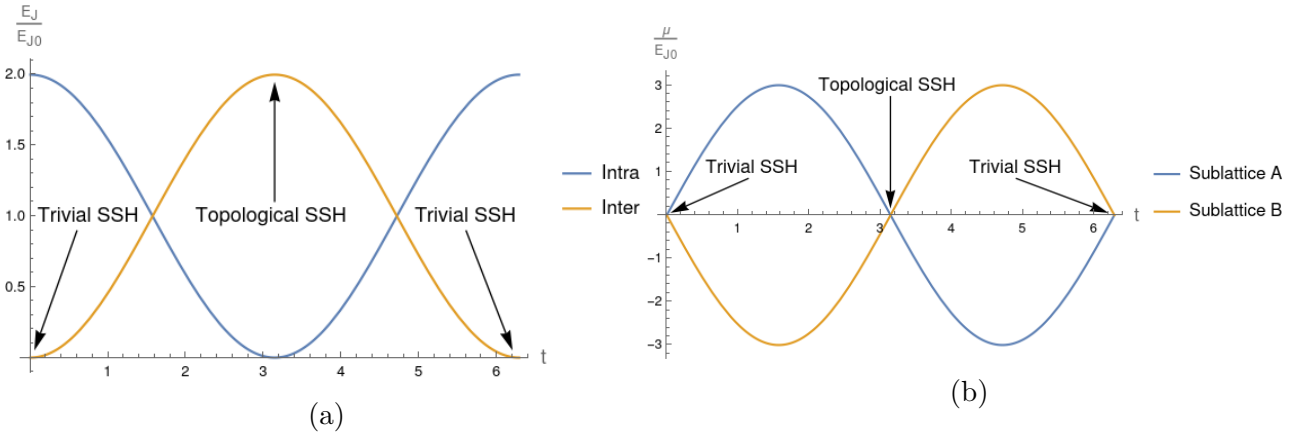

Figure 4.2: The pumping protocol of the Rice-Mele model for (a) the hopping parameters $E_{J_{1/2}}(t)$ and (b) the on-site staggered potential $\mu_{A/B}(t)$, for $\delta E = E_{J_0}$ and $\Delta = 3E_{J_0}$.

and this choice of modulation defines our pumping protocol. This specific choice of driving is not unique, but as it turns out, it is a suitable one leading to quantized transport. Figures 4.2a and 4.2b present the form of the time-dependent parameters. It is evident that within a driving period, the system exhibits both the trivial and topological phases of the SSH model (Appendix A). At these points, $\mu_{A/B} = 0$ while the hoppings are, in general, non-zero, thus allowing particles to hop.

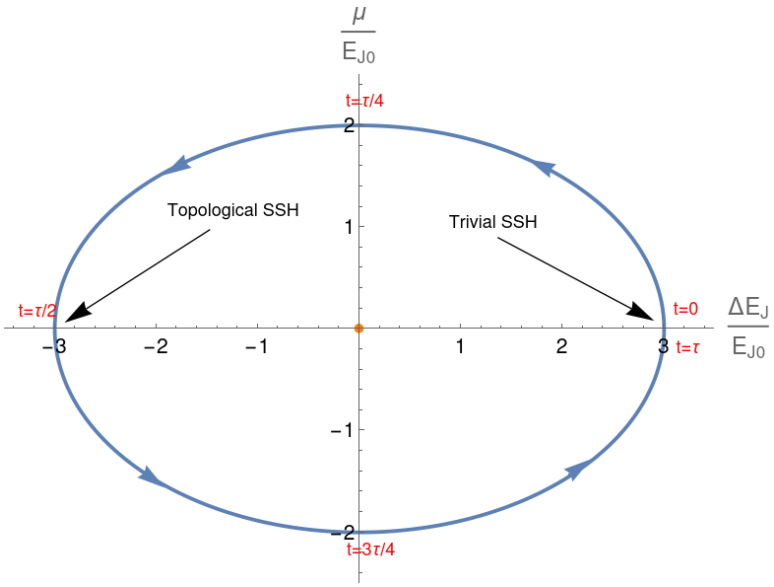

Figure 4.3: The pumping protocol on the ΔE_J - μ plane, where the ellipse of Eq. 4.2.4 encircles the gapless point (orange dot), for $\Delta = 2E_{J_0}$ and $\delta E = 1.5E_{J_0}$.

We can combine the expressions given in 4.2.3 as to remove the parametric dependence on t,

$$\left.\begin{array}{lll} \Delta E_J = 2\delta E \cos\omega t & \Rightarrow & (\Delta E_J)^2 = (2\delta E)^2 \cos^2\omega t \\ \mu = \Delta \sin\omega t & \Rightarrow & \mu^2 = \Delta^2 \sin^2\omega t \end{array}\right\} \Rightarrow \frac{(\Delta E_J)^2}{(2\delta E)^2} + \frac{\mu^2}{\Delta^2} = 1 \qquad (4.2.4)$$

where $\Delta E_J = E_{J_1} - E_{J_2}$. The resulting curve is that of an ellipse on the δE_J - μ plane and is displayed in Fig 4.3. As time grows, the system 'moves' counterclockwise along the ellipse,

exhibiting both the trivial and topological phases of the SSH model. At the same time, notice that the ellipse winds around the origin, the point corresponding to $E_{J_1} = E_{J_2}$ and $\Delta = 0$. This is the gapless point since at this exact point, the energy band gap closes, thus the system is in a metallic phase. We will show this explicitly in Subsection 4.4. When the ellipse winds around the gapless point, this is linked with non-trivial topology, in a similar fashion as in the SSH model. We recall that in the SSH model we are concerned with the winding of the relevant ellipse about the gapless point on the E_{J_1} vs E_{J_2} plane. In the Rice-Mele model, by mapping to momentum space, we can show that the gapless point is directly connected to a Berry monopole in the parameter space. At the same time, the ellipse corresponds to a closed surface in this parameter space. Thus, we can imagine a surface enclosing the monopole, and finds a magnetic analogue. The non-zero flux on the surface corresponds to non-trivial topology. This brief analysis does not demonstrate how observables are influenced by the underlying nontrivial topology. However, the above argument ensures the existence of the latter.

The pumping protocol given by Eq. 4.2.4 and depicted in Figure 4.3, ensures that the system is in a topological phase, since the ellipse encircles the origin irrespective of the values of $E_{J_0}, \delta E, \Delta$, unless $\delta E = 0$ or $\Delta = 0$ or both. To 'exit' the topological phase, we add an energy shift A to one of the hopping parameters, for instance in E_{J_1}.

$$E_{J_1} = E_{J_0} + \delta E \cos \omega t + A \tag{4.2.5}$$

We note that this is a perturbation we consider here, for the sake of discussing the related topological phase transition. However, in the following sections and chapters, the perturbation A is set to zero, unless otherwise stated. Then the equation of the ellipse changes slightly, with A appearing as a shift on the x-axis.

$$\frac{(\delta E_J - A)^2}{(2\delta E)^2} + \frac{\mu^2}{\Delta^2} = 1 \tag{4.2.6}$$

We notice that the ellipse does not wind around the gapless point anymore when $A > 2\delta E$, and thus we enter the topologically trivial phase. In the picture we set up earlier, this ellipse corresponds to a closed surface that does not enclose the monopole, thus the outward flux through the surface is zero, thus trivial topology.

4.3 The current operator

We now discuss the current operator, the relevant observable linked to transport. The integral of the expectation value of the current is the pumped charge.

$$Q = \frac{1}{\tau} \int_0^\tau dt \ \langle \mathcal{J} \rangle (t) \tag{4.3.1}$$

For the derivation of the expression for the current operator, we follow [46].

We will employ a small trick by introducing a fictitious flux through the system, in which in the case of periodic boundary conditions has the geometry of a ring. The insertion of this magnetic flux results in the appearance of an Aharonov-Bohm [47] phase, which can be uniformly distributed along the links of the chain.

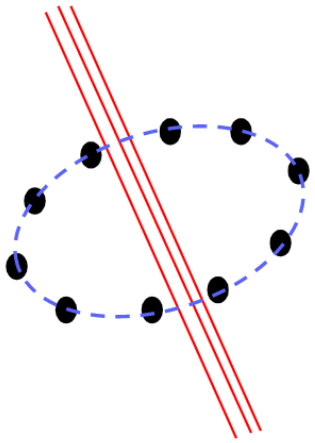

Figure 4.4: A flux passes through the a system with periodic boundary conditions

In a tight-binding model, the introduction of such a flux casts the hopping parameter from a real quantity to a complex one through the Peierls substitution.

$$-E_J c_{j+1}^\dagger c_j \mapsto -E_J e^{i\theta_j} c_{j+1}^\dagger c_j, \quad \theta_j = \frac{q}{\hbar c}\int_j^{j+1} \mathbf{A}\cdot d\mathbf{l} \tag{4.3.2}$$

The line integral of the vector potential is done along the length of the link connecting the sites j and $j+1$. There is zero magnetic field in the region outside the flux, and we choose a radial vector potential with azimuthal symmetry. At radius R where the ring exists, the vector potential will be constant, and is taken out of the line integral.

$$\int_j^{j+1} \mathbf{A}\cdot d\mathbf{l} = |\mathbf{A}|\int_j^{j+1} dl = |\mathbf{A}|\frac{1}{L}\oint dl = \frac{1}{L}\oint |\mathbf{A}|dl = \frac{1}{L}\iint BdS = \frac{1}{L}\Phi \tag{4.3.3}$$

where Φ is the overall flux, penetrating the ring, and it is constant in value. The sum over all θ_j is the gauge invariant quantity, and matches the flux due to the Stoke's theorem. The phase now becomes (considering $\hbar = 1, c = 1$)

$$\theta_j = q\frac{\Phi}{L} \tag{4.3.4}$$

Let us now view our system in first quantization. The Hamiltonian in one-dimension under the minimal substitution is

$$H = \sum_i \left[\frac{(p_i + \hbar\kappa_i)^2}{2m} + V(x_i)\right] \tag{4.3.5}$$

where $\hbar\kappa_i = qA$ (assuming all particles carry the same charge), and $A = \left|A(\vec{x})\right|$ is the vector potential or gauge field. We take the derivative with respect to the momentum κ_i, and then we let $\kappa_i \to 0$ to remove the fictitious flux.

$$\frac{1}{\hbar}\frac{\partial H}{\partial \kappa_j} = \sum_i \left[\frac{(p_i + \hbar\kappa_i)}{m}\delta_{ij}\right] = \frac{(p_j + \hbar\kappa_j)}{m} \quad \xrightarrow{\kappa_j \to 0} \quad \frac{p_j}{m} = v_j \tag{4.3.6}$$

The current operator is then given by qv_j where q is the charge of the particle. We can express the current in units of the charge, and thus write,

$$\mathcal{J}_j = \frac{\partial H}{\partial \kappa_j}\bigg|_{\kappa_j=0} \qquad (\hbar = 1) \tag{4.3.7}$$

The constant vector potential is written as $|A| = \Phi/L, (\hbar = 1)$ and thus $\kappa_j = \Phi/L$. Equivalently, we can write the current operator in terms of the flux or the phase associated with this flux.

$$\mathcal{J}_j = L\frac{\partial H}{\partial \Phi}\bigg|_{\Phi=0} = \frac{\partial H}{\partial \theta_j}\bigg|_{\theta_j=0} \tag{4.3.8}$$

Let us return to Rice-Mele tight-binding model and introduce a fictitious [3] flux. Only the kinetic term in the Hamiltonian will be affected by this effect. Because of this, the current operator reduces to the derivative of the kinetic energy with respect to the flux, as one might expect. According to Peierls substitution, the hopping parameters become complex, $\tilde{E}_{J_1} = E_{J_1}e^{-i\theta_j}$ and $\tilde{E}_{J_2} = E_{J_2}e^{-i\theta_{j+1}}$ where $\theta_{j/j+1} = q\Phi/L$. Then, the kinetic part of the Hamiltonian becomes

$$\hat{T}_{RM} = -\sum_j \left(\tilde{E}_{J_1}\hat{c}^\dagger_{2j-1}\hat{c}_{2j} + h.c.\right) - \sum_j \left(\tilde{E}_{J_2}\hat{c}^\dagger_{2j}\hat{c}_{2j+1} + h.c.\right) \tag{4.3.9}$$

Then, we take the derivative of the Rice-Mele Hamiltonian with respect to the flux based on Eq. 4.3.4.

$$\hat{\mathcal{J}} = \frac{1}{L}iq\left[E_{J_1}\sum_j \left(\hat{c}^\dagger_{2j-1}\hat{c}_{2j} - h.c.\right) + E_{J_2}\sum_j \left(\hat{c}^\dagger_{2j}\hat{c}_{2j+1} - h.c.\right)\right] \tag{4.3.10}$$

4.4 The origins of quantized transport in the RM model

4.4.1 The momentum space formalism

Let us study now the Rice-Mele model with periodic boundary conditions. It feels natural to us to switch to the momentum space since the relevant Hamiltonian possesses space translation symmetry. We map to the k-space where k is the crystal momentum, with a Fourier transformation. Because of the lattice having a two-site unit cell, the initial Hilbert space maps to a composite space, that of the momentum and two-dimensional sublattice space $\{A, B\}$.

$$\hat{H}_{RM}(t) = \sum_k C^\dagger_k\, \mathcal{H}(k,t)\, C_k, \quad C_k = \begin{pmatrix} c_{k,A} \\ c_{k,B} \end{pmatrix} \tag{4.4.1}$$

where the Hamiltonian $\mathcal{H}(k,t)$ is a 2×2 matrix and can be written in the following compact form.

$$\mathcal{H}(k,t) = \vec{R}(k,t)\cdot\vec{\sigma}, \quad \vec{R}(k,t) = \Big(R_x(k,t), R_y(k,t), R_z(k,t)\Big) \tag{4.4.2}$$

where $\vec{\sigma}$ are the Pauli matrices in the sublattice space. $\mathcal{H}(k,t)$ resembles a system of a spin-1/2 particle in a 'magnetic' field $\vec{R}(k,t)$. The components of the field $\vec{R}(k,t)$ are functions of the time-dependent parameters of the RM Hamiltonian.

[3] This argument also applies for a true magnetic field.

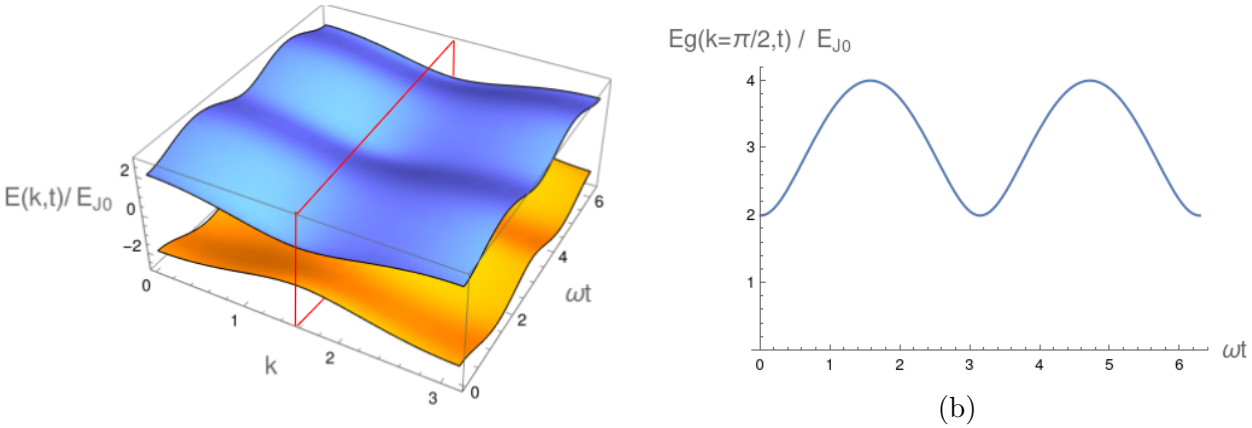

(a) (b)

Figure 4.5: The spectrum of the Rice-Mele model. (a) The two energy bands $\varepsilon_\pm(k,t)$ are periodic functions of k,t. The minimum gap is located at the center of the Brillouin zone, and (b) along the time direction at $t = 0, \pi/2$.

$$R_x(k,t) = -E_{J_1}(t) - E_{J_2}(t)\cos(2k), \quad R_y(k,t) = -E_{J_2}(t)\sin(2k), \quad R_z(k,t) = \Delta \sin \omega t \tag{4.4.3}$$

The components $R_i(k,t)$ are periodic function of the crystal momentum k and time t. The spectrum of the Hamiltonian $\mathcal{H}(k,t)$, depicted in Figure 4.5a, is symmetric with respect to zero,

$$\varepsilon_\pm(k,t) = \pm\left|\vec{R}(k,t)\right|, \quad E_g(k=\pi/4,t) = 2\left|\vec{R}(k=\pi/4,t)\right| \tag{4.4.4}$$

The minimum gap is at the point $2k = \pi/2$ and $t = 0, \tau/2$ (see Figure 4.5b). The chemical pontential term vanishes and we retrieve the SSH model, thus we expect the minimum gap to exist at these time moments. The gap takes the simple form of $E_g^{(min)} = E_g(\pi/2, \tau/2) = 4\delta E$, thus depends only on the value of the amplitude of the modulation of the hopping parameters δE. The adiabatic limit is established when the gap $E_g^{(min)}$ is much larger than the driving frequency ω.

The eigenstates of the Hamiltonian $\mathcal{H}(k,t)$ take the following form,

$$|u_\pm(k,t)\rangle = \left|u_\pm(\vec{R})\right\rangle = \alpha_\pm |\uparrow\rangle + \beta_\pm |\downarrow\rangle \tag{4.4.5}$$

where the states $\{|\uparrow\rangle = \begin{pmatrix}1 & 0\end{pmatrix}^T, |\downarrow\rangle = \begin{pmatrix}0 & 1\end{pmatrix}^T\}$ correspond to sublattices A and B, respectively. The coefficients $\alpha_\pm, \beta_\pm$, where $\pm$ correspond to the upper and lower band, are,

$$\alpha_\pm = \pm\frac{e^{-i\phi}}{\sqrt{2}}\sqrt{1 \pm \frac{R_z}{R}}, \quad \beta_\pm = \frac{1}{\sqrt{2}}\sqrt{1 \mp \frac{R_z}{R}} \tag{4.4.6}$$

where $\phi = \arctan(R_y/R_x)$ and $R = \left|\vec{R}\right|$.

4.4.2 Berry Picture

As we have demonstrated, the Hamiltonian of the Rice-Mele model in the momentum space resembles a system of a spin-1/2 in a magnetic field $\vec{R}$, i.e. $H = \vec{R} \cdot \vec{\sigma}$. The system evolves

adiabatically in the parameter space, formed by $\{R_i\}$, and returns to itself after the evolution of one period, but during its journey along some closed curve in the parameter space, it acquires a phase, the famous Berry phase. In fact, this problem was one of the first applications of his theory [22].

In Berry theory, one asks to determine the Berry connection and curvature for each eigenstate of the Hamiltonian,

$$\mathcal{A}_{\pm}(\vec{R}) = i \left\langle u_{\pm}(\vec{R}) \middle| \nabla_{\vec{R}}\, u_{\pm}(\vec{R}) \right\rangle, \quad \mathcal{B}_{\pm}(\vec{R}) = \nabla_{\vec{R}} \times \mathcal{A}_{\pm}(\vec{R}) \tag{4.4.7}$$

The resemblance to the spin-1/2 problem is apparent especially if we express the eigenstates of the k-space Rice-Mele Hamiltonian Eq. 4.4.5 in terms of the polar and azimuthal angles of the spherical coordinate system,

$$|u_{+}(\theta,\phi)\rangle = \begin{pmatrix} e^{-i\phi}\cos\frac{\theta}{2} \\ \sin\frac{\theta}{2} \end{pmatrix}, \quad |u_{-}(\theta,\phi)\rangle = \begin{pmatrix} -e^{-i\phi}\sin\frac{\theta}{2} \\ \cos\frac{\theta}{2} \end{pmatrix} \tag{4.4.8}$$

where $\theta = \arccos(R_z/R)$, and thus the eigenstates live on the Bloch sphere. By following a similar procedure to the spin-1/2 problem and after a few calculations, the Berry curvature of the eigenstates has the form of a radial magnetic field generated by a monopole of charge $q_m = 1/2$, located at the origin $\vec{R} = 0$.

$$\mathcal{B}_{\pm}(\vec{R}) = \mp\frac{1}{2}\frac{\hat{R}}{R^2}, \quad \text{where} \quad \hat{R} = \frac{\mathbf{R}}{R} \tag{4.4.9}$$

The $\vec{R} = 0$ point is a degeneracy/gapless point, at which the energy bands Eq. 4.4.4 touch. By examining the explicit form of $\vec{R}(k,t)$ as a function of k and t Eq. 4.4.3, we find that $\vec{R} = 0$ when $E_{J_1} = E_{J_2}$ and $\Delta = 0$ for all values of (k,t). Therefore, the gapless point is implies the existence of a Berry monopole in the parameter space of $\vec{R}$!

By choosing a set of values for the parameters of the Hamiltonian $\{E_{J_0}, \delta E, \Delta\}$, we realize a closed surface in the parameter space of $\vec{R}$. In Figure 4.6a, the resulting closed surface encloses the monopole. This has a nice analogue with electromagnetism and the hypothetical magnetic monopole. We can think of the latter as the Berry monopole situated at the origin and the magnetic field that generates is the Berry curvature. Integrating the magnetic field over a closed surface yields the flux. Additionally, Gauss' law says that the closed integral of the magnetic field is equal to the enclosed charge. Therefore, in exact analogy with electromagnetism, for our problem we take the surface integral of the Berry curvature,

$$\oiint_S \mathcal{B}_{\pm}(\vec{R}) \cdot d\mathbf{S} = 4\pi q_m = \mp 2\pi \tag{4.4.10}$$

It is explicitly shown in Ref. [46], using up to first-order in adiabatic perturbation expansion, that the pumped charge is written in terms of this surface integral [4] and thus it turns out to be quantized in units of the particle charge, i.e.

$$Q_{\pm} = -\frac{1}{2\pi}\oiint_S \mathcal{B}_{\pm}(\vec{R}) \cdot d\mathbf{S} = \pm 1 \tag{4.4.11}$$

[4] In Thouless pumping, the surface integral of the Berry curvature is also interpreted as the first Chern number, defined on the torus (k,t).

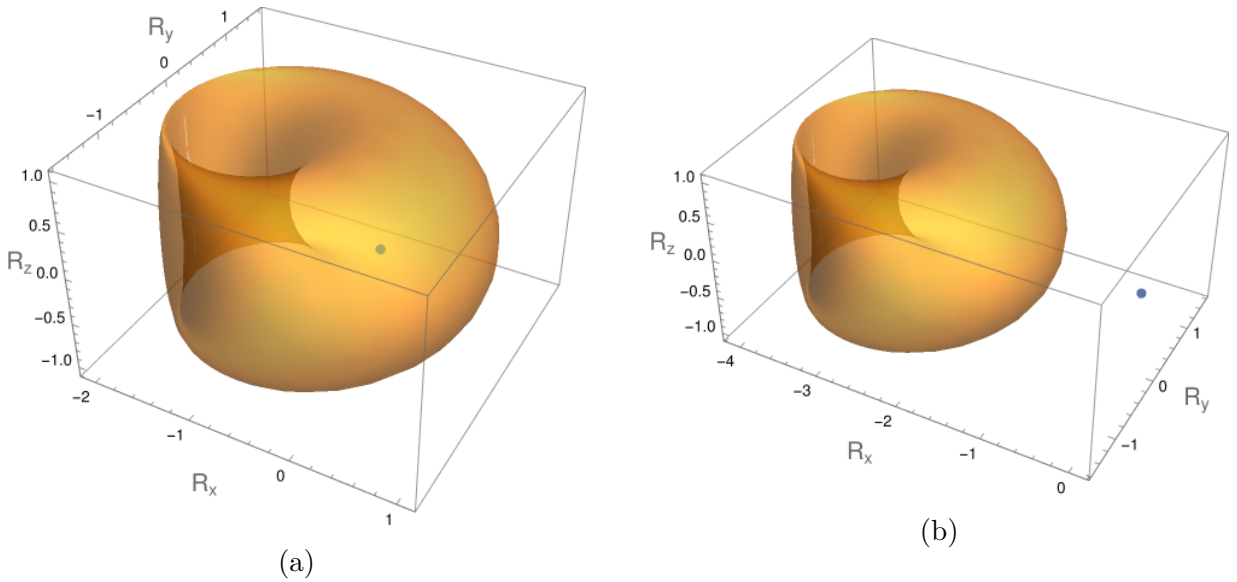

Figure 4.6: When a two-dimensional surface in the $\vec{R}$ parameter space (a) encloses the Berry monopole or equivalently the gapless point, the flux passing through the surface is nonzero, and thus the pumped charge is nonzero, assuming adiabaticity. Otherwise, (b) the flux is zero as well as the pumped charge. The surface in (a) corresponds to $\delta E = 0.5E_{J_0}, \Delta = E_{J_0}, A = 0$, while in (b) to $\delta E = 0.5E_{J_0}, \Delta = E_{J_0}, A = 2E_{J_0}$.

4.4.3 Floquet Picture

We now change perspective and we tackle pumping in the Rice-Mele model within the Floquet picture (Chapter 3). In this context, we are concerned with the Floquet operator which is obtained by the time evolution operator at time τ. Because of space translational invariance, the original Hilbert space is reduced to a composite space of the sublattice space and momentum space. The time evolution operator, just like the Hamiltonian in Subsection 4.4.1, is decomposed as follows,

$$U(t) = \sum_k U_k(t) \otimes |k\rangle \langle k| \tag{4.4.12}$$

At the stroboscopic time $t = \tau$, we obtain the Floquet operator labelled by the momentum index, $F_k(\tau) \equiv U_k(\tau)$. Diagonalization of the Floquet operator yields the quasienergies $\varepsilon_{\nu,k}$, or equivalently the Floquet bands, defined within the first Floquet-Brillouin zone (see Figure 4.7b). We emphasize that the quasienergies are uniquely determined within the interval $\varepsilon_{\nu,k} \in [0, \omega)$, and they are folded within this range. This is similar to the Bloch theorem, Figure 4.8, in which the parabola of the free electron is distorted by the weak periodic potential, is folded and thus defined within the Brillouin zone. The 'pattern' is then repeated across the whole crystal momentum direction (Fig. 4.8c). In fact, the repeated zone is the spectrum obtained by the extended Hamiltonian in the Floquet-Shirley approach back in Section 3.3 in which the Floquet-Brillouin zone is repeated across the quasienergy direction.

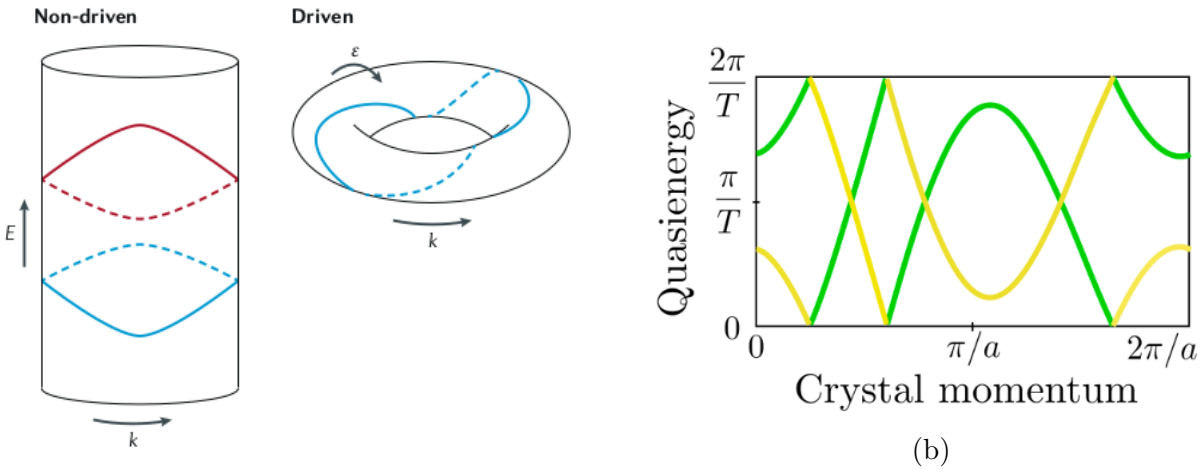

(a) (b)

Figure 4.7: (a) A periodic drive in a 1D band insulator changes the geometry of the spectrum. Adapted from [48]. (b) The Floquet-Brillouin zone for the Rice-Mele model. The Floquet bands wind in opposite direction thus generate a current of different sign. The right-moving and left-moving bands are colored green and yellow respectively. Adapted from [49].

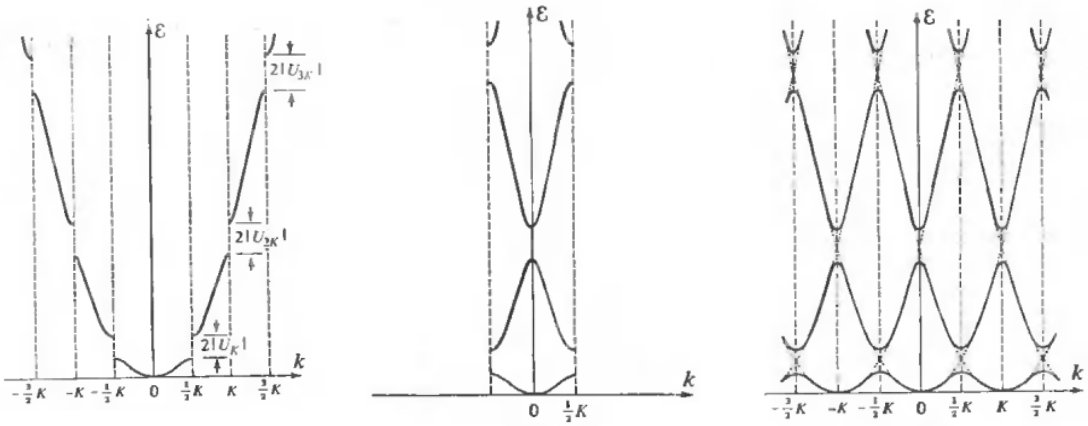

(a) (b) (c)

Figure 4.8: An illustration of the folding of bands in the Bloch theorem. (a) The effect of Bragg planes on the free electron, in the presence of other electron. This is the extended-zone scheme. (b) The folding of the bands correspond to the reduced-zone scheme. (c) The 'pattern' is repeated forming the repeated-zone scheme. Figures adapted from [39].

Because of the double periodicity in momentum $k \in S^1$ and quasienergy $\varepsilon_\nu \in S^1$, the Floquet-Brillouin zone has the geometry of a torus, i.e. $T^2 = S^1 \times S^1$. This feature has indirect impact to the pumped charge, which we now explore.

From solid state physics, the group velocity of the band ν is given by the derivative of the band with respect to the crystal momentum, i.e. $v_{\nu,k} = \partial_k \varepsilon_{\nu,k}$. If we are interested in the average group velocity over the Brillouin zone, then all we have to do it take the integral over the zone,

$$\langle v_{g,\nu} \rangle = a \int_{BZ} \frac{dk}{2\pi} \, v_{\nu,k} = a \int_{BZ} \frac{dk}{2\pi} \, \partial_k \varepsilon_{\nu,k} \tag{4.4.13}$$

where a is the size of the unit cell [5]. The current is given by $\langle j_\nu \rangle = \rho \langle v_{g,\nu} \rangle$ where the particle density ρ is taken to be that of the half-filling, i.e. $\rho = 1/a$. Therefore the current adopts the following form,

$$\langle j_\nu \rangle = \int_{BZ} \frac{dk}{2\pi} \partial_k \varepsilon_{\nu,k} \tag{4.4.14}$$

The integral expresses the winding of the quasienergy over the whole Brillouin zone, and thus it is an integer,

$$\langle j_\nu \rangle = \frac{W_\nu}{\tau} \tag{4.4.15}$$

where W_ν is the winding number of the Floquet band ν [6]. This results states that the average current, and therefore the pumped charge, is quantized in terms of the winding number. If the quasienergy winds trivially around the Floquet-Brillouin zone as we run along the k direction, then the average current is zero. However in the case of the Rice-Mele model, the quasienergies wind non-trivially as it is apparent from Figure 4.7b, and thus the current is non-zero. In fact, they wind exactly once as K goes from 0 to 2π, one clockwise, the other counterclockwise and thus the resulting currents have opposite signs. If the system was initialized in the one of the Floquet bands at half-filling, then the above analysis ensures that transport will be quantized.

The above discussion is applied when the adiabatic limit has been established, and the system is in one of the Floquet bands. When we move away from this limit, then the pumped charge involves contributions from both Floquet bands and thus it is no longer quantized. In this case, Eq. 4.4.14 generalizes to the following [44],

$$Q = \tau \sum_\alpha \int_0^{2\pi} \frac{dk}{2\pi} n_{\alpha,k} \partial_k \varepsilon_{\alpha,k} \tag{4.4.16}$$

where $n_{\alpha,k}$ are the occupations of the Floquet bands. When one of the Floquet states are occupied, $n_{\alpha,k} = \delta_{\nu,\alpha}$ we retrieve Eq. 4.4.14.

We close this discussion with a remark. A non-driven one-dimensional insulator will have a trivial band topology since the band structure has the geometry of a cylinder. When the system is driven periodically in time, then the energy direction inherits the time periodicity in the form of the quasienergies and the band structure now has the geometry of a torus, as seen in Figure 4.7a. Thus, bands living on this torus may be topologically non-trivial depending on how they wrap around the torus.

4.5 The impact of perturbations on pumping

Thouless pumping requires the slow modulation of the Hamiltonian in time, and slow means adiabatically [7]. In terms of energy scales this is translated into the driving frequency being much smaller than the energy gap. such that particle-hole excitations are suppressed. Furthermore, it assumes an infinite system such that the Chern number is established and thus pumping is quantized. However, in realistic scenarios we deal with finite systems and also

[5] In general, the size of the unit cells is set to unity, however here it is reinstated.

[6] The appearance of τ here comes by redefining the domain of the quasienergy $\mathcal{E}_\nu \to \mathcal{E}_\nu/\omega \in S^1$.

[7] There is theoretical evidence that one has quantized transport even in finite speeds, through some technique called shortcuts to adiabaticity (STA) [50].

nonadiabatic effects may take place due to finite frequency. We address these two factors and their impact on pumping in the following subsections, starting from finite size effects.

In the following results, we plot the pumped charge in the infinite-time limt, Eq. 3.4.9. We find the time-evolution operator, and diagonalize it at $t = \tau$ to obtain the Floquet states. The current operator is given by Eq. 4.3.10. The system is initialized in the lower band, therefore at half-filling. We work in real space representation, in the single-particle basis.

4.5.1 Finite size effects

Topological quantum pump is achieved in a system with space periodicity and of infinite size (the integral over the Brillouin zone expresses exactly this). Since we are concerned with the Rice-Mele model as the simplest example of a topological quantum pump, let us view how the pumped charge is affected by considering a finite lattice. One expects that as $L \to \infty$, the pumped charge approaches the value of one.

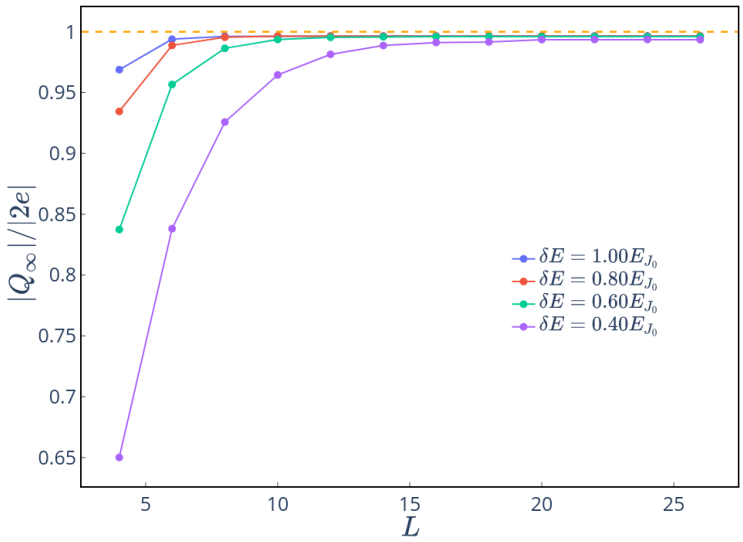

Figure 4.9: The dependence of the pumped charge on the system size for various values of the amplitude of the modulation of the hopping parameters δE. This concerns the Rice-Mele model with periodic boundary conditions. The parameters chosen here are $\Delta = 3E_{J_0}, \omega = 0.05E_{J_0}$.

Figure 4.9 presents the behavior of the pumped charge as a function of the system size, for a few values of the amplitude of modulations of the hopping parameters δE. As the system size increases, the pumped charge tends to approach the quantized value of one, as predicted in Thouless pumping. However, deviations from the quantized value are observed in smaller system size, and these deviations are stronger with decreasing δE.

4.5.2 Nonadiabatic effects

We discuss now about nonadiabatic effects in Thouless pumping. When we violate adiabaticity, particle-hole excitations appear in the system and the upper band starts being populated. Then, a particle current moving in the opposite direction is introduced and causes reduction in the net particle current, and thus deviations from the quantized value. This

aligns with the fact that in a gapped, topological two-band system, each band is 'assigned' with an integer Chern value.

In order to study the effect of nonadiabaticity on quantized pumping, one exploits the adiabatic perturbation theory [28] for small, yet finite driving frequencies. The first-order correction from the expansion, assuming that we suddenly switch on the driving with an 'infinite' acceleration, reveals a deviation from the quantized value by an amount that depends on ω^2, i.e.

$$Q(\omega) \approx 1 - A\omega^2 \tag{4.5.1}$$

The quadratic dependence of the pumped charge on the frequency for small values of it is shown in Figure 4.10a for the Rice-Mele model. As the frequency increases, it supplies sufficient energy to the system, enabling excitations to take place. Consequently, the upper band of the system begins to fill up, leading to a decrease in current, as we have previously discussed. When the frequency becomes approximately half of E_{J_0}, we are well beyond the adiabatic limit, and the pumped charge behaves in a quite unpredictable way.

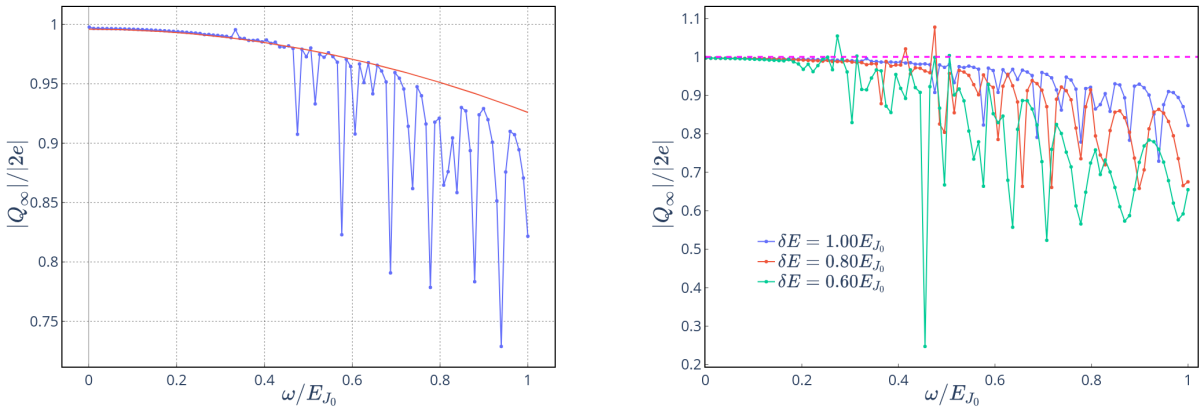

(a) (b)

Figure 4.10: Nonadiabatic effects on pumping of the Rice-Mele model. (a) The deviations from the quantized value are characterized by a quadratic trend (red line) on the frequency, for small values of it. As we keep increasing the frequency, pumping breakdowns completely. $\delta E = 1E_{J_0}, \Delta = 3E_{J_0}, L = 20$. (b) The dependence of the pumped charge on the driving frequency, for various values of δE. Smaller values of δE leads to earlier breakdown of pumping because of reduction in the value of the minimum gap. $\Delta = 3E_{J_0}, L = 20$.

It is also interesting to study the nonadiabatic breakdown of topological pumping for various values of δE. In this case, we recall the expression for the minimum gap of the Rice-Mele model $E_g = 4\delta E$. Because of the dependence of the gap on δE, we expect that as we increase the driving frequency, for smaller values of δE, the breakdown will appear 'earlier' compared to values of $\delta E \sim 1$. In other words, as the gap decreases because of decreasing δE, adiabaticity ceases to hold at smaller values of the driving frequency (see Figure 4.10b).

4.6 Open boundary conditions

We conclude this chapter by considering the Rice-Mele model with open boundary conditions. In this scenario, because of the finite size and the boundary, it seems that we can

pump particles towards the right for a while, assuming that we initialize the system in the lower band. It seems that all particles will pile up to the right edge. The existance of the zero-energy edge modes however, ensures that that will not occur. The edge modes move particles between the bands, and in particular the right edge mode moves a particle from a $E < 0$ to a $E > 0$ eigenstate, while the left edge mode does the opposite. This mechanism ensures the existence of a net particle current, however not quantized in any way. There are two contributions to the overall current, one coming from the lower band and one from the upper. Thus, by comparing the number of occupied $E < 0$ eigenstates and the number of occupied $E > 0$ eigenstates, we can deduce the direction of the current.

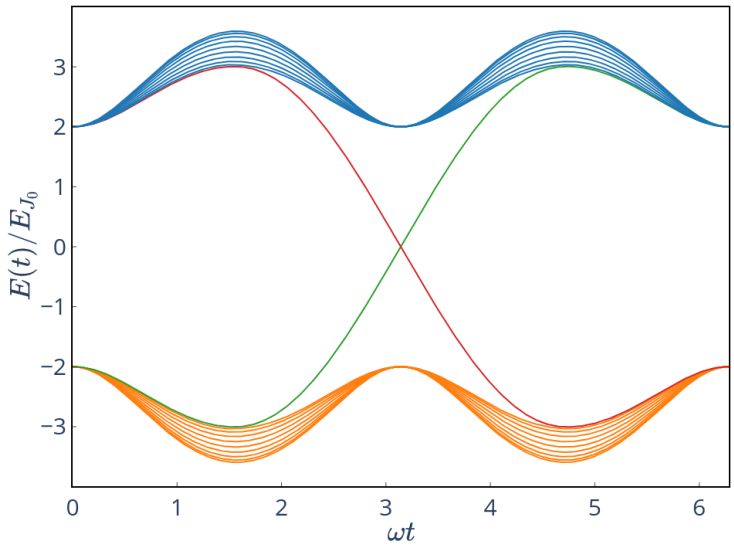

Figure 4.11: The instantaneous spectrum of the Rice-Mele model with open boundary conditions for $\delta E = E_{J_0}, \Delta = 3E_{J_0}, L = 20$. The right (green) edge mode moves a particle from the lower band to the upper band, which generates a particle current to the opposite direction. Likewise, the left edge mode moves a particle from the upper to the lower band.

Even though the physics of the open boundary Rice-Mele model might not be as rich as those of the periodic counterpart, however it will be the basis for the setup in Chapter 6, when we include external leads in the JJA setup.

Chapter 5

Disorder and the 1+1D to 2+0D mapping

A remarkable feature of topological systems is the robustness they display against disorder. In this Chapter, we examine static disorder in the Rice-Mele model with periodic boundary conditions by exploiting the Floquet theory. First the pumped charge is evaluated using the infinite-time limit formula. Then, we use the 1+1D to 2+0D mapping from Section 3.3 in combination with diagnostic tools of topological phases, namely the local Chern marker and the strange correlation function, to examine the system in the presence of disorder.

5.1 Pumping with disorder

In this section, we will discuss the Rice-Mele model with periodic boundary conditions, in which we introduce static, on-site disorder of the following form,

$$\hat{H}_{dis} = \sum_i \delta\mu_i \, \hat{c}_i^\dagger \hat{c}_i \tag{5.1.1}$$

such that $\hat{H}(t) = \hat{H}_{RM}(t) + \hat{H}_{dis}$. The parameters $\delta\mu_i$ are random variables, sampled from a uniform distribution $\mathcal{U} = [-w, w]$, where w is the strength of the disorder. Because of the nature of this disorder term, the total Hamiltonian does not possess discrete space translational symmetry, and therefore we cannot work in the momentum space. Our analysis and calculations are done in real space, in the single particle basis. We want to study the effect of the disorder on current quantization. When evaluating observables, we have to consider an ensemble of disorder configurations, and evaluate the pumped charge for each of these configurations. Then, the pumped charge is the average over these values,

$$\bar{Q} = \frac{1}{N} \sum_{n=1}^{N} Q_n \tag{5.1.2}$$

where n labels the configuration index. The pumped charge for each disorder configuration, is evaluated at the infinite-time limit provided by Eq. 3.4.9. Along the lines of Thouless et al [25], we also will track the behavior of the (minimum) energy gap E_g as we increase the disorder strength. The system is at half-filling, therefore the relevant gap is the particle-hole excitation gap. Evidently (see Figure 5.1a), while increasing disorder in the system, the energy gap reduces in value until it closes completely. At the same time, in Figure 5.1b, the pumped charge remains quantized and robust against disorder as long as the gap remains opens. Once the gap approaches zero, then the charge ceases to be quantized. However, notice that even

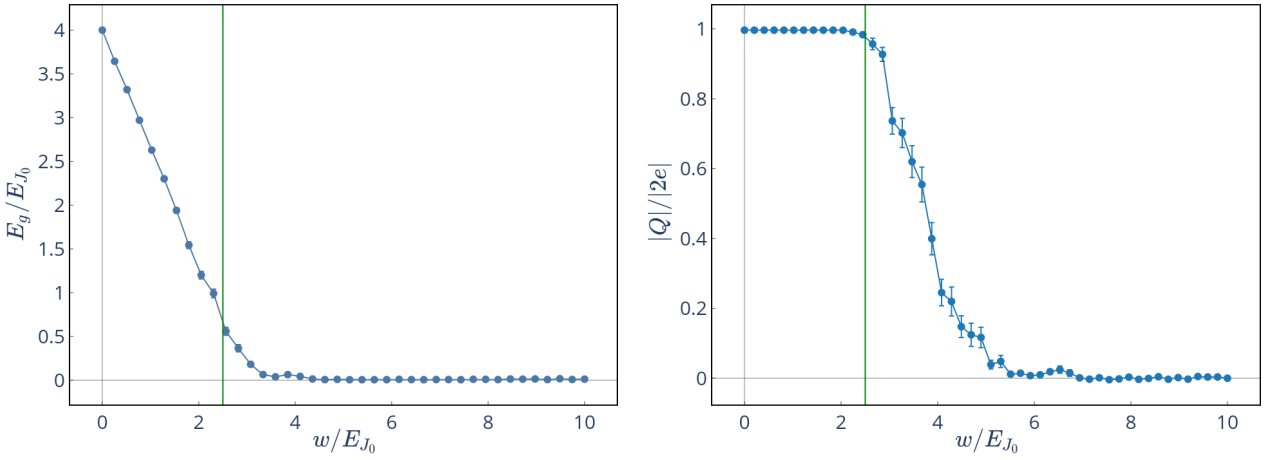

(a) (b)

Figure 5.1: The effect of the disorder on pumping in the Rice-Mele model. The pumped charge remains quantized in the presence of disorder as long as adiabaticity holds and the gap is open. Otherwise, a disorder-driven phase transition is observed which leads to a trivial state in which the current is zero. Parameters: $\delta E = E_{J_0}, \Delta = 3E_{J_0}, \omega = 0.05E_{J_0}, L = 20, N_{config} = 100$

when the gap closes entirely, we still observe a non-zero, yet non-quantized current flowing through the system.

There is a disorder-driven phase transition occuring here. We can distinguish three regions in Figure 5.1b; for $w < 2.5E_{J_0}$ the system is in the topological phase and remains robust against disorder since the current remains quantized. The non-zero current flow implies that we are in a delocalized phase. This occurs as long as the energy gap remains open. Between $w \approx 2.5E_{J_0}$ and $w \approx 6E_{J_0}$ the system is in a transition stage, in which the gap has been closed and the bands have been mixed but there is still some current flowing, indicating that delocalized states are still present. In the region $w > 6E_{J_0}$, there is no current while the gap remains closed, an indication that the system has well passed into an insulating phase. In the strong disorder regime, the Floquet states become localized and thus the current vanishes [44].

Let us summarize and comment on the sequence of events that took place. By increasing the strength of the disorder, the system undergoes a phase transition from a topological phase to a trivial phase. This is reflected by the integrated current, which is quantized and robust against moderate disorder in the topological phase, while it vanishes in the trivial phase. We can think of this phase transition in terms of localization [44] and the localization length of the Floquet states. In the weak disorder regime $w < w_c$ where w_c is the critical disorder strength, the localization length is equal to the system size [1] which indicates that the Floquet states are extended. Above the critical value w_c, the localization length behaves as $\xi \sim (w - w_c)^{-2}$ [44]. In this regime, the localization length is finite therefore the Floquet states are localized.

5.2 Mapping to the 2D static system

We proceed our study on the Rice-Mele model and the effect of disorder by exploiting two diagnostic tools for topological phases, the local Chern marker and the strange correlation

[1] Thus, in the thermodynamic limit, the localization length diverges.

function. These two techniques are applied to static systems, hence we map our 1D dynamical Rice-Mele model to a static 2D one by using the Floquet-Shirley approach, as described in Section 3.3. We start from the clean Rice-Mele model, and then we introduce on-site disorder, in the same manner as we did in the previous section.

5.2.1 The clean Rice-Mele model

We exploit the Shirley-Floquet approach to map the dynamical 1D Rice-Mele system to an effective static 2D system. The Rice-Mele Hamiltonian is given in a compact form,

$$\hat{H}_{RM}(t) = \hat{H}(t) = -E_{J_1}(t)\hat{T}_1 - E_{J_2}(t)\hat{T}_2 + \mu_A(t)\hat{U}_A + \mu_B(t)\hat{U}_B \tag{5.2.1}$$

where $\hat{T}_1, \hat{T}_2$ are the intra-cell and inter-cell kinetic terms, respectively,

$$\hat{T}_1 = \sum_j \left(\hat{c}^\dagger_{2j-1}\hat{c}_{2j} + h.c.\right), \quad \hat{T}_2 = \sum_j \left(\hat{c}^\dagger_{2j}\hat{c}_{2j+1} + h.c.\right) \tag{5.2.2}$$

and $\hat{U}_A, \hat{U}_B$ are the sum of particle number operators for sublattice A and B, respectively,

$$\hat{U}_A = \sum_j \hat{c}^\dagger_{2j-1}\hat{c}_{2j-1}, \quad \hat{U}_B = \sum_j \hat{c}^\dagger_{2j}\hat{c}_{2j} \tag{5.2.3}$$

We recall the form of the time-dependent coefficients of the Hamiltonian, where we expand the sinusoidal functions into a sum of complex exponentials.

$$E_{J_{1/2}}(t) = E_{J_0} \pm \delta E \cos\omega t = E_{J_0} \pm \frac{\delta E}{2}\left(e^{i\omega t} + e^{-i\omega t}\right) \tag{5.2.4}$$

$$\mu_{A/B}(t) = \pm\Delta \sin\omega t = \pm\frac{\Delta}{2i}\left(e^{i\omega t} - e^{-i\omega t}\right) \tag{5.2.5}$$

We start by evaluating the Fourier coefficients of the Hamiltonian,

$$\hat{H}^{(\Delta m)} = \frac{1}{\tau}\int_0^\tau dt\ \hat{H}(t)e^{i\Delta m\,\omega t} \tag{5.2.6}$$

The $\Delta m = 0$ coefficient is the time-average Hamiltonian over a pumping cycle,

$$\hat{H}^{(0)} = -E_{J_0}\left(\hat{T}_1 + \hat{T}_2\right) \tag{5.2.7}$$

which expresses the fact that the Hamiltonian of each individual chain characterized by the frequency index m is consisted of hoppings between adjacent sites with unique hopping parameter E_{J_0}. Note that there is zero on-site staggered potential. Next, we have the $\Delta m = \pm 1$ coefficients,

$$\hat{H}^{(\pm 1)} = -\frac{\delta E}{2}\left(\hat{T}_1 - \hat{T}_2\right) \pm \frac{\Delta}{2}e^{i\frac{\pi}{2}}\left(\hat{U}_A - \hat{U}_B\right) \tag{5.2.8}$$

This Hamiltonian coefficient involves 'cross-talk' between different frequency indices with $|\Delta m| = 1$, otherwise it resembles the coupling of lattice sites on different m's. Remarkably, the on-site staggered potential of the original model has been cast into a complex hopping in this new picture, between sites of different frequency indices but same real space indices. This is translated into having some kind of a magnetic flux through the plaquettes. This can be understood when one follows a loop around a single plaquette, eventually picking up a phase corresponding to a flux of π (in units of the magnetic flux quantum) - see Figure 5.3a. Depending on the direction we choose to move on the loop, we also pick up an appropriate sign

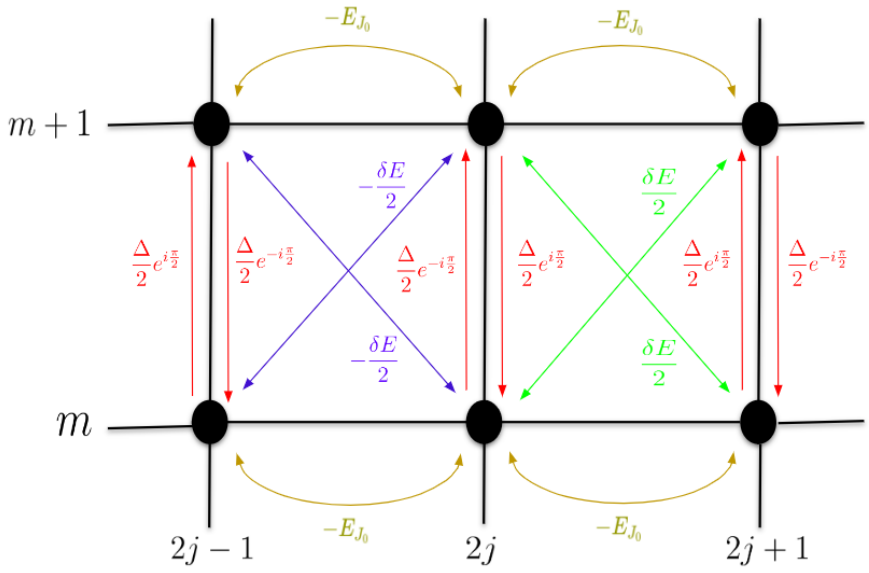

Figure 5.2: A sketch representing the processes described by Eq. 5.2.11.

on the phase/flux. Notice that when we choose a loop that goes around two plaquettes that involve a unit cell of the original model, then the overall flux is zero. This is a consequence of having zero magnetic field in the original problem (Figure 5.3c).

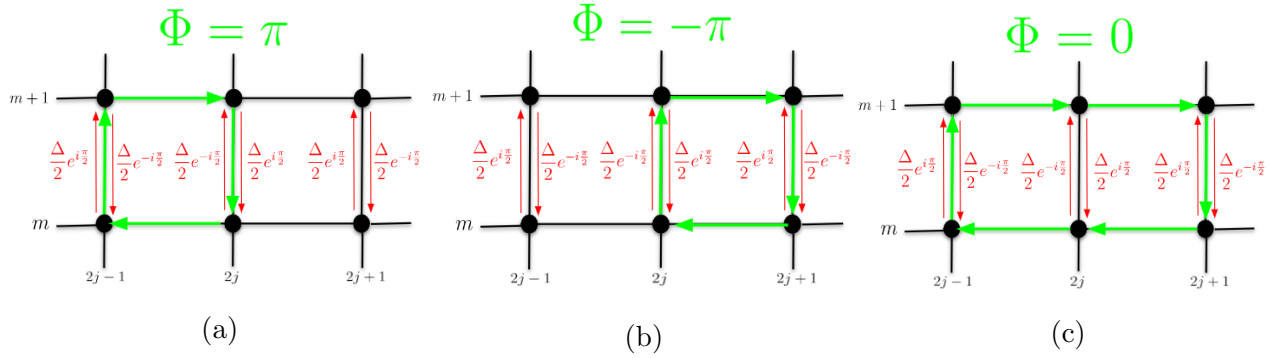

Figure 5.3: By considering a closed path around the plaquette, one can deduce the flux that penetrates it. The overall flux however between adjacent plaquettes in the horizontal direction (a unit cell in the x direction) is zero, and complies with the zero magnetic field in the original system.

The rest of the Fourier coefficients $|\Delta m| > 1$ are zero, because all integrals contain complex exponentials, which when integrated over a driving period, they are zero. The extended Hamiltonian has the following form, which is technically infinite in dimensions and each Hamiltonian coefficient is a matrix with dimension equal to that of the original Hilbert space.

$$\mathcal{H} = \begin{array}{c} \\ \mathbf{m} \\ \mathbf{m+1} \end{array} \begin{array}{c} \begin{array}{ccc} \mathbf{m} & & \mathbf{m+1} \end{array} \\ \begin{pmatrix} \ddots & H^{(-1)} & \\ H^{(+1)} & H_0 - m\omega & H^{(-1)} \\ & H^{(+1)} & H_0 - (m+1)\omega \quad H^{(-1)} \\ & & H^{(+1)} \quad \ddots \end{pmatrix} \end{array} \tag{5.2.9}$$

The driving frequency appears in the diagonal and acts as an electric field shifting the energy levels (see Figure 3.1). In the adiabatic regime, $\omega \to 0$, the contribution of the driving field is suppressed.

$$\mathcal{H}_{adiabatic} \approx \begin{array}{c} \\ \mathbf{m} \\ \mathbf{m+1} \\ \\ \end{array} \begin{array}{c} \begin{array}{cccc} \mathbf{m} & & \mathbf{m+1} & \end{array} \\ \begin{pmatrix} \ddots & H^{(-1)} & & \\ H^{(+1)} & H_0 & H^{(-1)} & \\ & H^{(+1)} & H_0 & H^{(-1)} \\ & & H^{(+1)} & \ddots \end{pmatrix} \end{array} \tag{5.2.10}$$

The frequency index m corresponds to the synthetic dimension, generated by Fourier transforming the original dynamical system to a static one. The mapping casts the dynamical dimension t into a synthetic, static one m. We can now write the effective Hamiltonian in terms of the creation and annihilation operators in the 2D picture,

$$\begin{aligned} \hat{H}_0^{eff} = &-\sum_{j,m} m\omega \left(\hat{c}^\dagger_{2j-1,m}\hat{c}_{2j-1,m} + \hat{c}^\dagger_{2j,m}\hat{c}_{2j,m} \right) - E_{J_0} \sum_{j,m} \left(\hat{c}^\dagger_{2j-1,m}\hat{c}_{2j,m} + \hat{c}^\dagger_{2j,m}\hat{c}_{2j+1,m} + h.c. \right) \\ &- \frac{\delta E}{2} \sum_{j,m} \left(\hat{c}^\dagger_{2j-1,m}\hat{c}_{2j,m+1} + \hat{c}^\dagger_{2j,m}\hat{c}_{2j-1,m+1} + h.c. \right) \\ &+ \frac{\delta E}{2} \sum_{j,m} \left(\hat{c}^\dagger_{2j,m}\hat{c}_{2j+1,m+1} + \hat{c}^\dagger_{2j,m+1}\hat{c}_{2j+1,m} + h.c. \right) \\ &+ \frac{\Delta}{2} \sum_{j,m} \left(e^{i\frac{\pi}{2}} \hat{c}^\dagger_{2j-1,m+1}\hat{c}_{2j-1,m} + e^{i\frac{\pi}{2}} \hat{c}^\dagger_{2j,m}\hat{c}_{2j,m+1} + h.c. \right) \end{aligned} \tag{5.2.11}$$

where the summation index j runs over the number of unit cells, and the index m runs, in principal, over the whole set of integers. In practice, one has to truncate at some value M (let us assume that we truncate symmetrically about $m = 0$) such that the summation index m runs from $-M$ to $+M$. In the adiabatic limit, $\omega \to 0$ and the truncation can be taken up to any arbitrary value of M.

5.2.2 Adding on-site static disorder

Given our previous analysis of the mapping to a static problem, let us introduce disorder to the original system and see how it acts in the new 2D picture. We consider a static, on-site disorder,

$$\hat{H}_{dis} = \sum_i \delta\mu_i \, \hat{c}^\dagger_i \hat{c}_i \tag{5.2.12}$$

where the summation index i runs over the number of sites $2N$ of the real lattice. The total hamiltonian is $\hat{H}(t) = \hat{H}_{RM}(t) + \hat{H}_{dis}$. This term is static in time, according to our analysis in the previous section, we expect it to appear only in the zeroth coefficient $H^{(0)}$,

$$\hat{H}^{(0)} = -E_{J_0}\left(\hat{T}_1 + \hat{T}_2\right) + \sum_i \delta\mu_i \, \hat{c}^\dagger_i \hat{c}_i \tag{5.2.13}$$

In the 2D picture, the original disordered Hamiltonian still represents the on-site disorder. Notice that the disorder is different across the real lattice as we chose in the beginning. However, for a fixed real lattice index and across the whole frequency space, the disorder is the same (it only depends on the real index i). The effective Hamiltonian for the disorder is,

$$\hat{H}_d^{eff} = \sum_{i,m} \delta\mu_i \, \hat{c}_{i,m}^\dagger \hat{c}_{i,m} \tag{5.2.14}$$

such that the total effective Hamiltonian in the case of disorder becomes $H^{eff} = H_0^{eff} + H_d^{eff}$ where H_0^{eff} is given by Eq. 5.2.11.

5.3 The Local Chern Marker

We now introduce the concept of the local Chern marker as a tool to investigate the topological phase of the Rice-Mele model in the 2D effective description.

5.3.1 Concept

The first Chern number defined on a two-dimensional Brillouin zone, is given by integrating the Berry curvature of an occupied band over the Brillouin zone. To be precise, for a system of N filled bands, the total Chern number will be the sum of Chern numbers of each of these bands.

$$\mathcal{C} = \frac{i}{2\pi} \sum_{n\in occ} \int_{BZ} dk_x dk_y \Big[\langle \partial_{k_x} u_{nk} | \partial_{k_y} u_{nk} \rangle - c.c. \Big] \tag{5.3.1}$$

where $|u_{n,\mathbf{k}}(\mathbf{r})\rangle$ is the periodic part of a Bloch function, normalized in a unit cell of area A_c. The Chern number given by Eq. 5.3.1 is a non-local quantity of the two-dimensional translational invariant system, in the thermodynamic limit. The expression for the Chern number is formulated in $\mathbf{k}$-space, which is inherently linked to periodic boundary conditions. A local 'version' of the Chern number is introduced in Ref. [51] or otherwise called the topological marker, and it is expressed in terms of the local ground-state projector $P(\mathbf{r}, \mathbf{r}')$, which decreases exponentially with the distance in an insulator. Thus, the local Chern marker (LCM), as we will refer to it from now on, samples the ground state locally.

It is shown in [51], that by exploiting properties of the ground state projector and its complement, along with some linear-response theory arguments, the Chern number can be written in terms of the ground-state projector P and the real-space operator $\mathbf{r}$, and it is a local quantity,

$$\mathcal{C} = \frac{4\pi}{A_c} \operatorname{Im} \operatorname{tr}_{cell}\{PxPy\} \tag{5.3.2}$$

and the trace is taken over the unit cell of the lattice-periodical system. Note that the position operator $\mathbf{r}$ is ill-defined in periodic boundary conditions, because it is multi-valued. Now, if we are given a finite system with open boundary conditions and replace the trace over the cell with the trace over the whole system, then we find the total Chern number,

$$\mathcal{C} = 4\pi \operatorname{Im} \operatorname{tr}\{PxPy\} = -2\pi i \operatorname{tr}\{[PxP, PyP]\} = 0 \tag{5.3.3}$$

by exploiting the trace property $\operatorname{tr}\{AB\} = \operatorname{tr}\{BA\}$ and the fact that the projection operator is idempotent $P^2 = P$. Arguably, the trace must be avoided when we deal with finite or disordered system. Consequently, we establish the local Chern marker in the following compact form,

$$\mathcal{C} = -2\pi i[PxP, PyP] \tag{5.3.4}$$

Projecting to the real-space basis $\mathbb{1} = \int d\mathbf{r}\,|\mathbf{r}\rangle\,\langle\mathbf{r}|$, we obtain

$$C(x,y) = -2\pi i \int d\mathbf{r}' \Big[\tilde{X}(\mathbf{r},\mathbf{r}')\tilde{Y}(\mathbf{r}',\mathbf{r}) - c.c.\Big], \quad \tilde{R}_i = \int d\mathbf{r}'' P(\mathbf{r},\mathbf{r}'') r_i'' P(\mathbf{r}'',\mathbf{r}') \tag{5.3.5}$$

where $P(\mathbf{r},\mathbf{r}') = \langle\mathbf{r}|R|\mathbf{r}'\rangle$ and $\tilde{R}_1 = \tilde{X}, \tilde{R}_2 = \tilde{Y}$. When space is discrete, the integration over space becomes a summation.

5.3.2 LCM of the static system

Initially, we consider the clean case of the Rice-Mele model with periodic boundary conditions. In such scenario, it is enough to simply calculate the Chern number by integrating the Berry curvature of occupied bands over the Brillouin zone and this is given by Eq. 5.3.1, due to space translation symmetry. The evaluation of the LCM requires a two-dimensional static system, hence we applied the Floquet-Shirley approach in Section 5.2.

The procedure to obtain the local Chern marker involves diagonalizing the truncated extended Hamiltonian of Eq. 5.2.9 in real space, and from there we construct the ground state projector $P(\mathbf{r},\mathbf{r}')$. We choose the truncation value such that the resulting 2D grid is approximately square. In Figure 5.4a, the local Chern marker for the clean system is displayed. The bulk of the system has a Chern number of -1 as was expected, while the left and right edges do not have a well-defined Chern number. This is because the system across the x-direction has periodic boundary conditions, while the definition of the LCM involves the position operator $\mathbf{r}$ which is ill-defined for these boundary conditions. In Figure 5.4b, the average Chern marker over the frequency index m is shown as a function of the real space index n, which clearly demonstrates the well-defined Chern number for the bulk, in contrast to the edges.

We also look into a case in which the system is in the trivial phase. Figure 5.5a shows that the bulk is characterized by a zero Chern number, hence there is zero transport. The trivial state is obtained by adding a perturbation to the Josephson energy E_{J_1}, as in Eq. 4.2.5. Let us look into another interesting case, that of the Rice-Mele model in the topological phase with open boundary conditions. As we have discussed in Chapter 4, the current is not quantized, even though the system is in a topological phase. This is evident by the local Chern marker depicted in Figure 5.6. The bulk is characterized by a Chern number of -1, as we expected for a system being in a topological phase.

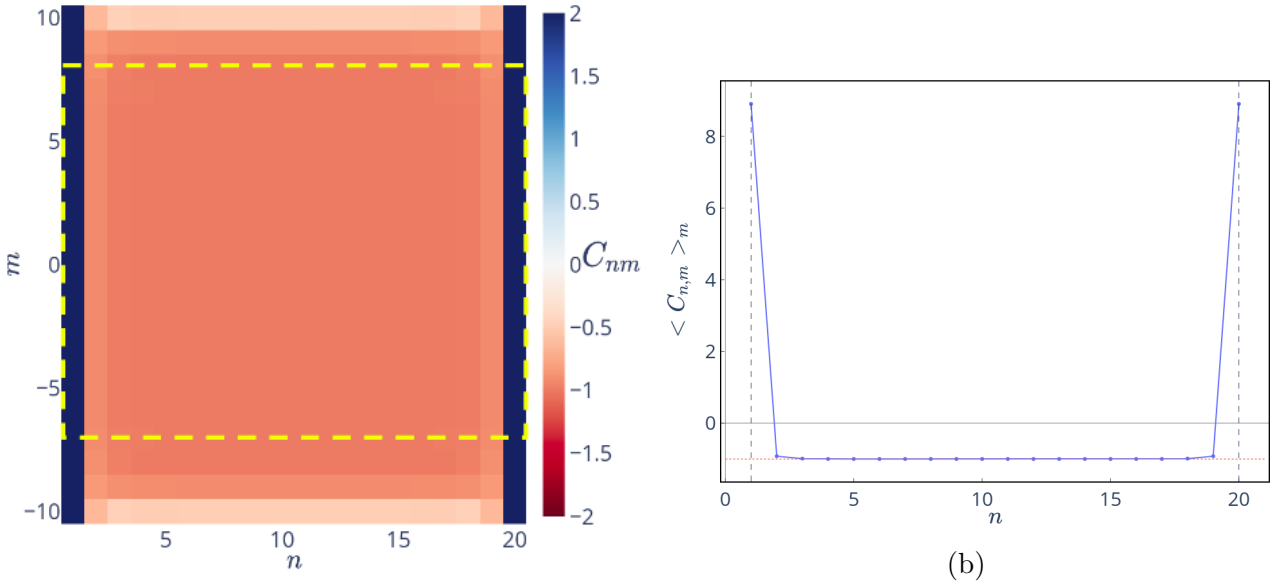

(a) (b)

Figure 5.4: (a) The local Chern marker for a topological state of the 2D static Rice-Mele model. (b) The frequency-averaged local Chern marker as a function of the real space index. The average over the frequency is taken within the yellow box. We note that the upper limit of the LCM colorbar is truncated to give equal emphasis to positive and negative values. Parameters: $\delta E = E_{J_0}, \Delta = 3E_{J_0}, \omega = 0.05E_{J_0}, L = 20$

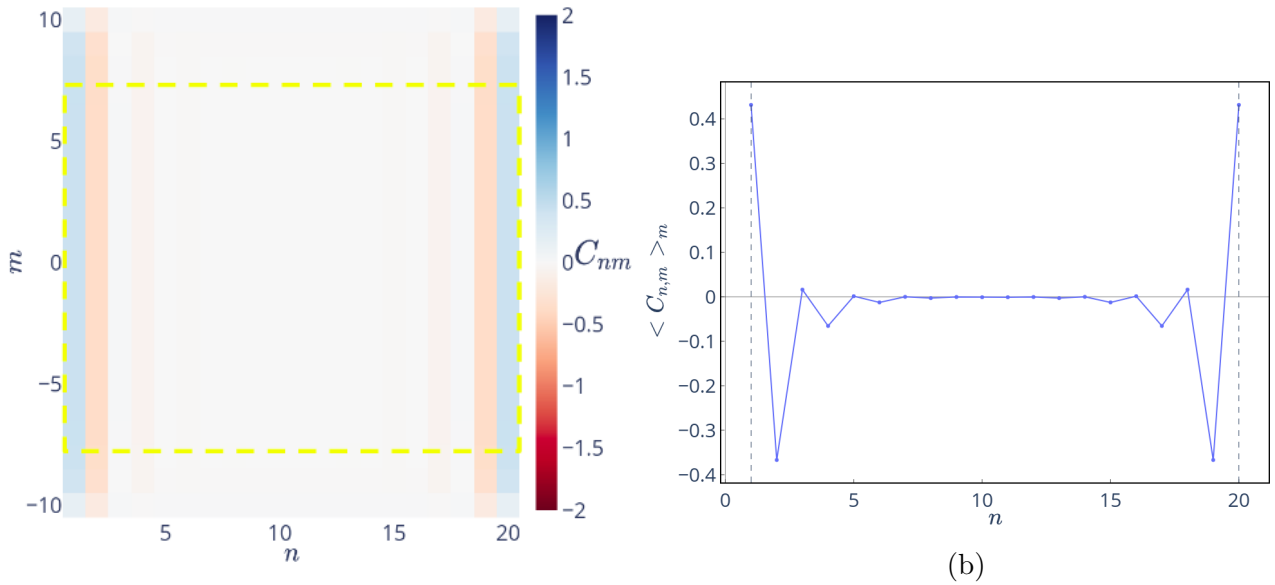

(a) (b)

Figure 5.5: (a) The local Chern marker for a trivial state of the 2D static Rice-Mele model. (b) The frequency-averaged (yellow box) local Chern marker as a function of the real space index n. The Chern marker vanishes in the bulk. Parameters: $\delta E = E_{J_0}, \Delta = 3E_{J_0}, \omega = 0.05E_{J_0}, L = 20, A = 6E_{J_0}$

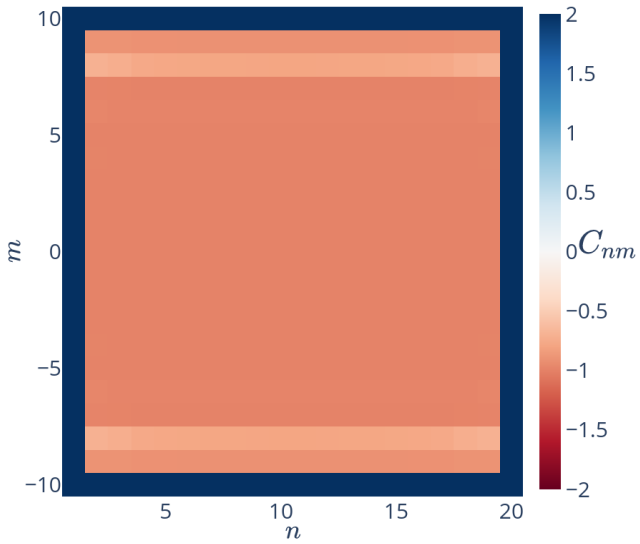

Figure 5.6: The local Chern marker for a topological state of the 2D static Rice-Mele model with open boundary conditions. We note that the upper limit of the LCM colorbar is truncated to give equal emphasis (in color) to positive and negative values. Parameters: $\delta E = E_{J_0}, \Delta = 3E_{J_0}, \omega = 0.05E_{J_0}, L = 20$

We now explore the Rice-Mele model with on-site disorder in the form of Eq. 5.2.12. In the presence of random disorder, the local Chern marker is averaged over a number of disorder configurations. In Figure 5.7a, the bulk averaged Chern marker is displayed as a function of the disorder strength. Clearly, for moderate disorder $w \sim 2.5E_{J_0}$, the Chern marker displays remarkable robustness, as witnessed in the previous subsection. For this range of the disorder strength, the energy gap remains open. However, as adiabaticity breaks down and the gap approaches the zero value at $w \approx 2.5E_{J_0}$, the Chern marker 'moves' away from the value of -1. As the disorder strength increases, the average Chern marker vanishes.

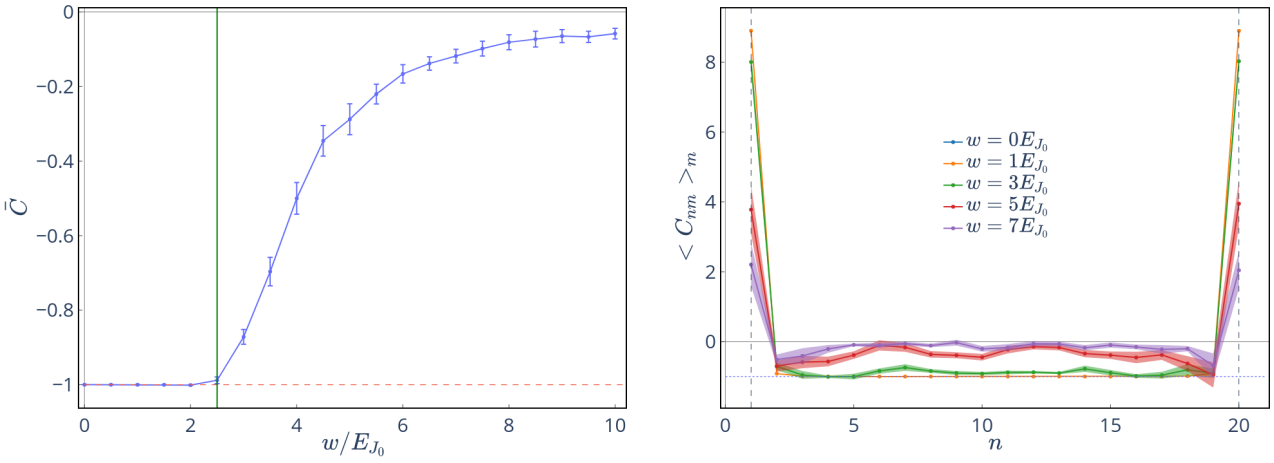

(a) (b)

Figure 5.7: The local Chern marker of the Rice-Mele model in the presence of disorder. (a) The bulk-averaged local Chern marker as a function of disorder. (b) The frequency-averaged local Chern marker as a function of the real space index n. As the disorder strength increases, we transition from a topological state to a trivial one. Parameters: $\delta E = E_{J_0}, \Delta = 3E_{J_0}, \omega = 0.05E_{J_0}, L = 20, N_{config} = 20$

In Figure Eq. 5.7b, the average Chern marker over the frequency index m is shown along the real space dimension for various disorder strengths. Evidently, the Chern marker becomes zero in the bulk as the disorder increases.

It is worth mentioning that the Chern marker at the boundaries of the two-dimensional grid are determined such that the trace of the local Chern marker over the whole sample is zero.

5.4 The strange correlation function

5.4.1 The concept of the strange correlator

In many realistic scenarios, identifying the topological character of a state of some given system can be tricky. This is the case with finite-size systems and disorder, effects that can prevent us from precisely characterizing the phase of the system. The concept of the strange correlation function [52, 53] is introduced here, as a mean to characterize phases in such tricky scenarios. A detailed analysis of the strange correlator [2] is beyond the scope of this thesis because it requires concepts from Conformal Field theory, however we present some key components of the theory and how it can be utilized as a diagnostic tool for topological phases.

The strange correlation function is given by,

$$s[\hat{o}, \hat{o}']_{\mathbf{r},\mathbf{r}'} = \frac{\langle\Omega|o(\mathbf{r})o'(\mathbf{r}')|\Psi\rangle}{\langle\Omega|\Psi\rangle} \tag{5.4.1}$$

It may look like a typical two-point correlation function, yet it is not, hence the name 'strange'. It requires two different states to evaluate this object; $|\Omega\rangle$ is the reference state, and typically corresponds to a topologically trivial state, and $|\Psi\rangle$ is the target state, or in other words the state we want to characterize, either being topological or not. In order for this to be valid, the two states must be defined in the same Hilbert space. The operators $o(\mathbf{r}), o'(\mathbf{r}')$ are chosen according to the symmetries of the system. For instance, the Hamiltonian of the Rice-Mele model commutes with the particle number operator, $\left[\hat{H}_{RM}, \hat{N}\right] = 0$, therefore the particle number is a symmetry of the system. Thus a suitable choice for the operators in the strange correlator are $\hat{o} = \hat{c}^\dagger$ and $\hat{o}' = \hat{c}$, since $\hat{N} = \hat{c}^\dagger\hat{c}$. This correlation function is defined in the bulk of the system, and as a result it does not rely on the presence of physical boundaries.

Consider a lattice of dimension d and size L. We calculate the sum of the strange correlation function of Eq. 5.4.1,

$$\bar{s}[\hat{o}, \hat{o}']_L = \frac{1}{L^d}\sum_{\mathbf{r},\mathbf{r}'} |s[\hat{o}, \hat{o}']_{\mathbf{r},\mathbf{r}'}| \tag{5.4.2}$$

which tells us how the strange correlator scales with the system size. This information is obtained once we determine how Eq. 5.4.1 behaves in space. When the target state is a short-ranged entangled topological phase, and the reference state is a trivial state, then the strange correlator decays as a power law in large distances,

[2] It is similar to the off-diagonal long range order (ODLRO) we encounter in the Bose-Einstein condensates (and BCS superconductivity), in which the one-body density matrix is expressed to be a two-point correlation function that decays to a constant in the long distance limit.

$$|s[\hat{o},\hat{o}']_{\mathbf{r},\mathbf{r}'}| \propto |\mathbf{r}-\mathbf{r}'|^{-2\alpha}, \quad |\mathbf{r}-\mathbf{r}'| \to \infty \tag{5.4.3}$$

Then the scaling of Eq. 5.4.2 is resolved as follows,

$$\bar{s}[\hat{o},\hat{o}']_L \sim \begin{cases} L^{d-2\alpha} & \alpha < d/2 \\ \ln L & \alpha = d/2 \\ \text{const} + \mathcal{O}(r^{d-2\alpha}) & \alpha > d/2 \end{cases} \tag{5.4.4}$$

where α is the scaling dimension of the boundary in the space-time rotation picture. In Conformal field theory, we can prepare a setup in which the phase represented by $|\Omega\rangle$ precedes the topological phase $|\Psi\rangle$ in time, and hence they are separated by a boundary in time. Through a space-time rotation, the time direction becomes spatial and the boundary is described by the non-interacting, gapless Dirac theory [52]. The Dirac mode has a scaling dimension $\alpha = (d-1)/2$. For both one-dimensional and two-dimensional, we get $\alpha < d/2$, thus from Eq. 5.4.4, the scaling of the strange correlation follows a linear trend, i.e. $\bar{s}[\hat{o},\hat{o}']_L \sim L$.

If $|\Psi\rangle$ is trivial, or belongs to the same phase as the reference state, then the strange correlator $s[\hat{o},\hat{o}']_{\mathbf{r},\mathbf{r}'}$ decays exponentially for large distances. Therefore the sum $\bar{s}[\hat{o},\hat{o}']_L$ converges exponentially to a constant.

5.4.2 Characterization of topological phases in the RM model

We consider the 2D static Rice-Mele model with periodic boundary conditions, with the goal to characterize certain states. To facilitate this, we must initially establish the trivial state that will serve as our reference state. We recall from our analysis in Chapter 4, that a trivial state for the Rice-Mele model is obtained when an energy shift $A > 2\delta E$ is introduced to one of the hopping parameters. That will be the trivial state.

We denote a state of the 2D static Rice-Mele model as $|\psi(A)\rangle$ where A is the parameter that denotes whether the state is topological or not.

$$|\Omega\rangle = |\psi(A_1)\rangle\,, \quad |\Psi\rangle = |\psi(A_2)\rangle \tag{5.4.5}$$

such that the strange correlator is given by

$$(\bar{S}_L)_{ss'} = \frac{1}{L(L+1)} \sum_{j,m,j',m'} s_{s,j,m,s',j',m'}, \quad s_{s,j,m,s',j',m'} = \frac{\langle\psi(A_1)|c^\dagger_{s,j,m}c_{s',j,m}|\psi(A_2)\rangle}{\langle\psi(A_1)|\psi(A_2)\rangle} \tag{5.4.6}$$

where the operators $c^\dagger_{s,j,m}, c_{s,j,m}$ are the creation and annihilation operators of the 2D static system, and s, j, m are the sublattice, unit cell and frequency indices respectively. The state $|\psi(A)\rangle$ is obtained by diagonalizing the truncated extended Hamiltonian.

We should note here that since the definition of the strange correlation function of Eq. 5.4.2 assumes a square lattice, our truncation of the frequency direction in the mapping from 1+1D to 2+0D through the Floquet-Shirley approach is chosen such that it agrees with the size of real space lattice L. The truncation is performed symmetrically about $m = 0$ such that $m \in \{-M, -M+1, ..., 0, ..., M-1, M\}$, therefore the truncated size of the frequency direction is $2M+1$ where $M = L/2 = N$. For large L, the lattice is effectively a 2D square one. The strange correlator will be a function of 6 indices $s_{s,j,m,s',j',m'}$ where s, s' are the sublattice indices, j, j' correspond to the unit cell indices and m, m' correspond to the frequency direction.

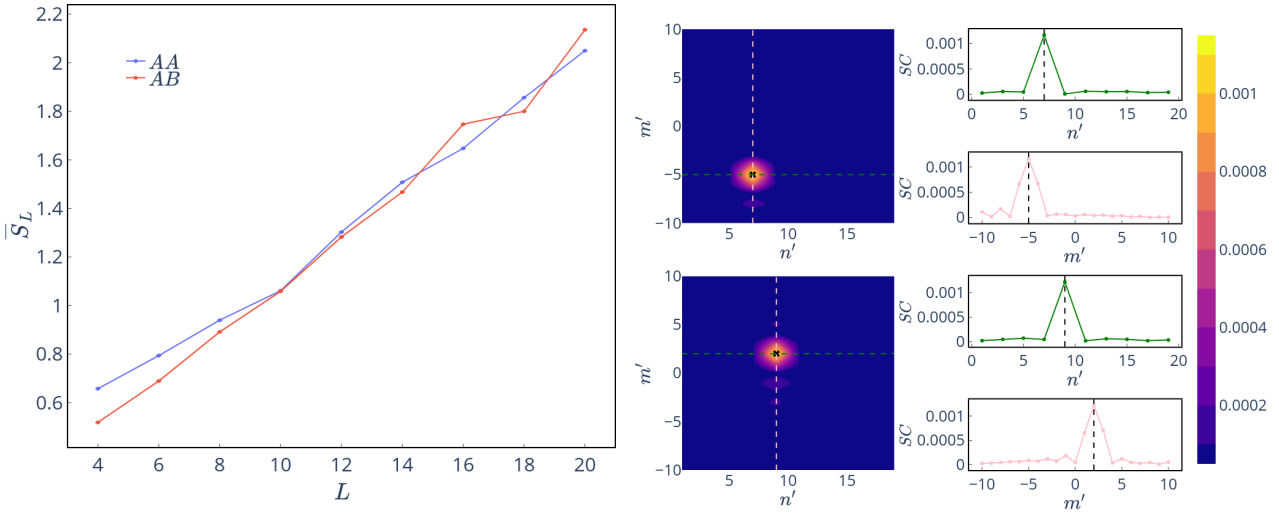

(a) (b)

Figure 5.8: (a) The scaling of the strange correlator with the system size for a trivial $A_1 = 6E_{J_0}$ and trivial $A_2 = 0$ states. (b) The strange correlator in space $s_{s,j,m,s',j',m'}$ for fixed (j, m) (denoted by the black cross) and $(s, s') = (A, A)$. The horizontal and vertical cuts show the correlation (SC) along that direction. Note, here n is the real space index and express (s, j). Parameters: $\delta E = E_{J_0}, \Delta = 5E_{J_0}, \omega = 0.01E_{J_0}, A_1 = 6E_{J_0}, A_2 = 0$

From the results in the previous subsection, and since we consider the two-dimensional static Rice-Mele model, we expect the strange correlator to scale linearly with the system size for a topological target state, given that the reference state is trivial. In the forthcoming analysis, it is important to clarify that the system size refers specifically to the size of the square lattice. In our case, the system size is determined by the size of the real lattice, denoted as $L = 2N$. This size also corresponds to the size of the frequency direction, except for the one in $2M + 1 = L + 1$, that becomes irrelevant for large L, such that $L(L + 1) \approx L^2$.

We take our reference state to be $|\psi(A_1 = 6E_{J_0})\rangle$, and we wish to examine the scaling of the strange correlation function with the system size for the target state $|\psi(A_2 = 0)\rangle$. Figure 5.8a demonstrates that the strange correlator exhibits linear scaling with the system size for $A_2 = 0$, implying that the target state is indeed a topological state. This behavior can be attributed to the smooth behavior of the strange correlator $s_{s,j,m,s',j',m'}$, as depicted in Figure 5.8b. The decay of the strange correlator in space follows a power-law at large distances, Eq. 5.4.3 [3]. We extend our analysis to include cases where the states involved in the strange correlator are in the same phase. As an example, we consider both the reference and the target state to be topological states of the Rice-Mele model with different energy shifts in the hopping parameter, $A_1 \neq A_2$ - see Figure 5.9a. Another possibility is both the reference and target states to be topologically trivial states with $A_1 \neq A_2$ (Figure 5.9b). In both occasions, the strange correlator approaches a constant value as the system size increases, which confirms that the states inolved in the strange correlator belong to the same phase.

[3]Due to the finite size of the system, it becomes challenging to observe the power-law decay, even when using log-log plots.

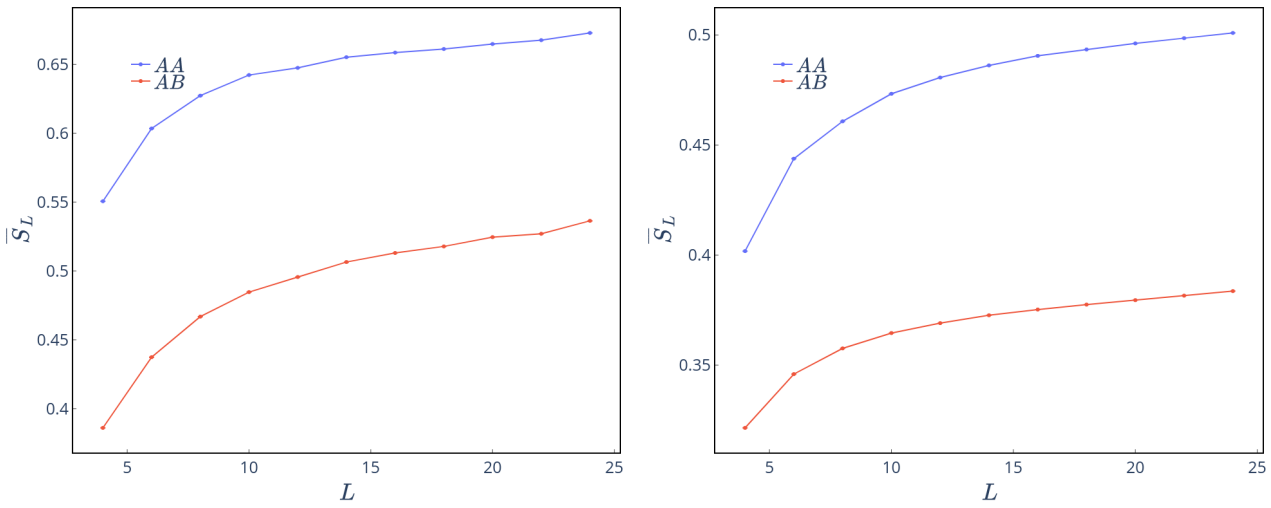

(a) (b)

Figure 5.9: The scaling of the strange correlation function with the system size for (a) a set of topological states $A_1 = 0.5E_{J_0}, A_2 = 0$ and for a set of trivial states (b) $A_1 = 6E_{J_0}, A_2 = 5E_{J_0}$. Parameters: $\delta E = E_{J_0}, \Delta = 5E_{J_0}, \omega = 0.01E_{J_0}, N_{config} = 20$.

5.4.3 Disorder and the breakdown of the strange correlation at strong disorder

We now introduce static disorder to the Rice-Mele model. The mapping to the static system does not alter the nature of the disorder, as it continues to resemble on-site disorder in the new description, as shown in Subsection 5.2.2. From Section 5.1, it was found that the presence of disorder in the system causes a decrease of the excitation gap. While it remains open, the pumped charge is quantized. As disorder becomes stronger and the gap closes, the quantization ceases to exist, and the system is in a topologically trivial, insulating phase, and as a result the current vanishes.

We use the strange correlation function to study these disordered states of the Rice-Mele model, which are averaged over a number of disorder configurations. The reference state of the correlator is a trivial state with $A_1 = 6E_{J_0}$, while the target state corresponds to $A_2 = 0$ which is a topological state in the clean case. For the purpose of comparison, the parameters of the topological state are the same as those discussed in Section 5.1. Figure 5.10a demonstrates the linear scaling of the correlator with the system size for a few values of disorder strength. Evidently, these states are topological, hence the system is in a topological state in the presence of disorder and the pumped charge is quantized. Nevertheless, as the disorder is progressively increased, we expect that the excitation gap will eventually close. We observe that the strange correlation function breaks down in strong disorder. This is evident in both Figures 5.10b and 5.10c, in which the strange correlator admits large values as the system size increases. We note that this issue is not addressed in the literature.

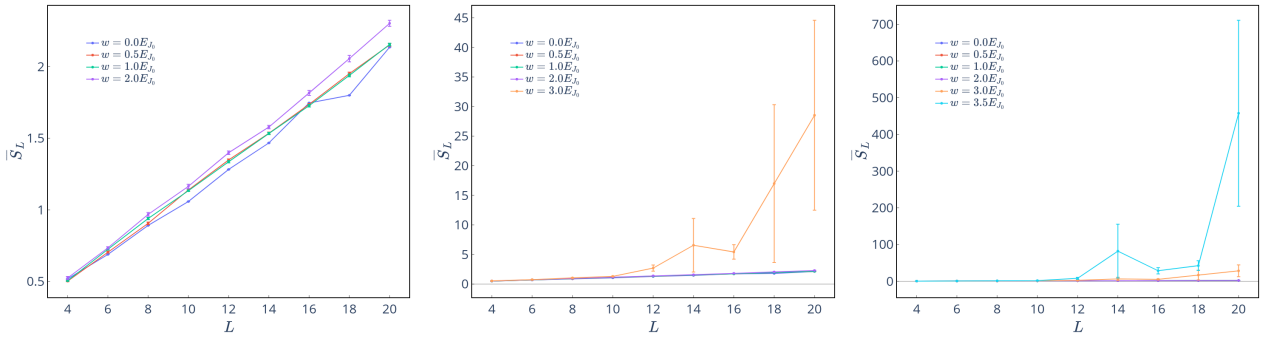

(a) (b) (c)

Figure 5.10: The scaling of the strange correlator $(S_L)_{AB}$ with the system size in the presence of disorder. For weak disorder, (a) the correlator scales linearly and thus the target state is in the topological phase. As the disorder strength gets large, the correlator breaks down as shown in (b) and (c). Parameters: $\delta E = E_{J_0}, \Delta = 5E_{J_0}, \omega = 0.01E_{J_0}, N_{config} = 20, A_1 = 6E_{J_0}, A_2 = 0$.

To better understand this behavior, we examine the distribution of values of the strange correlator across multiple realizations of disorder. Figure 5.11a shows a typical linear scaling of the strange correlator for a topological target state with disorder. The box distribution illustrates the range within which the calculated values of the strange correlator extend. Instead, Figure 5.11b shows an example of the strange correlator collapsing in strong disorder. At large L, the values of the correlator exhibit a wide range of spread. The wide spread and presence of outliers in the box distribution suggest that the behavior of the calculated correlator is unpredictable across different disorder configurations.

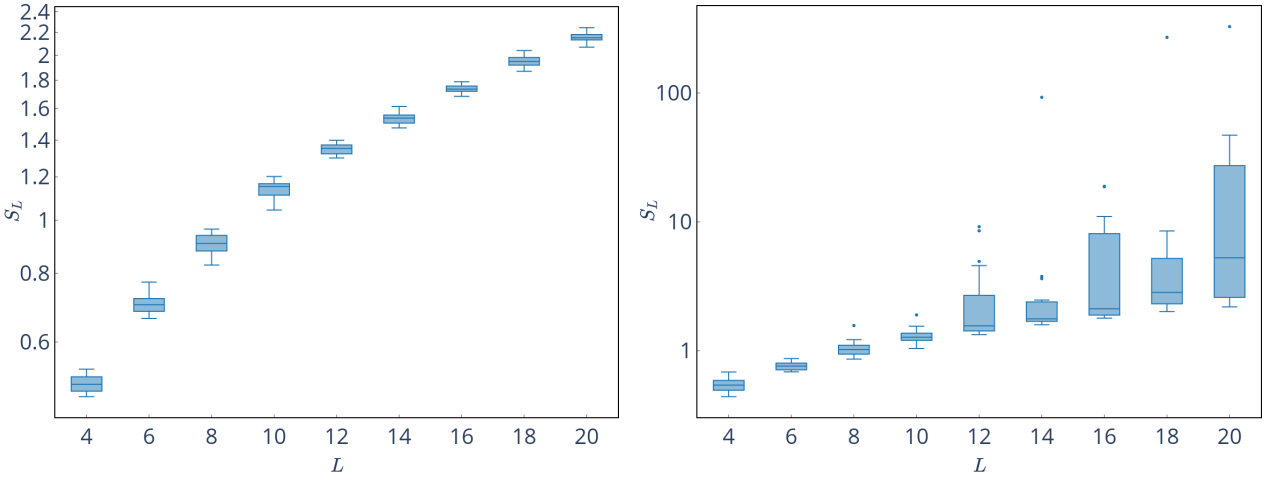

(a) (b)

Figure 5.11: Box plots of the calculated values of the strange correlator for a number of disorder configurations for (a) a regular linear scaling and a (b) irregular scaling of the correlator with the system size. In (b), the values are spread over a wide range, indicating the collapse of the correlator. Parameters: $\delta E = E_{J_0}, \Delta = 5E_{J_0}, \omega = 0.01E_{J_0}, N_{config} = 20, A_1 = 6E_{J_0}, A_2 = 0, (s, s') = (A, B)$.

To further support our argument, we look at the medians of the set of correlator values, calculated for a number of disorder configurations. We do this by examining the denominator, the numerator of the strange correlator and the correlator itself S_L separately,

$$(S_L^{(numerator)})_{s,s'} = \sum_{\mathbf{r},\mathbf{r}'} \langle\Omega|o_s(\mathbf{r})o'_{s'}(\mathbf{r}')|\Psi\rangle\,, \quad (S_L^{(denominator)})_{s,s'} = L(L+1)\,\langle\Omega|\Psi\rangle \tag{5.4.7}$$

First, from Figure 5.12, it is evident that the breakdown due to strong disorder becomes increasingly pronounced as the system size increases. Looking at the median values of the correlator distributions, it appears that the large values in the strange correlator are primarily attributed to the decreasing denominator. We further examine the behavior of the correlator in space $s_{s,j,m,s',j',m'}$. Figure 5.13 shows the correlation function for a given (n, m) where $n = (s, j)$, for a strong disorder configuration. We understand that the strange correlator indeed breaks down completely since it behaves in a very irregular way, compared to Figure 5.8b.

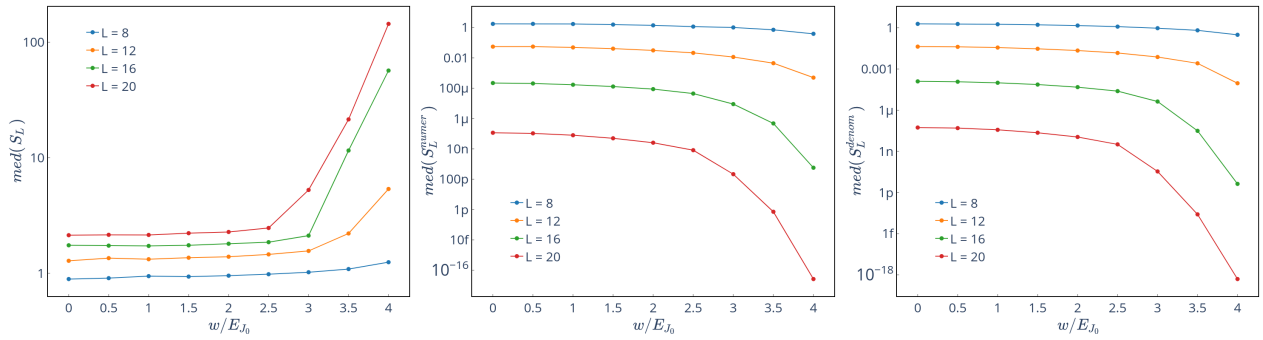

(a) (b) (c)

Figure 5.12: The median of the distributions of values for the (a) strange correlator, (b) the numerator and (c) the denominator of the strange correlator, as a function of disorder. Parameters: $\delta E = E_{J_0}, \Delta = 5E_{J_0}, \omega = 0.01E_{J_0}, N_{config} = 20, A_1 = 6E_{J_0}, A_2 = 0, (s, s') = (A, B)$.

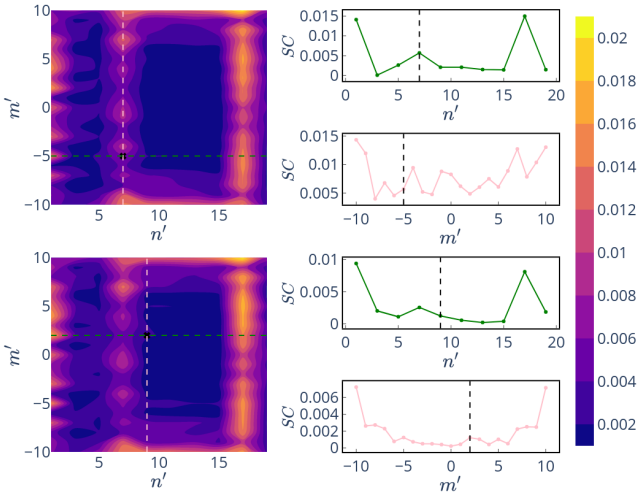

Figure 5.13: The strange correlator $s_{s,j,m,s',j',m'}$ for fixed (s, j, m, s') (denoted by the black cross) for a strong disorder configuration Note, here n is the real space index and express (s, j). $\delta E = E_{J_0}, \Delta = 5E_{J_0}, w = 4E_{J_0}, \omega = 0.01E_{J_0}, N_{config} = 20, A_1 = 6E_{J_0}, A_2 = 0, (s, s') = (A, B), L = 20$

In summary, the behavior of the strange correlation function under strong disorder in the Rice-Mele model requires further investigation to comprehend the reasons behind its collapse.

Additionally, the observed collapse of the strange correlator in the presence of disorder, as demonstrated in Appendix A for the 1D SSH model, emphasizes the need of studying this behavior, which appears to be prevalent in systems with strong disorder.

Chapter 6

Pumping with external leads

So far, we have considered a scenario in which the JJA Hamiltonian reduces to the Rice-Mele model which we have extensively studied throughout the last two chapters. However, we take a step back, and consider the Josephson junctions array setup of Chapter 2, with open boundary conditions. The system is connected to external superconducting leads at the boundaries [50]. Our target in this work is to demonstrate whether we can still observe induced quantized transport in the array, and examine its robustness.

6.1 Modeling of the leads

We consider a one dimensional Josephson junctions array in which only Cooper pairs take part in the dynamics. We connect two superconducting leads at the boundaries of the array, as depicted in Figure 6.1. Cooper pairs are allowed to tunnel between the leads and the system, through an ordinary Josephson junction,

$$\hat{H}_b(t) = -E_J^\ell(t)\cos(\hat{\varphi}_L - \hat{\varphi}_1) - E_J^\ell(t)\cos(\hat{\varphi}_{2N} - \hat{\varphi}_R) \tag{6.1.1}$$

where $\hat{\varphi}_L, \hat{\varphi}_R$ are the superconducting phase operators of the left and right lead respectively, and $\hat{\varphi}_1, \hat{\varphi}_{2N}$ the phase operators of the first and last island of the chain. The parameter $E_J^\ell(t)$ is the Josephson energy of the junctions of the system with the leads, and generally it is time-dependent. The total Hamiltonian of the system is,

$$\hat{H}_{tot}(t) = \hat{H}_0(t) + \hat{H}_b(t) \tag{6.1.2}$$

where $\hat{H}_0(t)$ is the JJA Hamiltonian of the array. We apply the hardcore boson approximation that we developed in Chapter 2 to the Hamiltonian given by Eq. 6.1.2. First the boundary term becomes,

$$\hat{H}_b(t) = -E_J^\ell(t)\left(e^{-i\hat{\varphi}_L}\hat{a}_1 + h.c.\right) - E_J^\ell(t)\left(e^{-i\hat{\varphi}_R}\hat{a}_{2N} + h.c.\right) \tag{6.1.3}$$

where $\hat{a}_{1/2N}$ are the hardcore bosonic annihilation operators of the first and last island in the array. The operators $e^{-i\hat{\varphi}_{L/R}}$ are the Cooper pair creation operators of the left and right leads. The JJA Hamiltonian $\hat{H}_0(t)$ reduces to the hardcore boson version of it, and by applying the appropriate driving protocol, it becomes the Rice-Mele Hamiltonian of Eq. 2.4.8, with open boundary conditions. Consequently, the total Hamiltonian is expressed in terms of the hardcore bosonic operators for the system, and the Cooper pair operators for the leads. We will now show why including superconducting leads is preferred rather than ordinary normal leads.

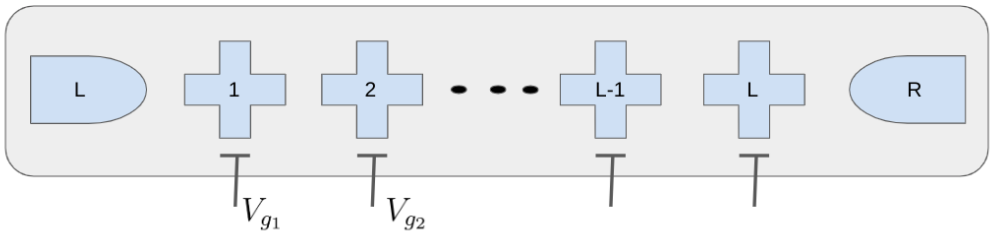

Figure 6.1: A sketch of the Josephson junctions array, connected to external superconducting leads.

Since the temperature is much lower than the critical BCS temperature, the leads are described by the BCS coherent state, characterized by a well-defined phase and a macroscopic particle number. Because of that, the state of the overall system is a product state of the Josephson junctions array state and the coherent state of the leads,

$$|\Psi_{tot}(t)\rangle = |BCS\rangle_L \otimes |\psi_{sys}(t)\rangle \otimes |BCS\rangle_R , \quad \forall t \geq 0 \tag{6.1.4}$$

and is a solution to the time-dependent Schrödinger equation

$$i\frac{\mathrm{d}}{\mathrm{d}t}|\Psi_{tot}(t)\rangle = \hat{H}_{tot}(t)\,|\Psi_{tot}(t)\rangle \tag{6.1.5}$$

with $\hat{H}_{tot}(t)$ being the total Hamiltonian in the hardcore boson limit. The BCS coherent state is an eigenstate of the operators $e^{-i\hat{\varphi}_{L/R}}$ which appear in the overall Hamiltonian, with eigenvalue the superconducting phase,

$$e^{-i\hat{\varphi}_{L/R}}\,|BCS\rangle_{L/R} = e^{-i\phi_{L/R}}\,|BCS\rangle_{L/R} \tag{6.1.6}$$

Because of this nice property of the BCS superconductor, the Schrödinger equation of Eq. 6.1.5 reduces to,

$$i\frac{\mathrm{d}}{\mathrm{d}t}|\psi_{sys}(t)\rangle = \hat{H}(t)\,|\psi_{sys}(t)\rangle \tag{6.1.7}$$

where the Hamiltonian $\hat{H}(t)$ describes the Josephson junctions array,

$$\hat{H}(t) = \hat{H}_{RM}(t) - E_J^{\ell}(t)\,\left(e^{-i\phi_L}\hat{a}_1 + h.c.\right) - E_J^{\ell}(t)\,\left(e^{-i\phi_R}\hat{a}_{2N} + h.c.\right) \tag{6.1.8}$$

The effect of the boundary, the tunneling between the array and the leads, appears in the form of the superconducting phases of the two leads. The dynamics of the overall system remains coherent, and unitarity is preserved. Thus, we can still solve the Schrödinger equation, or equivalently the von Neumann equation, to study the dynamics of the system.

Notice however that the Hamiltonian does not commute with the particle number. The introduction of the boundary term breaks this symmetry because the Hamiltonian is not quadratic anymore . Thus we have to work in the full Hilbert space to study the dynamics, and this requires a many-body treatment. This makes our work challenging since we cannot explore systems of arbitrary size, because of the exponential scaling of the Hilbert space with the system size.

The breaking of the particle number symmetry has implications on the many-body spectrum. The degeneracy that appears originally appears due to particle number symmetry and the zero-energy edge modes is lifted by the boundary term. We will examine this effect later in this chapter.

As discussed in Chapter 2, the hardcore bosonic Hamiltonian is tricky to handle, especially if we attempt to diagonalize it by some unitary transformation in a single particle basis. Recall that hardcore bosons are actually strongly interacting bosons with a mixed particle algebra. There, we exploited the Jordan-Wigner transformation which allowed us to map from hardcore bosons to free fermions and we carry out our study in that description. In the case of Eq. 6.1.8 though we cannot apply this transformation. The resulting Hamiltonian becomes non-local because the Jordan-Wigner string operator appears in the boundary term. We want to avoid this complication, and therefore we preserve the hardcore bosonic description.

Equivalently, we re-write the Hamiltonian of Eq. 6.1.8 in terms of spins, since the hardcore bosonic operator obey a similar algebra to spin-1/2 operators,

$$\begin{aligned}\hat{H}(t) = &-E_{J_1}(t)\sum_j \left(\sigma^-_{2j-1}\sigma^+_{2j} + h.c.\right) - E_{J_2}(t)\sum_j \left(\sigma^-_{2j}\sigma^+_{2j+1} + h.c.\right) \\ &+ \sum_j \mu_A(t)\,\frac{1-\sigma^z_{2j-1}}{2} + \sum_j \mu_B(t)\,\frac{1-\sigma^z_{2j}}{2} \\ &- E^\ell_J(t)(e^{-i\phi_L}\sigma^+_1 + h.c.) - E^\ell_J(t)(e^{-i\phi_R}\sigma^+_{2N} + h.c.)\end{aligned} \tag{6.1.9}$$

where we have identified $a^\dagger_j \leftrightarrow \sigma^-_j$, $a_j \leftrightarrow \sigma^+_j$, $a^\dagger_j a_j \leftrightarrow \frac{1-\sigma^z_j}{2}$ and the basis $|0\rangle \leftrightarrow |\uparrow\rangle, |1\rangle \leftrightarrow |\downarrow\rangle$. In the spin description, the boundary term is mapped to a transverse field, and the magnetization is not conserved. However, this approach still constrains us to work in the full Hilbert space.

Another important feature of the approach presented in this section is that since the Hamiltonian is an observable quantity, it is gauge invariant, and it depends only on the phase difference of the superconducting leads, i.e. $\phi = \phi_L - \phi_R$. The Hamiltonian is now parametrized by $\hat{H}(\phi)$. This parameter ϕ appears as a magnetic flux in the system. By applying a gauge transformation, we can distribute the phase to the tunneling terms, casting the hopping parameters into complex numbers. This resembles the appearance of a magnetic flux. We can think of the system as a ring with twisted boundary conditions $c_{i+L} = e^{i\phi}c_i$, the generalization of periodic boundary conditions. In such case, the Hamiltonian is parametrized by ϕ, and ϕ plays the role of a supercell pseudomomentum [1], where the supercell is the whole system [54]. A consequence of the dependence of the Hamiltonian on ϕ is that the bulk properties for instance correlation functions and expectation values will depend on ϕ. In the case of gapped, local Hamiltonians with exponentially localized ground state projectors, the expectation values of the system do not depend on ϕ in the limit of large system size [2] [54]. We will test this argument in our case later on.

The appearance of ϕ in the Hamiltonian will play a crucial role in transport. In the original Rice-Mele model, the pumped charge is expressed in terms of the first Chern number, defined on the parameter space formed by (k, t). In the present case, k is no longer a good quantum number. Merely having periodicity in time is insufficient to observe the effects associated with non-trivial topology. The role of ϕ becomes apparent here. As a parameter, ϕ is indeed periodic since $\phi \in S^1$. Notice though that different values of ϕ correspond to a set of different Hamiltonians $\{H(\phi)\}$. A many-body topological invariant in this occasion will require the integration over $\phi \in S^1$ [25].

[1] We can think of ϕ as the many-body generalization of the single-particle momentum [54, 25].

[2] In the case of correlation functions, if the equal-time correlation functions decay exponentially, then the correlation functions will not depend on the phase ϕ for large system sizes.

6.2 The many-body gap

As emphasized consistently throughout this thesis, the gap along with the driving frequncy are the relevant energy scales one looks at when considering adiabaticity. In this scenario, the gap corresponds to the instantaneous many-body gap. Typically, we prepare the system in the ground state. Then, the many-body gap will be the energy difference between the instantaneous ground state and the first excited state. In the time-periodic Rice-Mele model, the gap corresponds to the minimum gap,

$$E_g = \min_{0\leq t\leq \tau} \left[E_1(t) - E_0(t)\right] \tag{6.2.1}$$

where $E_{0/1}(t)$ are the instantaneous many-body energies of the ground state and first excited state, respectively. As in the case with Rice-Mele in Chapter 4, the minimum gap is expected to found at $t = \tau/2$. At this time instance, the system adopts the topological SSH model form. The following discussion is restricted to the $\delta E = E_{J_0}$ case which is the simplest to obtain an analytical form because the system is in a product state at half-period. Similar considerations could be applied to the general case of $\delta E < E_{J_0}$. From this point onwards, we consider a constant hopping with the leads, i.e. $E_J^\ell(t) = E_0^\ell$.

At $t = \tau/2$, the system takes the form of the topological SSH model. The ground state of the system is a product state of the dimers of the inter-type and the edges states. The intra-cell hopping is completely switched off, i.e. $E_{J_1} = 0, E_{J_2} = 2E_{J_0}$.

$$|\psi\rangle = |1\rangle \otimes |D_-\rangle_{23} \otimes \cdots \otimes |D_-\rangle_{N-2,N-1} \otimes |2N\rangle \tag{6.2.2}$$

where $|D_-\rangle = \frac{1}{\sqrt{2}}\begin{pmatrix}1 & 1\end{pmatrix}^T$ is the state of the dimer of lowest energy, $E_- = -E_{J_2}$ and $|1/2N\rangle$ are the two edges states of zero energy. The ground state energy is $E_0 = -(N-1)E_{J_2}$ and it is degenerate because of the zero-energy modes. The energy gap is the difference between the ground state energy and the first excited state energy. For a conserved particle number, as it is the case for the Rice-Mele model with open boundary conditions and no leads, the first excited state is degenerate, and corresponds to states in which one of the dimers has been excited to $|D_+\rangle$ state with energy $+E_{J_2}$. The first excited state energy is $E_1 = -(N-3)E_{J_2}$, and the gap is $E_g = 2E_{J_2}$ (this gap corresponds exactly to the particle-hole excitation gap). The many-body gap without considering particle number conservation is $E_g = E_{J_2}$.

In the presence of the boundary terms, the edge states of the SSH model are no longer of zero energy, and we will explain why. Because the intra-cell hopping vanishes at $t = \tau/2$, the Hamiltonian becomes a tensor product of boundary Hamiltonians and dimer Hamiltonians. The boundary Hamiltonian, in the Fock basis $\{|0\rangle, |1\rangle\}$, is,

$$H_{b_{L/R}} = \begin{pmatrix} 0 & -E_0^\ell e^{-i\phi_{L/R}} \\ -E_0^\ell e^{i\phi_{L/R}} & 0 \end{pmatrix} \tag{6.2.3}$$

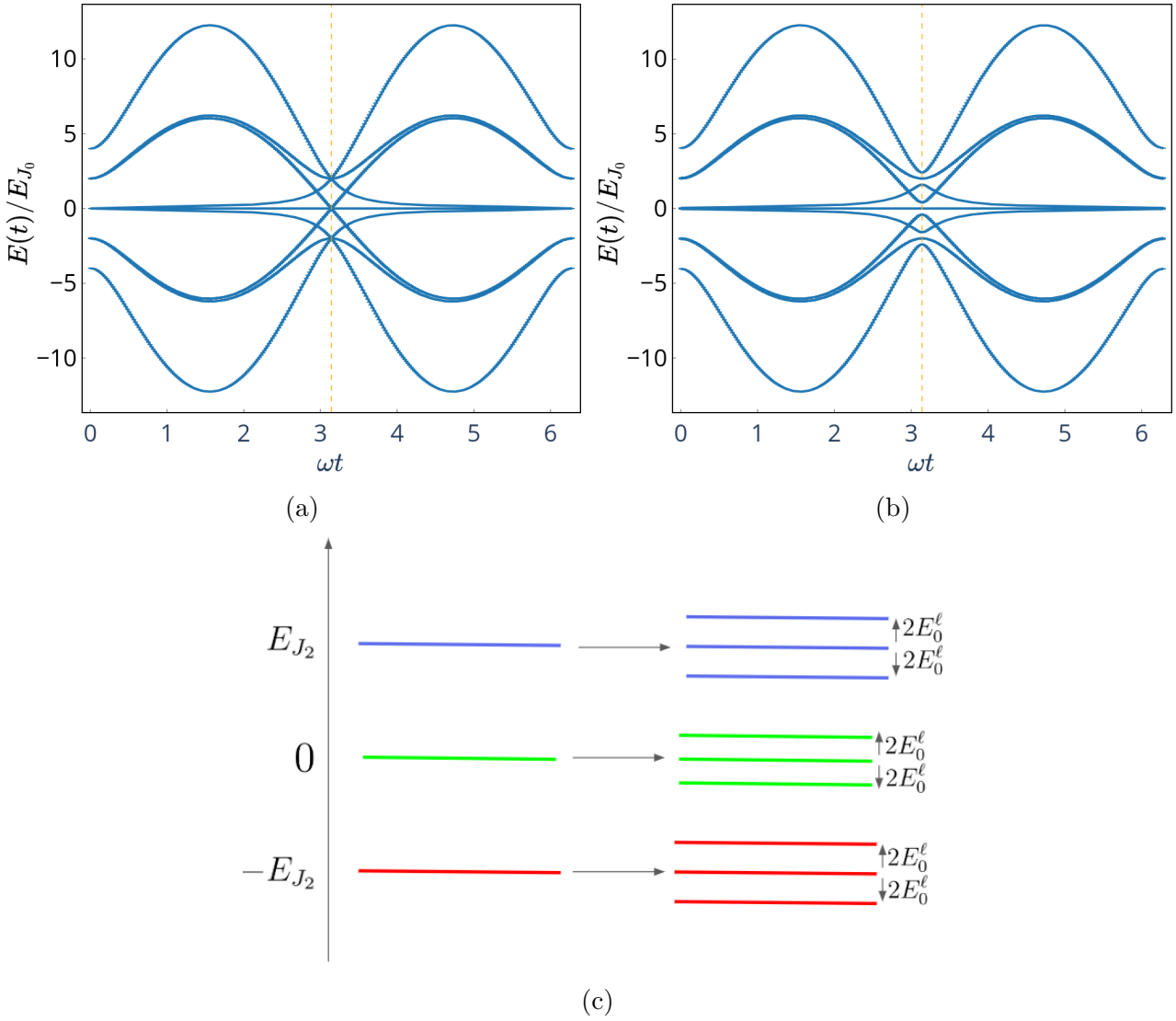

Figure 6.2: An example of degeneracy breaking by the boundary term for $L = 4$. The instantaneous many-body spectrum for (a) $E_0^\ell = 0$ and (b) $E_0^\ell = 0.2$. The appearance of a nonzero E_0^ℓ breaks the degeneracy of the energy levels at $t = \tau/2$ where the minimum gap is located. A simple sketch in (c) shows closely the effect of the boundary term at $t = \tau/2$. Before the introduction of the leads, each of the three energy levels are degenerate because of particle number conservation and of the zero-energy edge modes. But when $E_0^\ell \neq 0$, the particle number is not conserved anymore and the isolated sites at the ends of the chain are coupled to the leads. As a result, the degeneracy due to these factors breaks.

When $E_0^\ell = 0$, we obtain the usual Hamiltonian for the edges and the corresponding zero-energy edge states in the topological SSH model. Diagonalization of Eq. 6.2.3 yields,

$$|\psi_\pm\rangle = \frac{1}{\sqrt{2}}\left[e^{i\phi_{L/R}}|0\rangle \mp e^{-i\phi_{L/R}}|1\rangle\right] \tag{6.2.4}$$

with energies $E = \pm E_0^\ell$. The combined states for the boundary terms are given by Eq. 6.2.5-6.2.8.

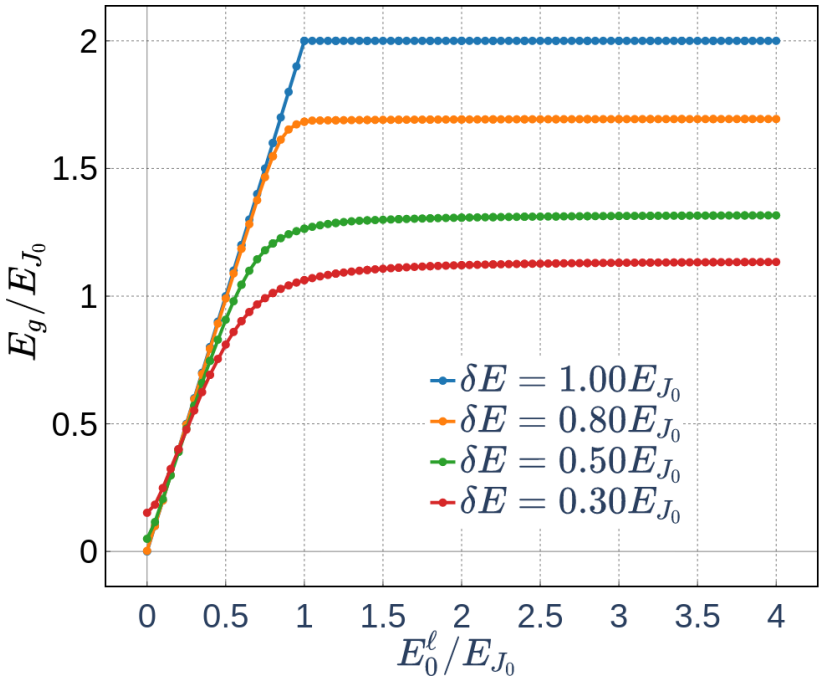

Figure 6.3: The many-body gap as a function of E_0^ℓ for various values of δE. At values $E_0^\ell > E_{J_0}$, the gap saturates to a final value. This value decreases with decreasing δE. Parameters: $\Delta = 3E_{J_0}, \phi = \pi/3$.

$$\left|\psi_1(E=-2E_0^\ell)\right\rangle = |\psi_-\rangle_1 \otimes |\psi_-\rangle_{2N} \tag{6.2.5}$$
$$|\psi_2(E=0)\rangle = |\psi_-\rangle_1 \otimes |\psi_+\rangle_{2N} \tag{6.2.6}$$
$$|\psi_3(E=0)\rangle = |\psi_+\rangle_1 \otimes |\psi_-\rangle_{2N} \tag{6.2.7}$$
$$\left|\psi_4(E=+2E_0^\ell)\right\rangle = |\psi_+\rangle_1 \otimes |\psi_+\rangle_{2N} \tag{6.2.8}$$

The relevant states in the topological SSH model all have zero energy. Therefore, E_0^ℓ breaks the degeneracy because of the edge states. At the same time, since it appears as a non-quadratic term, it breaks the degeneracy because of the particle number is not conserved. An illustrative example for $L = 4$ is demonstrated in Figure 6.2.

The overall ground state energy of the system (including the leads) at time $t = \tau/2$ is $E_0 = -(N-1)E_{J_2} - 2E_0^\ell$ and it is non-degenerate. The energy of the first excited state now can varied depending on the value of E_0^ℓ.

$$E_1 = \begin{cases} -(N-1)E_{J_2} & E_0^\ell < E_{J_0} \\ -(N-3)E_{J_2} - 2E_0^\ell & E_0^\ell > E_{J_0} \end{cases} \tag{6.2.9}$$

Therefore, the energy gap takes the following form,

$$E_g = \begin{cases} 2E_0^\ell & E_0^\ell < E_{J_0} \\ E_{J_2} & E_0^\ell > E_{J_0} \end{cases} \tag{6.2.10}$$

and $E_{J_2} = 2E_{J_0}$ at time $t = \tau/2$. This agrees with the numerical result of Figure 6.3 for $\delta E = E_{J_0}$. The same procedure applies to $\delta E \neq E_{J_0}$ however these cases are quite tricky to tackle analytically since they do not form product states but rather entangled states, due to the fact that neither of the two hopping parameters are completely switched off.

6.3 The quantization of the pumped charge

We now discuss about pumping following [26], in which we show the connection of the pumped charge to the Berry phase [3]. Assume we initialize the system in the many-body ground state $|\Psi_0(0)\rangle$ of Eq. 6.1.8. If the evolution is adiabatic then after time τ the system returns to the initial state and has acquired a phase factor,

$$|\Psi_0(\tau)\rangle \approx e^{i\alpha_0} |\Psi_0(0)\rangle \tag{6.3.1}$$

by virtue of the adiabatic theorem. The accumulating phase α_0 is the sum of the geometrical γ_0 and dynamical δ_0 phase associated with the ground state,

$$\alpha_0 = \gamma_0 + \delta_0, \quad \gamma_0 = \int_0^\tau dt \ \langle \Psi_0(t)|\partial_t \Psi_0(t)\rangle \,, \quad \delta_0 = -\int_0^\tau dt \ E_0(t) \tag{6.3.2}$$

The transferred charge over this period of time is, as usual, the time integral of the expectation value of the current operator,

$$Q = \frac{1}{\tau}\int_0^\tau dt \ \langle \mathcal{J} \rangle \,, \quad \langle \mathcal{J} \rangle = \langle \Psi_0(t)|\mathcal{J}|\Psi_0(t)\rangle \tag{6.3.3}$$

Given the discussion in Section 4.3 on the current operator, the insertion of the flux through the system is equivalent to twisted boundary conditions, therefore the current operator is simply given as the derivative of the Hamiltonian with respect to ϕ, the phase associated with the flux,

$$\hat{\mathcal{J}} = \partial_\phi \hat{H} \tag{6.3.4}$$

Eq. 6.3.3 is expressed as the sum of two contributions using the product rule for derivatives,

$$\langle \Psi_0(t)|\partial_\phi H|\Psi_0(t)\rangle = \partial_\phi \langle \Psi_0(t)|H(t)|\Psi_0(t)\rangle - \Big[\langle \Psi_0(t)|H|\partial_\phi \Psi_0(t)\rangle + c.c.\Big] \tag{6.3.5}$$

and we have $Q(\phi) = Q_d(\phi) + Q_g(\phi)$, where $Q_d(\phi)$ is the transferred charge due to the supercurrent and is associated with the dynamical phase,

$$Q_d(\phi) = -\int_0^\tau dt \ \partial_\phi E_0(t) \tag{6.3.6}$$

and $Q_g(\phi)$ is the pumped charge which is associated with the geometrical phase γ_0,

$$Q_g(\phi) = -\int_0^\tau dt \ \Big[\langle \Psi_0(t)|H|\partial_\phi \Psi_0(t)\rangle + c.c.\Big] \tag{6.3.7}$$

Admittedly, it is not obvious how this contribution is linked to the geometrical phase. After some manipulations shown in Appendix C, shows that indeed $Q_g = -\partial_\phi \gamma_0$. Therefore the total transferred charge is given by,

$$Q(\phi) = Q_d(\phi) + Q_g(\phi) = -\partial_\phi \delta_0 - \partial_\phi \gamma_0 \tag{6.3.8}$$

The transferred charge obviously depends on ϕ. Throughout the thesis, quantized transport was translated into quantized pumped charge, the transferred charge due to the slow modulation of the parameters of the Hamiltonian. This is linked to the geometric phase, which leads

[3] The Berry phase was experimentally measured in a Cooper pair pump by establishing a direct connection between the pumped charge and the Berry phase. This experiment became the first observation of the Berry phase in a superconducting circuit [55]

to the quantization of the pumped charge by integrating the relevant Berry curvature over time and momentum. In the present case, the total transferred charge is due to both the dynamical and geometrical phases, hence we do not expect any quantization. However, recall that the dependence of expectation values on ϕ is neglected in the limit of large system size, in accordance with [54]. Therefore, the charge due to the supercurrent vanishes because the ground state energy no longer depends on ϕ, and the derivative of it is zero. This is not the case with the geometrical phase, and thus the total transferred charge is equal to the pumped charge $Q \approx -\partial_\phi \gamma_0$ as $L \to \infty$.

In the general case of arbitrary L, to demonstrate the quantization of the overall transferred charge we integrate over all values of $\phi \in S^1$ [25].

$$Q = Q_d + Q_g = \int_0^{2\pi} \frac{d\phi}{2\pi}\, Q(\phi) \tag{6.3.9}$$

The charge due to the supercurrent is trivially zero,

$$Q_d = -\int_0^{2\pi} \frac{d\phi}{2\pi}\, \partial_\phi \delta_0 = -\frac{\delta_0(2\pi) - \delta_0(0)}{2\pi} = 0 \tag{6.3.10}$$

while this is not the case with the pumped charge,

$$Q_g = -\int_0^{2\pi} \frac{d\phi}{2\pi}\, \partial_\phi \gamma_0 \neq 0 \tag{6.3.11}$$

After some manipulations, the pumped charge is expressed as the Chern number defined by the double periodicity of (ϕ, t)

$$Q_g = -i \int_0^{2\pi} \frac{d\phi}{2\pi} \int_0^{\tau} dt \, \Big[\langle \partial_\phi \Psi_0(t) | \partial_t \Psi_0(t) \rangle - c.c. \Big] = -\int_0^{2\pi} \frac{d\phi}{2\pi} \int_0^{\tau} dt \, \mathcal{B}^{(0)}_{\phi t} = -\mathcal{C} \tag{6.3.12}$$

The pseudomomentum ϕ has replaced the crystal momentum in the corresponding expression for the pumped charge in the Rice-Mele model, for periodic boundary conditions. The resulting quantization applies to any system size, as long as we can average over the parameter ϕ. In the opposite case, deviations from the quantized value due to the supercurrent contribution appear.

We have shown the Berry approach towards the quantization of the transferred charge. We now view our problem in the Floquet picture by considering the arguments of Subsection 3.4.2. In the adiabatic limit, the dynamical and geometrical phases are linked with the Floquet many-body quasienergies $\mathcal{E}_n$,

$$\mathcal{E}_n = -\frac{1}{\tau}\big(\gamma_0 + \delta_0\big) \tag{6.3.13}$$

Combining Eq. 6.3.8 and Eq. 6.3.13, we express the transferred charge as the derivative of the quasienergies with respect to ϕ.

$$Q(\phi) = \tau \partial_\phi \mathcal{E}_n \tag{6.3.14}$$

Averaging out ϕ, this becomes,

$$Q = \int_0^{2\pi} \frac{d\phi}{2\pi}\, Q(\phi) = \tau \int_0^{2\pi} \frac{d\phi}{2\pi}\, \partial_\phi \mathcal{E}_n \tag{6.3.15}$$

When we average over ϕ, the contribution from the dynamical phase is zero, thus the quasienergies are linked to the geometrical phase only. Thus, the pumped charge corresponds to the winding of the many-body quasienergies as ϕ runs from 0 to 2π,

$$Q = \tau \int_0^{2\pi} \frac{d\phi}{2\pi}\, \partial_\phi \mathcal{E}_n = W, \quad W \in \mathbb{Z} \tag{6.3.16}$$

The integer number W is called the winding number of the many-body quasienergy and counts how many times $\mathcal{E}_n$ wraps up about the Floquet zone as ϕ runs over its domain. The winding of $\mathcal{E}_n$ relies solidly on the multivaluedness of the quasienergy. Recall that the quasienergy is uniquely defined, or single-valued, within a Floquet-Brillouin zone of width ω, but it is multivalued outside of it, since $\mathcal{E}_{n,m} = \mathcal{E}_n + m\omega,\ m \in \mathbb{Z}$.

Eq. 6.3.16 assumes that the system is initialized in the ground state of the Hamiltonian and that this corresponds to a many-body Floquet state. In other words, there is an exact overlap of the ground state to one of the Floquet states, such that the overlaps with the rest of the Floquet states are exactly zero. It is a rephrasing of the statement provided in Subsection 3.4.2, in which the Floquet states and the Hamiltonian eigenstates coincide in the adiabatic limit.

The result of Eq. 6.3.16 can be generalized by including the occupations of all Floquet states and the contributions thereof to the current. We recall the result of Eq. 3.4.10. The result is generalized to that of twisted boundary conditions by simply omitting setting the phase to zero. Thus, the charge is expressed in terms of ϕ,

$$Q(\phi) = \tau \sum_\nu \mathcal{N}_\nu(\phi)\, \partial_\phi \mathcal{E}_\nu(\phi) \tag{6.3.17}$$

where the overlaps where $\mathcal{N}_\nu(\phi) = |\langle \Psi_0(0) | \Phi_\nu(\tau)\rangle|^2$ represent the occupations of the Floquet states $|\Phi_\nu(\tau)\rangle$, given that the initial state of the system is the Hamiltonian ground state $|\Psi_0(0)\rangle$. Integrating out ϕ, Eq. 6.3.17 becomes,

$$Q = \tau \sum_\nu \int_0^{2\pi} \frac{d\phi}{2\pi}\, \mathcal{N}_\nu(\phi)\, \partial_\phi \mathcal{E}_\nu \tag{6.3.18}$$

We retrieve Eq. 6.3.15 when the ground state coincides exactly with one of the Floquet states, i.e. $\mathcal{N}_\nu = \delta_{\nu,n}$ where n is the index of the corresponding Floquet state of exact overlap.

6.4 Short-time dynamics

Let us first study the short-time dynamics to examine what happens to the system as it evolves in time. Later on, we will mostly focus on the pumped charge at the infinite-time limit.

We study the pumped charge for a few periods of the drive to examine its behavior.

$$Q(t) = \int_0^t dt'\ \mathrm{tr}\{\rho(t')\mathcal{J}(t')\} \tag{6.4.1}$$

where the $\rho(t) = U(t)\rho_0 U^\dagger(t)$ is the time-evolved density matrix in the Schrödinger picture. One can solve the von Neumann equation $\dot{\rho} = -i[H, \rho]$ to determine how the density matrix of the system evolves in time. However, we can tackle the problem from a time evolution operator perspective by determining $U(t)$ and then finding $\rho(t)$. Since the system is under the influence of a periodic drive, then we can simply use the Floquet theorem,

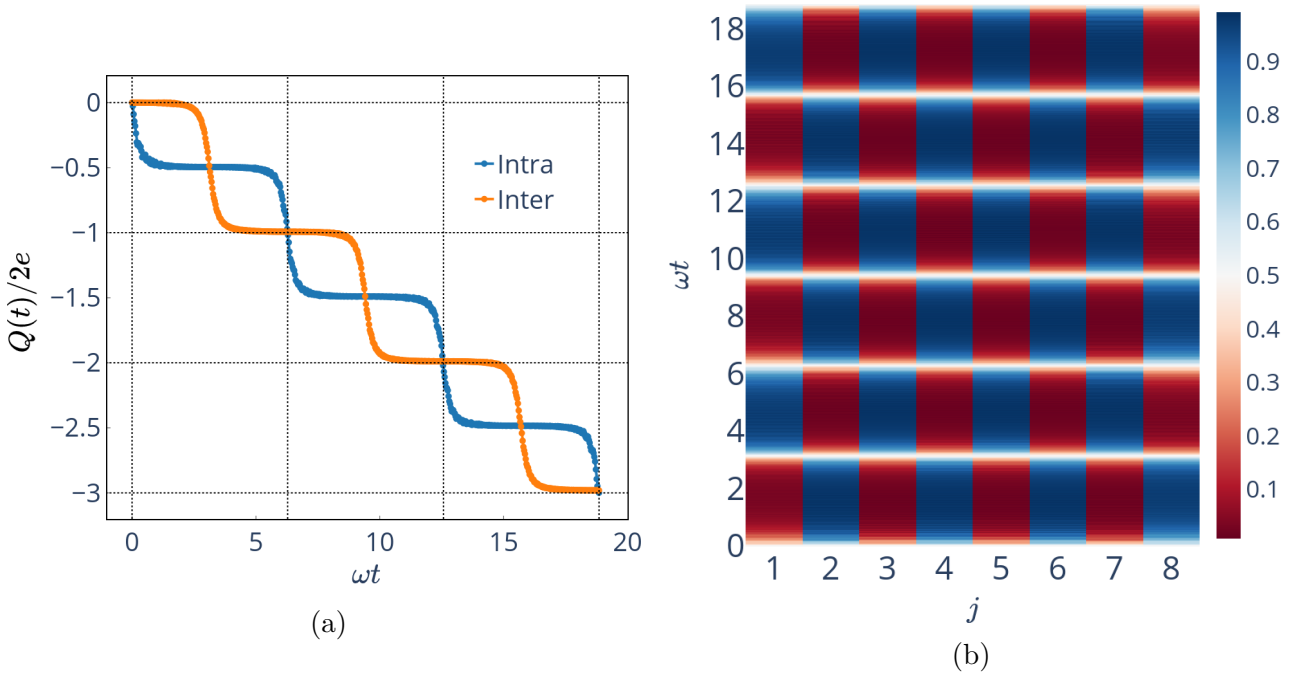

(a) (b)

Figure 6.4: The time evolution of the pumped charge of Eq. 6.4.1 and the occupation numbers of the real lattice for 3 periods. (a) The pumped charge associated with the intra-cell (blue) and inter-cell (orange) currents are shown. After the completion of a driving period, the average pumped charge is quantized. (b) The occupations (colorbar) of each island are shown. After half a period, either an intra- or inter-cell current flows depending on which sublattice is occupied, either A or B. Parameters chosen: $\delta E = E_{J_0}, \Delta = 3E_{J_0}, E_0^{\ell} = E_{J_0}, \omega = 0.1E_{J_0}, \phi = \pi/3, L = 6$

$$U(t + m\tau) = U(t)[F(\tau)]^m, \quad m \in \mathbb{N} \tag{6.4.2}$$

which requires knowledge of the time evolution operator within a period of the driving and the Floquet operator.

In Figure 6.4a, the pumped charge of Eq. 6.4.1 as a function of time is displayed. We consider separately the current generated across sites within a unit cell (intra-cell current) and sites of adjacent unit cells (inter-cell current). Evidently, at stroboscopic times $t = m\tau$ where m is an integer, the charge of Eq. 6.4.1 is quantized. Throughout the evolution, only one type of current is non-zero. This is a consequence of the choice $\delta E = E_{J_0}$, a choice that corresponds to states of isolated dimers at some time moments, when current flows. This is also evident from the occupations of the sites of the array, as seen in Figure 6.4b. During the first half period, particles occupy the sites of sublattice B. Then, at the second half, there is a inter-cell current and particles move to sites the sites of sublattice A. This current is generated at $t \approx \tau/2$ at which the sytem is in a state of isolated dimers of the inter type, the intra-cell hopping is zero. Notice that at the same time, particles can hop in or out of the system to the leads. Likewise, intra-cell current is generated at times $t = 0$ and $t = \tau$ such that the average intra-cell current over a period is quantized to one.

We now take a different approach and perform a detailed study of the quantization of the pumped charge.

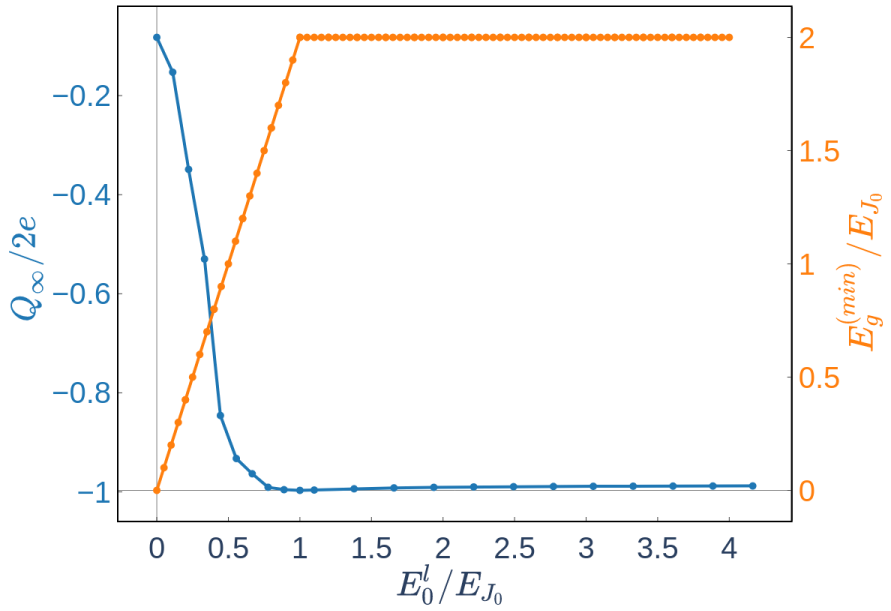

Figure 6.5: The pumped charge (at the infinite-time limit) and the energy gap as a function of E_0^ℓ. As we increase E_0^ℓ, pumped charge becomes quantized once adiabaticity is established, while at $E_0^\ell = E_{J_0}$ the gap adopts its final value of $E_g = 2E_{J_0}$. Parameters chosen: $\delta E = E_{J_0}, \Delta = 3E_{J_0}, \omega = 0.1E_{J_0}, \phi = \pi/3, L = 6$

6.5 Pumping in the presence of the leads

We have discussed several aspects of the new problem at hand. We considered the typical Josephson junctions array and introduced external superconducting leads at the edges of the array. Cooper pairs are allowed to move in or move out of the array. The phase bias induced by the superconducting leads, along with time, are the two relevant periodic parameters which in principal can generate quantized current.

As we have emphasized earlier, unitarity is still preserved. We can still diagonalize the Hamiltonian directly, but we do that considering the full Hilbert space since particle number is no longer conserved. This prevents us from studying arrays with a large number of islands, as in the case of the periodic Rice-Mele model. We primarily focus on the $\delta E = E_{J_0}$ case to get an insight of how the system behaves. However, as we find out, $\delta E = E_{J_0}$ exhibits some interesting features that cannot be seen for $\delta E \neq E_{J_0}$. Furthermore, the Josephson energy of the junctions between the array and the leads is taken to be constant in time.

We first want to examine whether quantized pumping can be achieved in the scenario where we have attached superconducting leads to the system. For this cause, we are concerned with the pumped charge at the infinite-time limit, given by Eq. 3.4.9 and was derived within the Floquet representation. Clearly, we want to see whether quantization of the particle current persists for long times and it is not a feature observed merely in short time scales. Figure 6.5 shows the pumped charge as a function of the Josephson energy associated with the hopping between leads and the system, E_0^ℓ. The many-body gap is also displayed to view the correspondence between the two. While E_0^ℓ is much smaller than E_{J_0}, the pumped charge is not quantized. One could say that within this range of values of E_0^ℓ, the gap is such that nonadiabatic effects take place and prevents the quantization of the pumped charge. As E_0^ℓ approaches E_{J_0}, i.e $E_0^\ell > 0.8E_{J_0}$, the pumped charge becomes quantized. The developed gap is much larger than

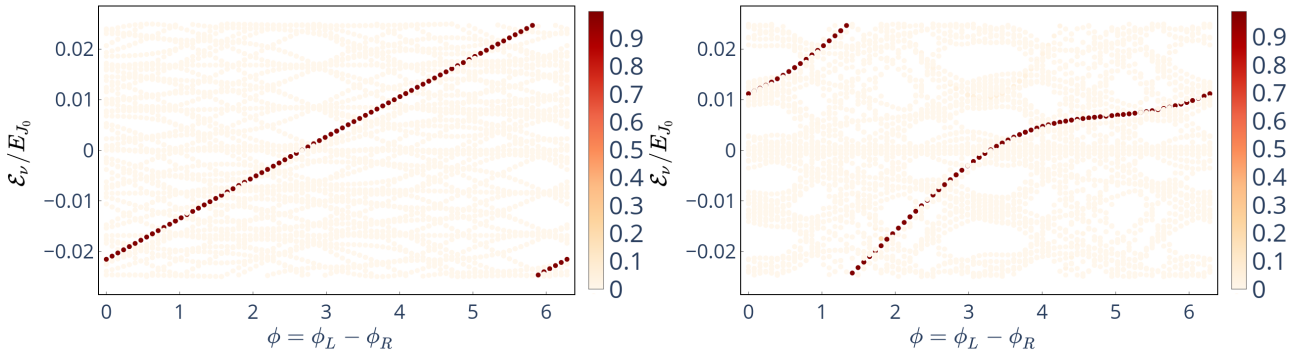

(a) (b)

Figure 6.6: The nontrivial winding of the quasienergies over the Floquet-Brillouin zone as a function of ϕ, for (a) $\delta E = E_{J_0}$ and (b) $\delta E = 0.5E_{J_0}$. The colorbar shows the occupation number of the Floquet states. Parameters: $\Delta = 3E_{J_0}, E_0^\ell = E_{J_0}, \omega = 0.05E_{J_0}, L = 6$.

the driving frequency and adiabaticity is established, thus the pumped charge is quantized. At $E_0^\ell = E_{J_0}$, the many-body gap admits its final value of $2E_{J_0}$, as discussed in Section 6.2, and the quantization of the pumped charge persists. As E_0^ℓ exceeds E_{J_0}, the quantization is preserved and the gap is mantained at $2E_{J_0}$. For a very large coupling with the leads, the first and last sites are effectively "swallowed" by the superconducting leads, thus making the system two sites shorter.

It should be stated that the pumped charge in Figure 6.5 is evaluated on a single value of ϕ and a relatively small system size is considered $L = 6$. Yet the pumped charge is quantized, even though in the latter section we emphasized that quantization is achieved when ϕ is averaged out. To examine this situation, we look at the quasienergies as a function of ϕ. For each value of ϕ, we diagonalize the Floquet operator obtaining the many-body quasienergies and the Floquet states. By constructing the corresponding resolution of identity, we can project the Hamiltonian ground state and calculate the occupations of the Floquet states. The quasienergies and the occupations of the Floquet states are the relevant quantities to determine if the pumped charge comes out to be quantized or not based on Eq. 6.3.18. Figure 6.6a shows the winding of the quasienergies as ϕ runs over its domain, which occurs once and thus the pumped charge is quantized. There is a remarkable feature; this winding happens in a linear fashion, the slope is constant across ϕ. This automatically means that whatever value of ϕ we choose to calculate the charge, as in the case with Figure 6.5, the pumped charge will be quantized. This is evident if we look into Eq. 6.3.18. Because of periodicity across both directions, the slope of the line comes out to be $\partial_\phi \mathcal{E}_\nu = \omega/2\pi = 1/\tau$. At the same time, for every value of ϕ, the Hamiltonian ground state coincides with a Floquet state, i.e. $\mathcal{N}_\nu = \delta_{\nu,\mu(\phi)}$ [4] . Therefore, the pumped charge (in units of the particle charge $Q = -2e$) is,

$$Q = \tau \int_0^{2\pi} \frac{d\phi}{2\pi} \partial_\phi \mathcal{E}_{\mu(\phi)}(\phi) = \tau \int_0^{2\pi} \frac{d\phi}{2\pi} \frac{1}{\tau} = 1 \tag{6.5.1}$$

This we already know. It does not justify the fact that the charge is quantized for a single value of ϕ. From the previous section recall that,

$$Q = \int_0^{2\pi} \frac{d\phi}{2\pi} Q(\phi), \quad Q(\phi) = \tau \partial_\phi \mathcal{E}_\nu \tag{6.5.2}$$

[4]For each value of ϕ, the ground state can coincide with a different Floquet state.

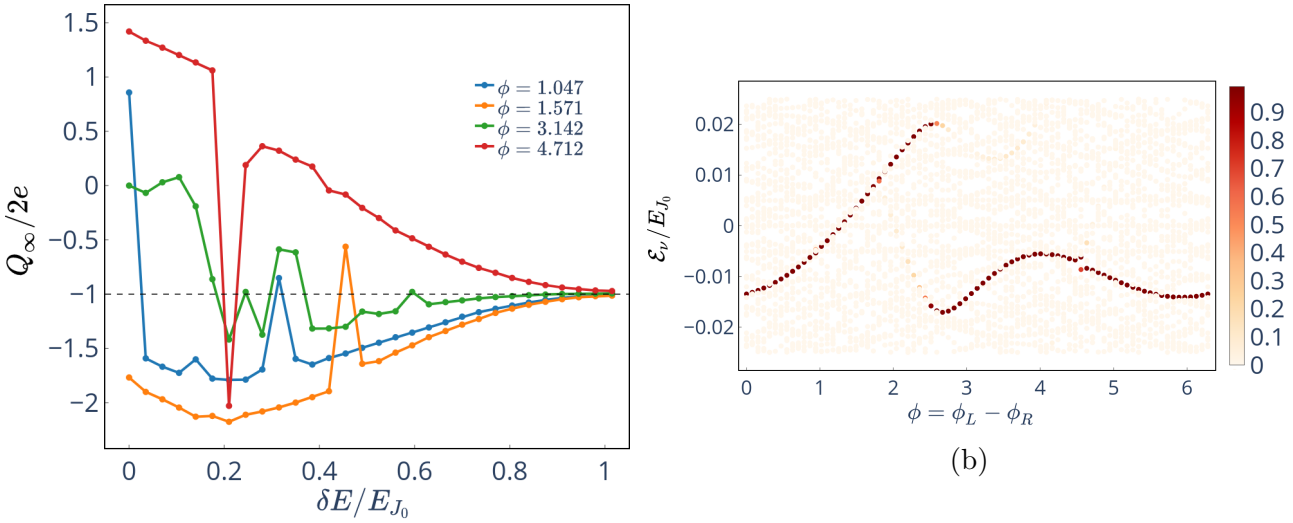

(a) (b)

Figure 6.7: (a) The pumped charge as a function of δE for various values of ϕ. As $\delta E \to E_{J_0}$, the pumped charge becomes less dependent on ϕ. (b) The quasienergy spectra as a function of ϕ for $\delta = 0.25E_{J_0}$. The gaps appear due to nonadiabatic effects described in the text. The colorbar shows the occupation number of the Floquet states. Parameters: $\Delta = 3E_{J_0}, E_0^\ell = E_{J_0}, \omega = 0.05E_{J_0}, L = 6$

and since $\partial_\phi \mathcal{E}_\nu = 1/\tau$, then $Q(\phi) = 1$, $\forall \phi \in S^1$ [5] . This independence of the pumped charge on ϕ for $\delta E = E_{J_0}$ may be attributed to the fact that the sites are weakly connected because one of the two hopping parameters is small or zero, throughout a driving period. The ground state projector is essentially localized at all times, therefore the expectation value of the pumped charge will be independent of ϕ, irrespective of the other parameters and the system size.

As emphasized, this observation is a consequence of the choice $\delta E = E_{J_0}$. For instance this does not occur for $\delta E = 0.5E_{J_0}$, see Figure 6.6b. Even though the quasienergies still winds about the Floquet zone in a non-trivial way, the formed curve across ϕ is not linear, hence the derivative of the quasienergy with respect to ϕ is not constant and the argument does not hold for this case. In general, for $\delta E \lesssim E_{J_0}$ we expect the derivative of the quasienergy across ϕ to be approximately constant. In this occasions, the evaluation of the pumped charge for a single value ϕ would deviate slightly from the quantized value. Figure 6.7a supports this statement, in which the pumped charge as a function of δE is displayed for various values of ϕ. As δE approaches E_{J_0}, all ϕ curves tend asymptotically towards the quantized value. In this regime, the pumped charge becomes independent of ϕ. For values of δE away from E_{J_0} we start seeing a strong dependence on ϕ as we expected. As we move towards smaller values of δE, the integral over ϕ becomes a necessary step. At the same time however, we need to consider how the many-body gap is affected by the change in δE, see Figure 6.3 for $E_0^\ell = E_{J_0}$. The reduction in the gap value can lead to breakdown of adiabaticity for a fixed driving frequency. This is reflected in Figure 6.7b for $\delta E = 0.25E_{J_0}$. At some values of ϕ the quasienergy curve is discontinuous. This is attributed to the fact that more than one Floquet state become populated, because the evolution is not strictly adiabatic anymore and this induces gaps in the quasienergy spectrum [28].

[5] Note that $Q(\phi)$ is the pumped charge at the infinite-time limit.

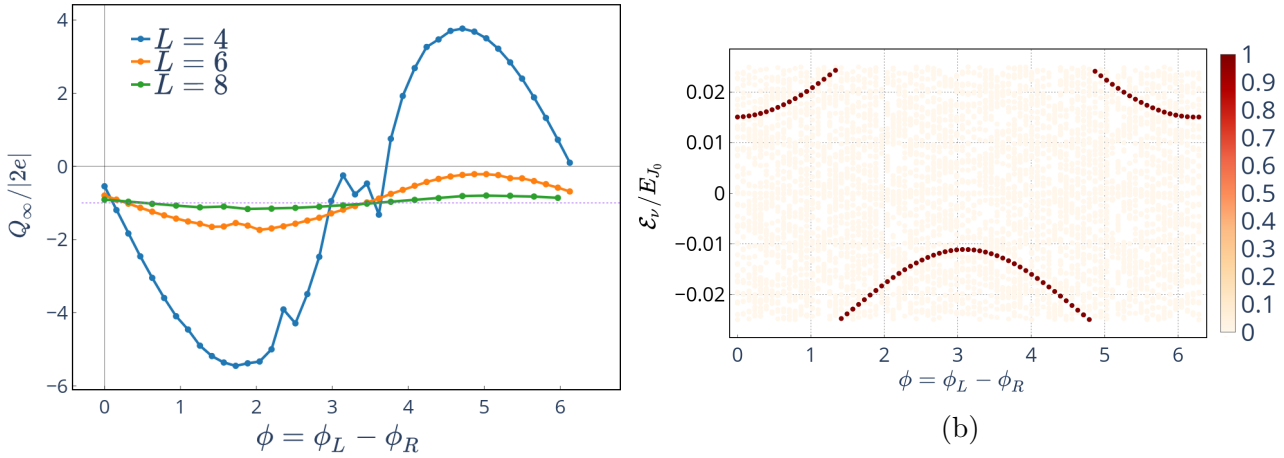

(a) (b)

Figure 6.8: (a) The pumped charge as a function of the phase ϕ for several values of the system size L. As the system size increases, the dependence of the pumped charge on ϕ diminishes. (b) An instance of a trivial winding of the quasienergies over the Floquet-Brillouin zone as a function of ϕ, for $\delta E = E_{J_0}$ and $A = 4E_{J_0}$ where A is the energy shift in the Josephson energy $E_{J_1}(t)$ of Eq. 4.2.5. The colorbar shows the occupation number of the Floquet states. Parameters: $\Delta = 3E_{J_0}, E_0^\ell = E_{J_0}, E_0^\ell = E_{J_0}, \omega = 0.05E_{J_0}, L = 6$

We showed that for $\delta E \sim E_{J_0}$, the dependence on ϕ becomes irrelevant. For a general δE, one has to integrate over all values of ϕ. However, we can still overcome this procedure by varying the system size. In the beginning of the chapter, we argued that the expectation values of the system [6] do not depend on ϕ in the limit of large system size, given that the ground state projector is exponentially localized. Figure 6.8a shows the dependence of the pumped charge on ϕ for increasing system size, for $\delta E = 0.5E_{J_0}$. Evidently, as the system size increases, the fluctuations in ϕ around the quantized value decrease, thus the reliance of the observable on ϕ gradually diminishes, in accordance with our previous statement.

For completness, let us show how the pumped charge is zero in the trivial phase. Recall from Chapter 4 of the Rice-Mele model, when adding a constant energy shift A in one of the hopping parameters, we exit the topological phase, as long as $A > 2\delta E$. In such instance, the quasienergy spectrum becomes that of Figure Eq. 6.8b. The quasienergy winds once in the clockwise but then winds in the opposite direction as ϕ runs from 0 to 2π, thus cancelling the first contribution and the overall winding is zero. Thus the pumped charge is zero, as expected since by adding $A > 2\delta E$ to one of the hopping parameters, the system is admitted to a topologically trivial phase.

6.6 On-site disorder

We now study the effect of disorder in our problem. We have discussed disorder in Chapter 5, where we showed that the quantization of the pumped charge persists as long as the disorder does not close the excitation gap. When the latter occurs, then the quantization breaks down and as the disorder keeps increasing, the system is admitted to an insulating phase in which

[6] This statement applies for a gapped, local Hamiltonian which is the case for our system.

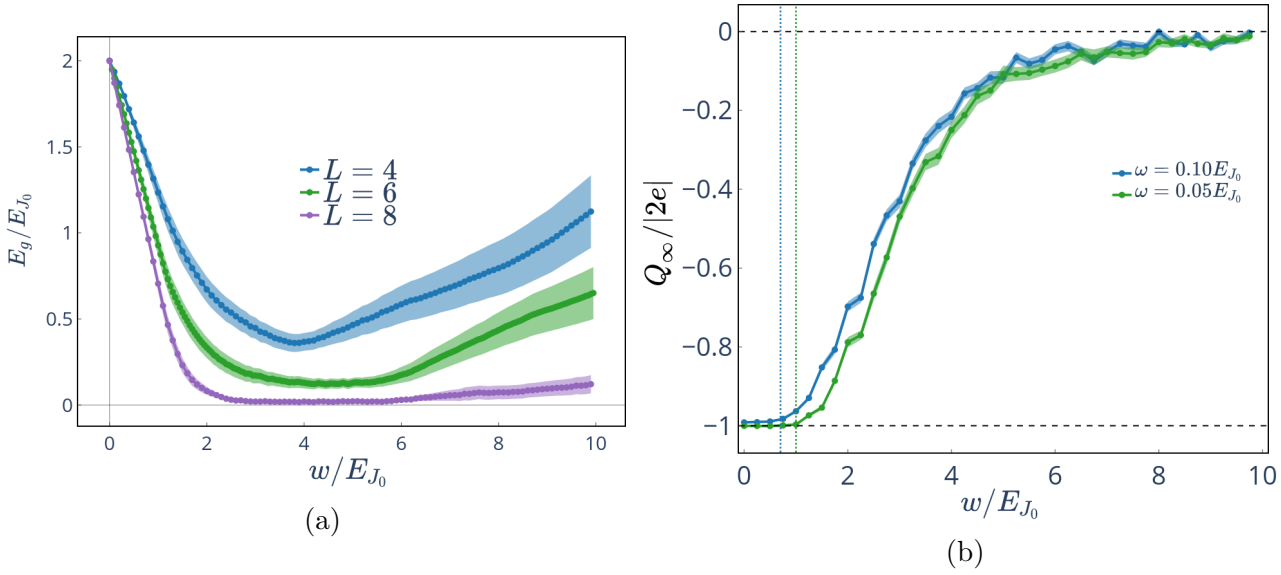

Figure 6.9: Introduction of on-site disorder. (a) The saturation of the gap due to increasing disorder, and how the value of saturation depends on the system size. (b) The insensitivity of the pumped charge against disorder and the breakdown of it at strong disorder. Parameters chosen: $\delta E = E_{J_0}, \Delta = 3E_{J_0}, E_0^\ell = E_{J_0}, L = 6$.

the Floquet states are completely localized. In the current problem, the relevant gap is the many-body gap.

We consider on-site disorder of the form,

$$\hat{H}_{dis} = \sum_i \delta\mu_i \, \hat{a}_i^\dagger \hat{a}_i \tag{6.6.1}$$

where $\delta\mu_i$ are random variables, sampled from a uniform distribution $\mathcal{U} = [-w, w]$, where w is the strength of the disorder. The case of $\delta E = E_{J_0}$ is discussed here, and the many-body gap at zero disorder is $E_g = 2E_{J_0}$. Because disorder is represented by random variables, we ought to take the average over a number of disorder configurations for the pumped charge and the many-body gap.

We turn to disorder and we study the behavior of the pumped charge and at the same time the many-body gap. As disorder increases, the many-body gap decreases while the transport is still quantized, see Figure 6.9. As the many-body gap keeps decreasing with increasing disorder for a fixed driving frequency, adiabaticity breaks down and thus the quantization ceases. This is evident by looking at Figure 6.9b when we compare data between different driving frequencies. It is apparent that the smaller the frequency, the more the quantization persists. For $\omega = 0.05E_{J_0}$, the quantization is robust up to $w \sim E_{J_0}$, the energy scale associated with Cooper pair tunneling. For larger disorder strength, quantization breaks down and the system is directed towards a trivial, insulating phase. Once again, disorder generates a phase transition from a topological to trivial state. In this topologically trivial state, the Floquet states become localized due to disorder and thus the particle current vanishes.

It is worth mentioning that the gap does not actually close for small system sizes, but rather approaches a finite value. This is related to the finite size of the system and subsequently the

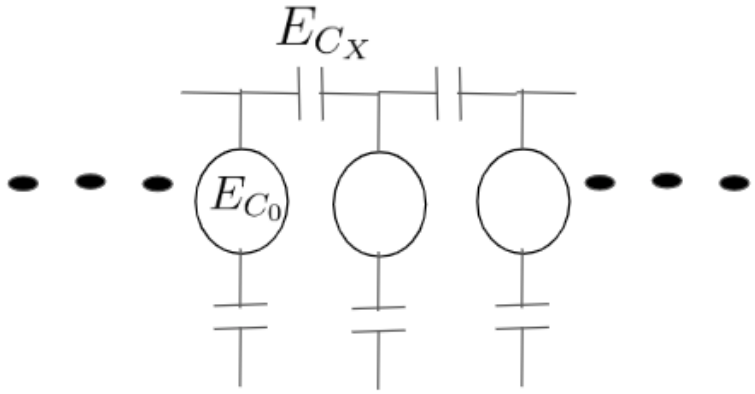

Figure 6.10: A sketch of the Josephson junctions array with nearest neighbour interactions.

finite number of many-body states. As the system size increases, the gap tends to the value of zero.

6.7 Nearest-neighbour interactions

Finally, we consider the effect of interactions and how the observables, in particular the pumped charge, is affected by them. This discussion is focus on $\delta E = E_{J_0}$. The discussion on interactions go back to Chapter 2, where we have assumed that interaction between Cooper pairs on different islands are negligible and focus entirely on the charging Hamiltonian of each island as the main contribution from Coulomb interactions. Then, the hardcore boson approximation focused on assuming that the charging energy is the dominant energy scale in the system, apart from the superconducting gap. We want to preserve this energy hierarchy and include the energy associated with nearest neighbour interaction, E_{C_X}. Therefore, for the setup we consider in this chapter to hold as it is, in the description we have adopted, we consider $E_{J_0}, E_{C_X} \ll E_{C_0}$. The interaction term arises from the charging Hamiltonian of Eq. 2.1.8.

$$\hat{H}_{int} = E_{C_X} \sum_i \left(\hat{N}_i - n_{g,i}\right) \cdot \left(\hat{N}_{i+1} - n_{g,i+1}\right) \tag{6.7.1}$$

where we assume a unique interaction energy E_{C_X}. The lattice index i runs over the number of islands minus one. Depending on the parity of the lattice index i, the induced charge adopts the form of driving of either sublattice A or B, based on Eq. 2.4.5, with $\frac{Q\delta V}{E_{g_0}} = \frac{\Delta}{E_{C_0}} \ll 1$. So far, we did not explicitly set a value for the charging energy E_{C_0}, but rather assumed to be much larger than the Josephson energy E_{J_0} through the approximation scheme we adopted. In the case of interactions we need to assign a value in the numerical simulations.

Figure 6.10 shows a sketch of the Josephson junctions array with interacting islands. We want to examine how nearest neighbour interactions impact the quantization of the pumped charge. We follow exactly the same recipe as we have done during this chapter for the evaluation of the pumped charge.

Let us look at the phase diagram of E_{C_X} vs E_0^ℓ, in Figure 6.11a, for $E_{C_0} = 8E_{J_0}$. There are clearly two distinct regions: one where the pumped charge is zero and another where the charge is quantized, in the presence of interactions. Let us carefully examine a cut along the E_{C_X} direction at E_0^ℓ (Figure 6.11b). Evidently, the pumped charge is remarkably robust against

the interaction strength. The quantization persists until $E_{C_X} \approx 3E_{J_0}$ and then it breaks down. However, we already reached a high enough value of the interaction strength at $E_{C_X} \approx 3E_{J_0}$, at which we begin to violate the energy hierarchy we assumed since E_{C_X} starts being comparable with the charging energy.

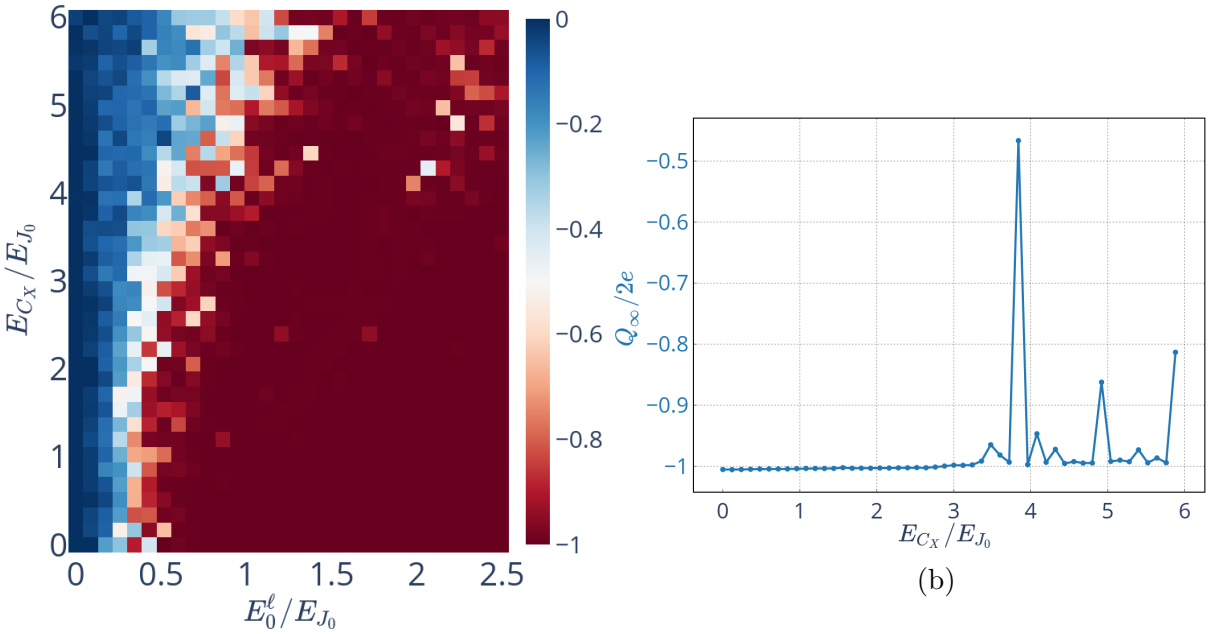

(a) (b)

Figure 6.11: Nearest neighbour interactions in a 1D Josephson junctions array with leads. (a) A phase diagram of E_{C_X} and E_0^ℓ. The colorbar corresponds to the pumped charge (in units of the particle charge). (b) The system is robust against interactions for $\delta E = E_{J_0}$ as explained in the text. Parameters chosen: $\delta E = E_{J_0}, \Delta = 3E_{J_0}, E_{C_0} = 8E_{J_0}, \omega = 0.05E_{J_0}, L = 6$. Additionally for (b) we have $E_0^\ell = E_{J_0}$.

How do we account for such robustness? We recall from Section 6.4 and Figure 6.4b, that during the time evolution, the particles occupy either the sites of sublattice A or B, and when tunneling between the two, a particle current is generated and ends up being quantized over a full driving cycle. Considering only nearest neighbour interactions simply does not affect the system, because when the particles "sit" at the sites of either of the two sublattices, there is no interaction going on between them. The nearest islands of a given island j are not occupied, thus the Cooper pair on the island does not interact with any particle. This is solidly a consequence of choice of the parameters associated with the Josephson tunneling, in particular $\delta E = E_{J_0}$. Therefore, for this choice δE, the nearest neighbour interaction does not affect the quantization of the pumped charge, if the parameters of the system are chosen such that quantized current is indeed induced. It should be emphasized that the pumped charge in Figures 6.11a and 6.11b is evaluated for a single value of ϕ, and this is justified by the arguments we provided in Section 6.5.

A way to extend and perhaps witness the effect of interactions will be to consider $\delta E \neq E_{J_0}$ such that the occupation of a single sublattice is avoided. Furthermore, for the case of $\delta E = E_{J_0}$ one can consider including next nearest neighbour interactions, which will have an impact because at this scenario, particles on the same sublattice will 'feel' each other.

Chapter 7

Conclusions and Outlook

Feynman's aspiration of simulating Nature using quantum computers has transitioned from a mere vision to a tangible reality. Thanks to technological progress, we now have the capability to simulate many-body phenomena on mesoscopic platforms. Our aspiration is to realize Thouless pumping on an array of Josephson junctions, a versatile and highly tunable device that has been in use for simulating many-body physics for several decades. The main challenge lies in achieving topological pumping in the presence of external leads. Introducing leads into the overall system can be relatively straightforward in these devices compared to other experimental setups. Hence, the primary objective of this thesis is to investigate and understand this particular scenario.

In conventional analog simulations, it is necessary to map the Hamiltonian of the setup to that of the original model, often by exploring different energy regimes. In this thesis, we chose to implement the pumping protocol of the Rice-Mele model, arguably one of the simplest examples of Thouless pumping. The foundation for implementing the Rice-Mele model on an array of Josephson junctions relied on the hardcore boson approximation, which was established under the condition of a large charging energy $E_{C_0} \gg E_{J_0}$. This approximation scheme reduces the original Hilbert space to a manageable size and eventually leads to the Rice-Mele model. By investigating the Rice-Mele model with periodic boundary conditions, the study showcased the underlying mechanisms of quantized pumping through two distinct approaches: Berryology and Floquet theory. The quantization of particle transport is expressed in terms of the Chern number defined on (k, t) or the nontrivial winding of the Floquet band over the Floquet-Brillouin zone. Furthemore, we explore disorder in the Rice-Mele model through different diagnostic tools such as the local Chern marker and the strange correlation function. The quantization is robust against disorder as long as the gap remains open. However, as disorder gets stronger the Floquet states become localized and the current vanishes. It is noteworthy that in the case of strong disorder, the strange correlation function breaks down. This happens in both the Rice-Mele model in Chapter 5 and the SSH model in the Appendix A. A comprehensive exploration of this issue could serve as an avenue for future research.

Chapters 4 and 5 provide valuable insights into the mechanism of topological pumping in the Rice-Mele model, shedding light on the influence of various factors such as finite size effects, nonadiabaticity and disorder. Building upon these insights, our investigation focuses on studying pumping in the presence of external superconducting leads, employing the pumping protocol of the Rice-Mele model. It is worth noting that due to the macroscopic description we adopt for the leads, the evolution of the system remains unitary. To properly account for the presence of the superconducting phase difference $\phi = \phi_L - \phi_R$, we establish a connection to twisted boundary conditions. As a result, the Hamiltonian and subsequently all the relevant

observables, depend on this ϕ. We demonstrate that the dependence on the superconducting phase difference disappears in the limit of a large system size and when δE approaches E_{J_0}, provided that the ground state projector is exponentially localized. The latter condition, i.e. $\delta E \to E_{J_0}$ is an essential feature observed even in systems of small size, like the ones we studied. For this choice of parameters, there is no longer a need to average out the phase ϕ. Additionally, our findings demonstrate that transport is quantized when the winding of the many-body quasienergy over the Floquet-Brillouin zone, as ϕ varies from 0 to 2π, is nontrivial. This quantization seems to be robust for disorder up to E_{J_0} and against nearest-neighbour interactions for the case of $\delta E = E_{J_0}$. Significantly, the consideration of this type of interaction becomes irrelevant for this specific parameter choice. However, future research can explore the inclusion of next-nearest-neighbor interactions, as it is anticipated to have an impact on the system dynamics and therefore pumping.

Our study is mainly focused on small arrays of Josephson junctions, where deviations from quantization can be observed. In our approach, the choice $\delta E = E_{J_0}$ seems like an excellent one to observe pumping in a straighforward manner. Even for $\delta E \neq E_{J_0}$, quantization of particle transport is still observed either by averaging out ϕ or choosing a larger system size, and as long as δE is not that small as to violate adiabaticity. Naturally, we aim to apply this approach to other models to investigate whether quantized pumping is observed in those cases as well. The Hofstadter-Harper model, with three sites per unit cell, appears to be a promising choice for such investigations, especially in the presence of interactions.

Possible routes for future research will be the relaxation of several of the assumptions we took. Indeed, relaxing the assumption of $E_{C_0} \gg E_{J_0}$ allows us to explore beyond the hardcore boson limit and investigate whether quantized pumping is still observed in the regime where multiple bosons can occupy a single island. This extension of the study can provide valuable insights into the robustness of the quantized pumping phenomenon under different system conditions.

In typical open systems, the presence of external baths introduces coupling to the system, resulting in dynamics that are no longer described by the von Neumann equation. In such instances, the Lindblad master equation is commonly employed to account for relaxation and decoherence processes, leading to a non-unitary evolution. However, our approach considers the external leads in a macroscopic and classical manner, where the state of the system is represented by a coherent state. An important direction for future research would be to investigate the validity of the approach and approximations we used for the leads.

Appendix A

The SSH model

The Rice-Mele model is built upon the widely recognized Su-Schrieffer-Heeger (SSH) model [56], and it is one of the simplest examples of quantum systems that exhibits topological features. In this Appendix, we briefly discuss the topological nature of the SSH model and we characterize phases with the strange correlation function [52, 53]. A peculiar feature arises in the overlap between a trivial and a topological SSH state, which we analyze in this Appendix.

A.1 The model

We consider a one-dimensional chain with two sites per unit cell, and a total number of unit cells N. Fermions are allowed to hop between adjacent sites. There are two types of hoppings, the intra-cell hopping which occurs between sites of the same unit cell J_1 and the inter-cell hopping which occurs between sites of adjacent unit cells J_2. The Hamiltonian is,

$$\hat{H}_{SSH} = -J_1 \sum_j \left(\hat{c}^\dagger_{2j-1}\hat{c}_{2j} + h.c.\right) - J_2 \sum_j \left(\hat{c}^\dagger_{2j}\hat{c}_{2j+1} + h.c.\right) \tag{A.1.1}$$

and the summation index j runs over the number of unit cells in the case of periodic boundary conditions. When open boundary conditions is conserved, we omit the contribution coming from hopping on the link between sites 1 and $2N$. Let us for now restrict to periodic boundary conditions. Because of space translation invariance, a map to momentum space can be realized through a Fourier transformation,

$$c^\dagger_{2j} = \frac{1}{\sqrt{L}} \sum_{k\in BZ} e^{-ikr} c^\dagger_{A,k}, \quad c_{2j} = \frac{1}{\sqrt{L}} \sum_{k\in BZ} e^{ikr} c_{A,k} \tag{A.1.2}$$

$$c^\dagger_{2j+1} = \frac{1}{\sqrt{L}} \sum_{k\in BZ} e^{-ikr} c^\dagger_{B,k}, \quad c_{2j+1} = \frac{1}{\sqrt{L}} \sum_{k\in BZ} e^{ikr} c_{B,k} \tag{A.1.3}$$

Then, the Hamiltonian takes the compact form of,

$$\hat{H} = \sum_k \hat{C}^\dagger_k H(k) \hat{C}_k, \quad \hat{C}_k = \begin{pmatrix} \hat{c}_{k/A} \\ \hat{c}_{k/B} \end{pmatrix}, \quad H(k) = \vec{h}(k)\cdot\vec{\sigma} \tag{A.1.4}$$

and $H(k)$ takes the form of a spin-1/2 particle in magnetic field $\vec{h}(k) = (h_x, h_y, h_z) = (-t_1 - t_2\cos 2k, -t_2 \sin 2k, 0)$, The matrices $\vec{\sigma}$ are the Pauli matrices in the sublattice space, $\{|A\rangle, |B\rangle\}$.

Topological features are manifested in the plane h_x vs h_y. We express the field components in terms of each other by eliminating the parameter k.

$$(h_x + J_1)^2 + h_y^2 = J_2^2 \tag{A.1.5}$$

This is the equation of a circle with center $(-J_1, 0)$ and radius J_2. The point of interest is the gapless point at $(J_1, J_2) = (0, 0)$ where the system admits a metallic phase. In order to characterize the topological phases in the SSH model, we employ concepts from Berryology [22]. Our parameter space is the one formed by h_x, h_y and we evaluate the Berry phase through the Berry connection $\gamma_n = \oint d\vec{h} \cdot \vec{\mathcal{A}}(\vec{h})$, and expresses the winding number about the gapless point. The Berry phase is non-zero when the circle of Eq. A.1.5 encloses the gapless point. A non-trivial winding number corresponds to the nontrivial topological state of the SSH model. This happens when $t_1 < t_2$. On the other hand, the circle does not enclose the gapless point when $t_1 > t_2$, which corresponds to the topologically trivial state. Therefore, the winding about the gapless point in the h_x-h_y plane represents the topological invariant of the system.

In the case of open boundary conditions, the distinction between topological and trivial phases remain the same. However, in the topological phase, zero-energy modes appear at the edges.

A.2 Overlap of states in the SSH model

In this section we examine the overlap between a trivial and a topological SSH state. The analysis will be of great importance when we implement the strange correlation function to the SSH model.

Let us define the state $|\psi\rangle$ as the state of the SSH model for any J_1, J_2, therefore we can write it as $|\psi(J_1, J_2)\rangle$. For simplicity, we express all energy quantities in terms of J_1, i.e. $J_1 = 1$, such that the inter-cell hopping is now denoted by $\Lambda = J_2/J_1$. Then, the state of the SSH model is thus reduced to $|\psi(\Lambda)\rangle$, and is topological when $\Lambda > 1$, while it becomes trivial when $\Lambda < 1$. Then the overlap of the reference state and the target state for the SSH model is,

$$\langle\Omega|\Psi\rangle = \langle\psi(\Lambda_1)|\psi(\Lambda_2)\rangle \tag{A.2.1}$$

where $\Lambda_{1/2}$ are some choices of the inter-cell hopping parameter in units of J_1. The phase transition occurs at $\Lambda = 1$ when the two hopping parameters are equal.

We focus entirely on the SSH model with periodic boundary conditions. The Hamiltonian in the momentum space is given by A.1.4. The diagonalization of $H(k)$ yields,

$$|\psi_\pm(k)\rangle = \frac{1}{\sqrt{2}}\Big[e^{-i\theta(k)}\,|A\rangle \pm |B\rangle\Big], \quad \varepsilon_\pm = \pm|h(k)| \tag{A.2.2}$$

where

$$e^{-i\theta(k)} = \cos\theta(k) - i\sin\theta(k) = \frac{h_x}{|h|} - i\frac{h_y}{|h|} \tag{A.2.3}$$

At half-filling, the ground state of the system is given by acting on the vacuum state $|0\rangle$ with the the creation operator of the lower band,

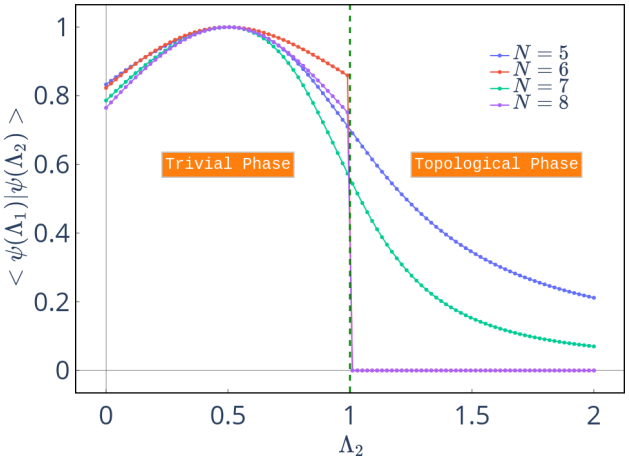

Figure A.1: THe overlap of SSH states with periodic boundary conditions for $\Lambda_1 = 0.5$ and varying Λ_2. When Λ_2 becomes greater than unity, the SSH model enters the topological phase. The overlap vanishes once $\Lambda_2 = 1$ for an even unit cell number while it behaves smoothly for an odd number.

$$|\psi(\Lambda)\rangle = \prod_k \gamma_k^\dagger |0\rangle\,, \quad \gamma_k^\dagger = \alpha_k^* c_{k/A}^\dagger + \beta_k^* c_{k/B}^\dagger \tag{A.2.4}$$

$\alpha_k = \frac{1}{\sqrt{2}} e^{-i\theta(k)}, \beta_k = -\frac{1}{\sqrt{2}}$ The overlap of states of the SSH model of different Λ is given as,

$$\langle\psi(\Lambda_1)|\psi(\Lambda_2)\rangle = \prod_k \left(\alpha_{1,k}\alpha_{2,k}^* + \beta_{1,k}\beta_{2,k}^*\right) = \prod_k \frac{1}{2}\left(e^{-i\theta_1(k)} e^{i\theta_2(k)} + 1\right) \tag{A.2.5}$$

Now, let's analyze this overlap considering the nature of periodic boundary conditions. With $c_{j+L} = c_j$, we find that $e^{ikL} = 1$, which leads to the quantization condition for the crystal momentum: $kL = 2n\pi \Rightarrow k = n\pi/N$, where $n \in 0, 1, ..., N-1$. We consider separately the the even and odd unit cell number. For an even number of unit cells, the point $k = \pi/2$ is included in the set of quantized values of k while for an odd unit cell number this is not true. This is evident when we consider the quantization condition for the crystal momentum. The point $k = \pi/2$ is included in the set when $n = N/2$. But since n is an integer, N must be even, thus for even unit cell number, we have,

$$k = n\frac{\pi}{N} = \frac{N}{2}\frac{\pi}{N} = \frac{\pi}{2} \tag{A.2.6}$$

When $k = \pi/2$, $h_y = 0$ and for any Λ we have,

$$e^{-i\theta} = \frac{h_x}{|h|} = \frac{J_2 - J_1}{|J_2 - J_1|} = \begin{cases} -1, & \Lambda < 1 \quad \text{trivial} \\ +1, & \Lambda > 1 \quad \text{topological} \end{cases} \tag{A.2.7}$$

Then, the product over k in Eq. A.2.5 includes the point $k = \pi/2$ for an even unit cell number. The relevant contribution to the product from the point $k = \pi/2$ is,

$$\frac{1}{2}\left(e^{-i\theta_1(\pi/2)} e^{i\theta_2(\pi/2)} + 1\right) = \begin{cases} 0 & \Lambda_1 < 1, \Lambda_2 > 1 \text{ or } \Lambda_1 > 1, \Lambda_2 < 1 \\ 1, & \Lambda_1, \Lambda_2 > 1 \text{ or } \Lambda_1, \Lambda_2 > 1 \end{cases} \tag{A.2.8}$$

Therefore, the overlap Eq. A.2.5 of a trivial $\Lambda < 1$ and a topological state $\Lambda > 1$ of the SSH model is zero for an even unit cell number hence we expect the strange correlation function to

diverge in this case. When the parity of the unit cell number is odd, then the overlap does not vanishes.

We also consider the case of antiperiodic boundary conditions i.e. $c_{j+2N} = -c_j$, which implies $e^{ikL} = -1$. The resulting quantization condition is,

$$k = (2n+1)\frac{\pi}{2N} = n\frac{\pi}{N} + \frac{\pi}{2N}, \quad n \in 0, 1, ..., N-1 \tag{A.2.9}$$

The antiperiodic conditions corresponds to a shift in the Brillouzin zone by $\pi/2N$. Evidently, the point $k = \pi/2$ appears in the set of momenta comprising the Brillouin zone when the parity of the unit cell number is odd. In particular, when $n = (N-1)/2 \Rightarrow k = \pi/2$, and this happens only when N is odd such that n is an integer. Applying similar reasoning as in the case of periodic boundary conditions, we find that the overlap between a trivial state and a topological state in the SSH model becomes zero for an odd number of unit cells when considering antiperiodic boundary conditions.

Periodic and antiperiodic boundary conditions can be seen as special cases of twisted boundary conditions We imagine that we insert a fictitious flux through the ring such that

$$c_{j+L} = e^{i\phi}c_j \tag{A.2.10}$$

Here, ϕ is the phase associated with the flux. Note that $\phi = 0$ corresponds the usual periodic BC while $\phi = \pi$ corresponds to the antiperiodic BC. The resulting quantization condition for momenta is,

$$e^{ikL} = e^{i2\pi n}e^{i\phi} \Rightarrow k = \frac{1}{L}\big(2n\pi + \phi\big), \quad n \in \{0, 1, 2, ..., N-1\} \tag{A.2.11}$$

The introduction of the flux results in a momentum shift in the Brillouin zone by ϕ/L. When the flux does not acquire the values of 0 or π, the overlap between the trivial and topological phases does not vanish for both even and odd unit cell numbers. However, the overlap behaves smoothly with the unit cell number when $\phi = \pi/2$. This becomes apparent when we look at the strange correlation function.

A.3 Characterization of topological phases using the strange correlator

We consider the strange correlation function for the SSH model. The strange correlator was introduced in the main text on Chapter 5 and implemented for the 2D static Rice-Mele model. The concept of the strange correlation function is to characterize a target state given a reference, typically trivial, state. We note that the Hilbert space of the two states must be the same.

We express the correlation in terms of the SSH state $|\psi(\Lambda)\rangle$, parametrized by $\Lambda = J_2/J_1$.

$$s[c^\dagger_{s,j}, c_{s',j'}] = \frac{\langle\psi(\Lambda_1)|c^\dagger_{s,j}, c_{s',j'}|\psi(\Lambda_2)\rangle}{\langle\psi(\Lambda_1)|\psi(\Lambda_2)\rangle} \tag{A.3.1}$$

Here, we use $c_{s,j}$ where $s \in \{A, B\}$ is the sublattice index and j is the unit cell index. The choice of operators is supported by the fact that the SSH Hamiltonian and the particle number operator commutes, thus the particle number is a symmetry. We are interested in the scaling of the strange correlation function with the system size.

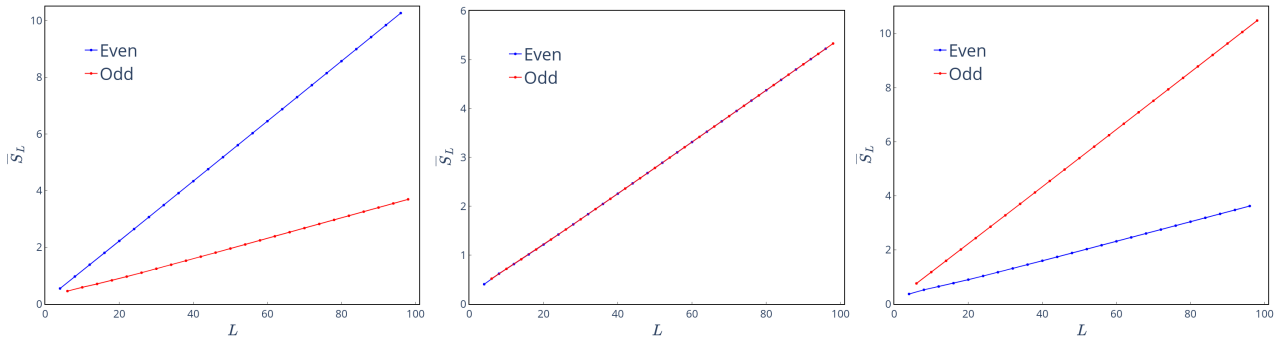

(a) (b) (c)

Figure A.2: The scaling of the strange correlator with the system size for the SSH model with twisted boundary conditions, for $\Lambda_1 = 0.5, \Lambda_2 = 2$ and (a) $\phi = \pi/4$, (b) $\phi = \pi/2$ and (c) $\phi = 3\pi/4$. The deviation between the trends of the odd and even unit cells number vanishes for $\phi = \pi/2$.

$$\bar{s}[c^\dagger, c]_{s,s'} = (\bar{S}_L)_{s,s'} = \frac{1}{L} \sum_{j,j'} \left| s[c^\dagger_{s,j}, c_{s',j'}] \right| \tag{A.3.2}$$

The behavior of this correlation function indicates whether the target state is topological or not, with the reference state being in the trivial phase. In the case of the SSH model, we choose $\Lambda_1 < 1$. According to our discussion in Chapter 5, for a one-dimensional system we expect that the strange correlation function scales linearly with the system size if the target state is topological. Instead, when the target state is trivial, the strange correlator tends to a constant.

We first study how the parity of the number of unit cells in combination with the boundary conditions, affect the strange correlation. The discussion involves the twisted boundary conditions, characterized by ϕ - see Eq. A.2.10. Evidently, we explicitly showed in the previous section that the overlap between a trivial and a topological state in the SSH model vanishes when the parity of the unit cell number is even and $\phi = 0$. This has a direct consequence for the strange correlation function described in Eq. A.3.1, causing it to diverge. The same occurs when we consider $\phi = \pi$ and the unit cell number has odd parity. By employing twisted boundary conditions, we can investigate the impact on the overlap and, consequently, on the strange correlator by testing various values of ϕ.

When $\phi \neq 0, \pi$, the overlap takes a non-zero value, resulting in a finite value for the strange correlator. However, there will be two distinct trends observed: one for even parity and another for odd parity. Initially, when $\phi = 0$, the two trends diverge completely, with the even parity trend becoming infinite. However, as we increase ϕ, the two trends gradually converge to each other, as illustrated in Figure A.2a. Eventually, when $\phi = \pi/2$, the two trends coincide and effectively merge into a single curve for the unit cell number as shown in Figure A.2b. The similar behavior occurs when we start from $\phi = \pi$ and move backwards to $\phi = \pi/2$, but instead the odd parity trend "starts" from infinity (Figure A.2c).

Given this unique feature, in order to use the strange correlator as a diagnostic tool in the SSH model, we adopt $\phi = \pi/2$. As already demonstrated in Figures A.2, the strange correlator scales linearly with the system size, an indication that the target state belongs to a different topological phase. Since the reference state is trivial, i.e. $\Lambda_2 = ...$, then the target state is a nontrivial topological state. The same linear trend appears for both $(s, s') = (A, A)$ and

$(s, s') = (A, B)$ [1], as shown in Figure A.3a. If instead the strange correlation function tends to a constant with increasing system size as in Figure A.3b, then we conclude that the target state belongs to the same phase as the reference state. Since the reference state is trivial, we can infer that the target state is also trivial.

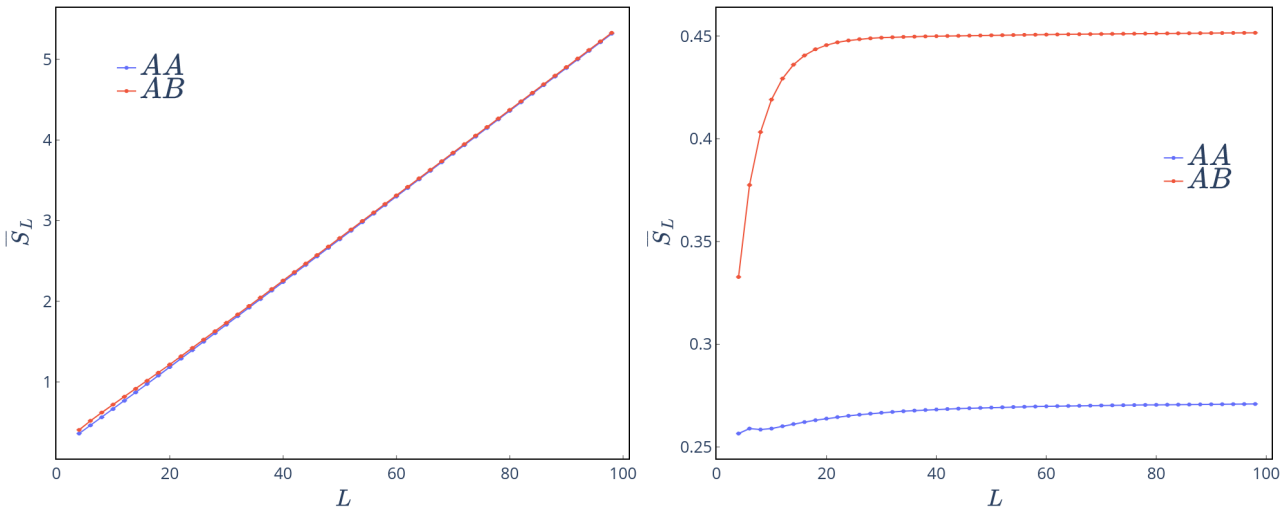

(a) (b)

Figure A.3: The scaling of the strange correlation function with the system size for the SSH model with twisted boundary conditions for $\phi = \pi/2$. The states involved in the strange correlator in (a) correspond to $\Lambda_1 = 0.5, \Lambda_2 = 2.0$ while in (b) correspond to $\Lambda_1 = 0.5, \Lambda_2 = 0.6$. The two curves in each plot correspond to the correlator with sublattice indices s, s'.

Finally, we study the presence of static, on-site disorder in the SSH model,

$$\hat{H}_{dis} = \sum_i \delta\mu_i \hat{c}_i^\dagger \hat{c}_i \tag{A.3.3}$$

where $\delta\mu_i$ is a random variable, sampled from a uniform distribution $\delta\mu_i \sim [-w, w]$ and w is the strength of the disorder. The topological SSH model is known to be robust against disorder and once the gap closes. Thus, the target state in the strange correlator will be a topological SSH state with disorder. For weak disorder, the strange correlation function still scales linearly with the system size (Figure A.4a, an indication that indeed even in the presence of disorder the SSH model is in the topological phase. This verifies the robustness against it. However, one expects that when disorder is strong, a phase transition occurs from the topological phase to a trivial state, thus the correlation function should tend to a constant value. This is not the case, as we see in Figure A.4b. The strange correlator breaks down for strong disorder. A brief discussion on the breakdown of the strange correlator in strong disorder is done in Chapter 5.

[1] The strange correlator of (B, B) is equivalent to (A, A), as well as (B, A) to (A, B) because of symmetry arguments.

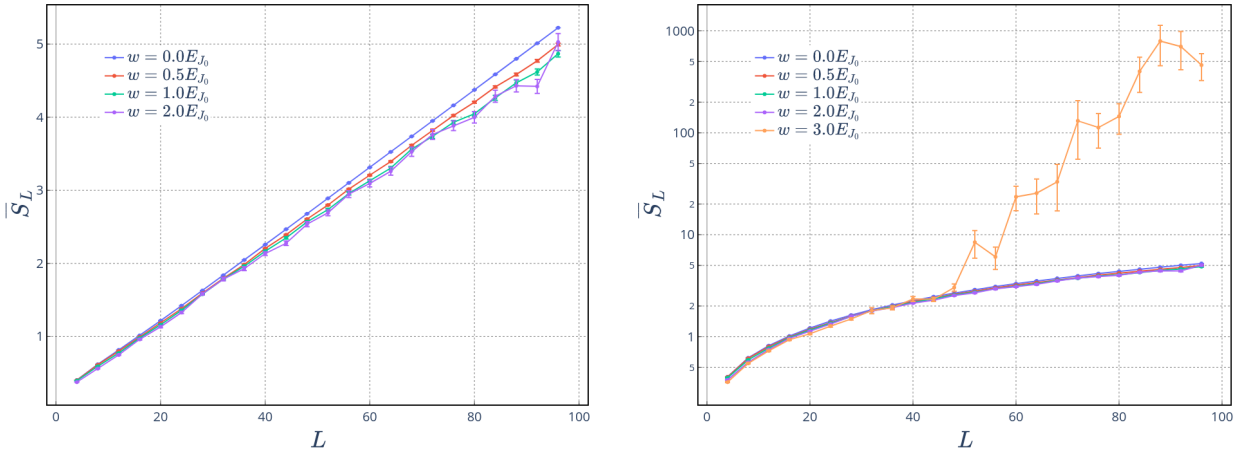

(a) (b)

Figure A.4: The scaling of the strange correlator with the system for the SSH model with twisted BCs in the presence of disorder. (a) For weak disorder the correlator scales linearly indicating that the target state is still topological. (b) For strong disorder, the correlator breaks down with unpredictable consequences. Parameters chosen: $\Lambda_1 = 0.5, \Lambda_2 = 2.0, \phi = \pi/2$.

Appendix B

Supplementary material for Chapter 3

In this appendix, we present the calculations regarding the pumped charge in the infinite-time limit of Subsection 3.4.1 in Chapter 3.

B.1 Pumped charge in the infinite-time limit

We want to show that the calculation of the pumped charge in the infinite time limit depends only on quantities defined within a single driving period. Our starting point is Eq. 3.4.8, but let us absorb the exponentials of the quasienergies in the time evolution operator using the statement of the Floquet theorem $U(t+m\tau,t_0) = U(t,t_0)[F(\tau)]^m$ and $F(\tau)\left|\Phi_\nu(\tau)\right\rangle = e^{-i\mathcal{E}_\nu(\tau)}\left|\Phi_\nu(\tau)\right\rangle$.

$$Q_\infty = \lim_{m\to\infty}\frac{1}{m}\sum_{\mu,\nu}\mathcal{C}_{\mu\nu}\int_0^{m\tau} dt\,\langle\Phi_\nu|\,U^\dagger(t,t_0)\mathcal{J}(t)U(t,t_0)\,|\Phi_\mu\rangle \tag{B.1.1}$$

We define the coefficients $\mathcal{A}_{\mu\nu}^{(m)}$ as follows,

$$Q_\infty = \lim_{m\to\infty}\frac{1}{m}\sum_{\mu,\nu}\mathcal{C}_{\mu\nu}\mathcal{A}_{\mu\nu}^{(m)}, \quad \mathcal{A}_{\mu\nu}^{(m)} = \int_0^{m\tau} dt\,\langle\phi_\nu|\,U^\dagger(t,t_0)\mathcal{J}(t)U(t,t_0)\,|\phi_\mu\rangle \tag{B.1.2}$$

and we focus on these for now. We write the integral over m periods as a sum of integrals over one period, starting from time 0 all the way up to time $m\tau$.

$$\begin{aligned}\mathcal{A}_{\mu\nu}^{(m)} = &\int_0^{\tau} dt\,\langle\Phi_\nu|\,U^\dagger(t,t_0)\mathcal{J}(t)U(t,t_0)\,|\Phi_\mu\rangle + \\ &\int_\tau^{2\tau} dt\,\langle\Phi_\nu|\,U^\dagger(t,t_0)\mathcal{J}(t)U(t,t_0)\,|\Phi_\mu\rangle + \\ &\int_{2\tau}^{3\tau} dt\,\langle\Phi_\nu|\,U^\dagger(t,t_0)\mathcal{J}(t)U(t,t_0)\,|\Phi_\mu\rangle + ...\end{aligned} \tag{B.1.3}$$

We use the statement of the Floquet theorem $U(t+m\tau,t_0) = U(t,t_0)[F(\tau)]^m$ to decompose the time evolution operator into the time evolution operator of one driving period and the Floquet operator. At the same time, because of the time periodicity of the current operator, we can change the limits of all integrals to that of the first period,

$$\mathcal{A}_{\mu\nu}^{(m)} = \int_0^\tau dt\, \langle\Phi_\nu|\, U^\dagger(t,t_0)\mathcal{J}(t)U(t,t_0)\,|\phi_\mu\rangle + \int_0^\tau dt\, \langle\Phi_\nu|\, F(\tau)U^\dagger(t,t_0)\mathcal{J}(t)U(t,t_0)F(\tau)\,|\Phi_\mu\rangle + \int_0^\tau dt\, \langle\Phi_\nu|\, [F(\tau)]^2U^\dagger(t,t_0)\mathcal{J}(t)U(t,t_0)[F(\tau)]^2\,|\Phi_\mu\rangle + ... \tag{B.1.4}$$

We now can use the action of the Floquet operator onto the Floquet states, which yields the exponentials of the quasienergies,

$$\mathcal{A}_{\mu\nu}^{(m)} = \int_0^\tau dt\, \langle\Phi_\nu(t)|\, \mathcal{J}(t)\,|\Phi_\mu(t)\rangle + \int_0^\tau dt\, e^{-i\Omega_{\mu\nu}\tau}\, \langle\Phi_\nu(t)|\, \mathcal{J}(t)\,|\Phi_\mu(t)\rangle + \int_0^\tau dt\, e^{-i\Omega_{\mu\nu}2\tau}\, \langle\Phi_\nu(t)|\, \mathcal{J}(t)\,|\Phi_\mu(t)\rangle + ... \tag{B.1.5}$$

where $\Omega_{\mu\nu} = \mathcal{E}_\mu - \mathcal{E}_\nu$ and $|\Phi_\nu(t)\rangle = U(t,t_0)\,|\Phi_\nu(\tau)\rangle$. We now write the Eq. B.1.5 in a compact form,

$$\mathcal{A}_{\mu\nu}^{(m)} = \sum_{l=0}^{m-1} e^{-i\Omega_{\mu\nu}l\tau} \int_0^\tau dt\ \ \langle\Phi_\nu(t)|\, \mathcal{J}(t)\,|\Phi_\mu(t)\rangle \tag{B.1.6}$$

and the pumped charge thus becomes,

$$Q_\infty = \lim_{m\to\infty} \frac{1}{m} \sum_{\mu,\nu} \mathcal{C}_{\mu\nu} \sum_{l=0}^{m-1} e^{-i\Omega_{\mu\nu}l\tau} \int_0^\tau dt\ \ \langle\Phi_\nu(t)|\, \mathcal{J}(t)\,|\Phi_\mu(t)\rangle \tag{B.1.7}$$

We now deal with the sum over complex exponentials. We define $\chi \equiv \Omega_{\mu\nu}\tau$, and it is uniquely defined on the unit circle. The sum corresponds to a geometric series,

$$S \equiv \sum_{l=0}^{m-1} e^{-i\chi l} = \frac{1 - e^{-i\chi m}}{1 - e^{-i\chi}} \tag{B.1.8}$$

If $\chi = 0, 2\pi, ...$, then the sum yields $S = m$ [1], therefore the pumped charge is non-zero for $\mu = \nu$. On the other hand, when $\mu \neq \nu$ and thus $\chi \neq 0, 2\pi, ...$, the pumped charge comes out to be zero when we take the limit over an infinite number of periods. Using these two facts, the summation over the Floquet indices μ, ν reduces to a summation over a single Floquet index,

$$Q_\infty = \sum_\mu \mathcal{N}_\mu \int_0^\tau dt\, \langle\Phi_\mu(t)|\, \mathcal{J}(t)\,|\Phi_\mu(t)\rangle \tag{B.1.9}$$

where $\mathcal{N}_\mu \equiv \mathcal{C}_{\mu\mu}$ are the occupations of the Floquet states, obtained by projecting the initial state to the Floquet basis.

[1] Note that the order of limits matters, first we take the limit of $\chi \to 0$, and then the limit $m \to \infty$.

B.2 The pumped charge as a function of the quasienergy

We want to take advantage of the properties of the time evolution operator and the Floquet operator to go even further from Eq. B.1.9. We start by isolating the integral of the expectation value of the current operator over a period,

$$Q_\infty = \sum_\mu \mathcal{N}_\mu \mathcal{I}, \quad \mathcal{I} \equiv \int_0^\tau dt \, \langle \Phi_\mu(t)| \, \mathcal{J}(t) \, |\Phi_\mu(t)\rangle \tag{B.2.1}$$

In Chapter 4, we show that the current operator is expressed as the derivative of the Hamiltonian with respect to a fictitious flux φ and then setting this flux to zero,

$$\mathcal{J} = \partial_\varphi H\big|_{\varphi=0} \tag{B.2.2}$$

Thus the integral $\mathcal{I}$ admits the following form,

$$\mathcal{I} = \int_0^\tau dt \, \langle \Phi_\mu(t)| \, \partial_\varphi H\big|_{\varphi=0} \, |\Phi_\mu(t)\rangle = \langle \Phi_\mu(\tau)| \int_0^\tau dt \; U^\dagger(t) \partial_\varphi H\big|_{\varphi=0} U(t) \, |\Phi_\mu(\tau)\rangle \tag{B.2.3}$$

and we have used $|\Phi_\mu(t)\rangle = U(t) \, |\Phi_\mu(\tau)\rangle$. Let us deal with this new integral separately (for brevity, we omit the setting the flux to zero notation, which we reinstate later),

$$\int_0^\tau dt \; U^\dagger(t) \partial_\varphi H \; U(t) \tag{B.2.4}$$

With some manipulations, we show that the above integral can be written in terms of the Floquet operator.

$$\begin{aligned}
\int_0^\tau dt \; U^\dagger(t) \partial_\varphi H \; U(t) &= i \int_0^\tau dt \; U^\dagger(t) \partial_t \partial_\varphi U(t) - \int_0^\tau dt \; U^\dagger(t) H(t) \partial_\varphi U(t) = \\
&= i \int_0^\tau dt \; U^\dagger(t) \partial_t \partial_\varphi U(t) + i \int_0^\tau dt \; \partial_t U^\dagger(t) \partial_\varphi U(t) = \\
&= i \int_0^\tau dt \; \partial_t \Big[U^\dagger(t) \partial_\varphi U(t) \Big] = \\
&= i U^\dagger(\tau) \partial_\varphi U(\tau)
\end{aligned} \tag{B.2.5}$$

where we have used $\partial_\varphi U(0) = 0$ while in the first line we used the Schrödinger equation for the time evolution operator.

$$i\partial_t U(t) = H(t) U(t) \Rightarrow i \partial_t \partial_\varphi U(t) = \partial_\varphi H(t) U(t) + H(t) \partial_\varphi U(t) \tag{B.2.6}$$

Then, we insert the result of Eq. B.2.5 to Eq. B.2.3, and subsequently to Eq. B.2.1, resulting in the following,

$$Q_\infty = \sum_\mu \mathcal{N}_\mu \, \langle \Phi_\mu(\tau)| \, i U^\dagger(\tau) \partial_\varphi U(\tau) \, |\Phi_\mu(\tau)\rangle \, |_{\varphi=0} \tag{B.2.7}$$

Notice that the pumped charge now depends on quantities related to the Floquet operator! We can take it a step further and use the action of the Floquet operator on Floquet states, thus obtaining the pumped charge in terms of the many-body quasienergy.

$$Q_\infty = \tau \sum_\mu \mathcal{N}_\mu \partial_\phi \mathcal{E}_\mu |_{\varphi=0} \tag{B.2.8}$$

Appendix C

Supplementary material to Chapter 6

We consider the contribution of the geometrical phase to the transferred charge. Our starting point is Eq. 6.3.7.

$$Q_g = -\int_0^\tau dt \left[\langle \psi_0(t)|H|\partial_\phi \psi_0(t)\rangle + c.c. \right] \tag{C.0.1}$$

The time-evolved state of the system is obtained by applying the time evolution operator to the initial state $|\psi_0(t)\rangle = U(t,t_0)\,|\psi_0\rangle$. We use this fact in the integral of Eq. C.0.1.

$$\begin{aligned} Q_g &= -\int_0^\tau dt \left[\langle \psi_0|U^\dagger(t) H|\partial_\phi \psi_0(t)\rangle + c.c. \right] = \\ &= i\int_0^\tau dt \left[\langle \psi_0|\partial_t U^\dagger(t)|\partial_\phi \psi_0(t)\rangle - c.c. \right] = \\ &= i\int_0^\tau dt \left[\langle \partial_t \psi_0(t)|\partial_\phi \psi_0(t)\rangle - c.c. \right] \end{aligned} \tag{C.0.2}$$

From the first to second line we used the Schrödinger equation for the time evolution operator,

$$i\partial_t \hat{U}(t) = \hat{H}(t)\hat{U}(t) \quad \rightarrow \quad -i\partial_t \hat{U}^\dagger(t) = \hat{U}^\dagger(t)\hat{H}(t) \tag{C.0.3}$$

and from the second to third line we used the time derivative of the time-evolved state,

$$\partial_t\,|\psi_0(t)\rangle = |\partial_t \psi_0(t)\rangle = \partial_t U(t)\,|\psi_0\rangle \quad \rightarrow \quad \langle \partial_t \psi_0(t)| = \langle \psi_0|\,\partial_t U^\dagger(t) \tag{C.0.4}$$

Now, we proceed as follows,

$$\begin{aligned} Q_g &= i\int_0^\tau dt \left[\langle \partial_t \psi_0(t)|\partial_\phi \psi_0(t)\rangle - \langle \partial_t \psi_0(t)|\partial_\phi \psi_0(t)\rangle \right] = \\ &= i\partial_\phi \int_0^\tau dt\ \langle \partial_t \psi_0(t)|\psi_0(t)\rangle = \\ &= -i\partial_\phi \int_0^\tau dt\ \langle \psi_0(t)|\partial_t \psi_0(t)\rangle = -\partial_\phi \gamma_0(\phi) \end{aligned} \tag{C.0.5}$$

where in the first to second line we used the product rule of derivatives twice,

$$\partial_\phi \langle \partial_t \psi_0(t)|\psi_0(t)\rangle = \langle \partial_\phi \partial_t \psi_0(t)|\psi_0(t)\rangle + \langle \partial_t \psi_0(t)|\partial_\phi \psi_0(t)\rangle \tag{C.0.6}$$

$$\partial_t \langle \partial_\phi \psi_0(t)|\psi_0(t)\rangle = \langle \partial_t \partial_\phi \psi_0(t)|\psi_0(t)\rangle + \langle \partial_\phi \psi_0(t)|\partial_t \psi_0(t)\rangle \tag{C.0.7}$$

and in the second to third line we used $\int_0^\tau dt\, \partial_t \langle \partial_\phi \psi_0(t) | \psi_0(t) \rangle = 0$.

Finally we obtain the pumped charge as the derivative of the geometric phase acquired by a evolving the ground state, with respect to the superconducting phase bias.

Bibliography

[1] I. M. Georgescu, S. Ashhab, and Franco Nori. "Quantum simulation". In: Rev. Mod. Phys. 86 (1 Mar. 2014), pp. 153–185. DOI: 10.1103/RevModPhys.86.153. URL: https://link.aps.org/doi/10.1103/RevModPhys.86.153.

[2] Francesco Tacchino et al. "Quantum Computers as Universal Quantum Simulators: State-of-the-Art and Perspectives". In: Advanced Quantum Technologies 3.3 (Dec. 2019), p. 1900052. DOI: 10.1002/qute.201900052. URL: https://doi.org/10.1002%2Fqute.201900052.

[3] Richard P. Feynman. "Simulating physics with computers". In: International Journal of Theoretical Physics 21.6 (June 1982), pp. 467–488. ISSN: 1572-9575. DOI: 10.1007/BF02650179. URL: https://doi.org/10.1007/BF02650179.

[4] Immanuel Bloch, Jean Dalibard, and Wilhelm Zwerger. "Many-body physics with ultracold gases". In: Rev. Mod. Phys. 80 (3 July 2008), pp. 885–964. DOI: 10.1103/RevModPhys.80.885. URL: https://link.aps.org/doi/10.1103/RevModPhys.80.885.

[5] Roberta Citro and Monika Aidelsburger. "Thouless pumping and topology". In: Nature Reviews Physics 5.2 (Feb. 2023), pp. 87–101. ISSN: 2522-5820. DOI: 10.1038/s42254-022-00545-0. URL: https://doi.org/10.1038/s42254-022-00545-0.

[6] Yongguan Ke et al. "Topological phase transitions and Thouless pumping of light in photonic waveguide arrays". In: Laser & Photonics Reviews 10.6 (2016), pp. 995–1001. DOI: https://doi.org/10.1002/lpor.201600119. eprint: https://onlinelibrary.wiley.com/doi/pdf/10.1002/lpor.201600119. URL: https://onlinelibrary.wiley.com/doi/abs/10.1002/lpor.201600119.

[7] T. Hensgens et al. "Quantum simulation of a Fermi–Hubbard model using a semiconductor quantum dot array". In: Nature 548.7665 (Aug. 2017), pp. 70–73. ISSN: 1476-4687. DOI: 10.1038/nature23022. URL: https://doi.org/10.1038/nature23022.

[8] C. J. van Diepen et al. "Quantum Simulation of Antiferromagnetic Heisenberg Chain with Gate-Defined Quantum Dots". In: Phys. Rev. X 11 (4 Nov. 2021), p. 041025. DOI: 10.1103/PhysRevX.11.041025. URL: https://link.aps.org/doi/10.1103/PhysRevX.11.041025.

[9] Yuriy Makhlin, Gerd Schön, and Alexander Shnirman. "Quantum-state engineering with Josephson-junction devices". In: Rev. Mod. Phys. 73 (2 May 2001), pp. 357–400. DOI: 10.1103/RevModPhys.73.357. URL: https://link.aps.org/doi/10.1103/RevModPhys.73.357.

[10] Rosario Fazio and Herre van der Zant. "Quantum phase transitions and vortex dynamics in superconducting networks". In: Physics Reports 355.4 (2001), pp. 235–334. ISSN: 0370-1573. DOI: https://doi.org/10.1016/S0370-1573(01)00022-9. URL: https://www.sciencedirect.com/science/article/pii/S0370157301000229.

[11] L. I. Glazman and A. I. Larkin. "New Quantum Phase in a One-Dimensional Josephson Array". In: Phys. Rev. Lett. 79 (19 Nov. 1997), pp. 3736–3739. DOI: 10.1103/PhysRevLett.79.3736. URL: https://link.aps.org/doi/10.1103/PhysRevLett.79.3736.

[12] D. J. Thouless. "Quantization of particle transport". In: Phys. Rev. B 27 (10 May 1983), pp. 6083–6087. DOI: 10.1103/PhysRevB.27.6083. URL: https://link.aps.org/doi/10.1103/PhysRevB.27.6083.

[13] Richard F. Voss and Richard A. Webb. "Macroscopic Quantum Tunneling in 1-μm Nb Josephson Junctions". In: Phys. Rev. Lett. 47 (4 July 1981), pp. 265–268. DOI: 10.1103/PhysRevLett.47.265. URL: https://link.aps.org/doi/10.1103/PhysRevLett.47.265.

[14] C. G. L. Bøttcher et al. "Superconducting, insulating and anomalous metallic regimes in a gated two-dimensional semiconductor–superconductor array". In: Nature Physics 14.11 (Nov. 2018), pp. 1138–1144. ISSN: 1745-2481. DOI: 10.1038/s41567-018-0259-9. URL: https://doi.org/10.1038/s41567-018-0259-9.

[15] H. S. J. van der Zant et al. "Quantum phase transitions in two dimensions: Experiments in Josephson-junction arrays". In: Phys. Rev. B 54 (14 Oct. 1996), pp. 10081–10093. DOI: 10.1103/PhysRevB.54.10081. URL: https://link.aps.org/doi/10.1103/PhysRevB.54.10081.

[16] Tafuri F. Fundamentals and Frontiers of the Josephson Effect. Springer Cham, 2019.

[17] J. Shabani et al. "Two-dimensional epitaxial superconductor-semiconductor heterostructures: A platform for topological superconducting networks". In: Phys. Rev. B 93 (15 Apr. 2016), p. 155402. DOI: 10.1103/PhysRevB.93.155402. URL: https://link.aps.org/doi/10.1103/PhysRevB.93.155402.

[18] H. Moon et al. "Machine learning enables completely automatic tuning of a quantum device faster than human experts". In: Nature Communications 11.1 (Aug. 2020), p. 4161. ISSN: 2041-1723. DOI: 10.1038/s41467-020-17835-9. URL: https://doi.org/10.1038/s41467-020-17835-9.

[19] B. L. Altshuler and L. I. Glazman. "Pumping Electrons". In: Science 283.5409 (1999), pp. 1864–1865. DOI: 10.1126/science.283.5409.1864. eprint: https://www.science.org/doi/pdf/10.1126/science.283.5409.1864. URL: https://www.science.org/doi/abs/10.1126/science.283.5409.1864.

[20] Archimedean screw. https://mechstuff.com/amazing-archimedean-screw/. Accessed: 28-04-2023.

[21] Thouless pumps and winding invariant. https://topocondmat.org/w3_pump_QHE/pumps.html. Accessed: 27-04-2023.

[22] M. V. Berry. "Quantal Phase Factors Accompanying Adiabatic Changes". In: Proceedings of the Royal Society of London. Series A, Mathematical and Physical Sciences 392.1802 (1984), pp. 45–57. ISSN: 00804630. URL: http://www.jstor.org/stable/2397741 (visited on 04/24/2023).

[23] D. J. Thouless et al. “Quantized Hall Conductance in a Two-Dimensional Periodic Potential”. In: Phys. Rev. Lett. 49 (6 Aug. 1982), pp. 405–408. DOI: 10.1103/PhysRevLett.49.405. URL: https://link.aps.org/doi/10.1103/PhysRevLett.49.405.

[24] Qian Niu, D. J. Thouless, and Yong-Shi Wu. “Quantized Hall conductance as a topological invariant”. In: Phys. Rev. B 31 (6 Mar. 1985), pp. 3372–3377. DOI: 10.1103/PhysRevB.31.3372. URL: https://link.aps.org/doi/10.1103/PhysRevB.31.3372.

[25] Q Niu and D J Thouless. “Quantised adiabatic charge transport in the presence of substrate disorder and many-body interaction”. In: Journal of Physics A: Mathematical and General 17.12 (Aug. 1984), p. 2453. DOI: 10.1088/0305-4470/17/12/016. URL: https://dx.doi.org/10.1088/0305-4470/17/12/016.

[26] M. Aunola and J. J. Toppari. “Connecting Berry’s phase and the pumped charge in a Cooper pair pump”. In: Phys. Rev. B 68 (2 July 2003), p. 020502. DOI: 10.1103/PhysRevB.68.020502. URL: https://link.aps.org/doi/10.1103/PhysRevB.68.020502.

[27] Matteo M. Wauters et al. “Localization, Topology, and Quantized Transport in Disordered Floquet Systems”. In: Phys. Rev. Lett. 123 (26 Dec. 2019), p. 266601. DOI: 10.1103/PhysRevLett.123.266601. URL: https://link.aps.org/doi/10.1103/PhysRevLett.123.266601.

[28] Lorenzo Privitera et al. “Nonadiabatic Breaking of Topological Pumping”. In: Phys. Rev. Lett. 120 (10 Mar. 2018), p. 106601. DOI: 10.1103/PhysRevLett.120.106601. URL: https://link.aps.org/doi/10.1103/PhysRevLett.120.106601.

[29] M. J. Rice and E. J. Mele. “Elementary Excitations of a Linearly Conjugated Diatomic Polymer”. In: Phys. Rev. Lett. 49 (19 Nov. 1982), pp. 1455–1459. DOI: 10.1103/PhysRevLett.49.1455. URL: https://link.aps.org/doi/10.1103/PhysRevLett.49.1455.

[30] Iliya Esin et al. “Quantized transport and steady states of Floquet topological insulators”. In: Phys. Rev. B 97 (24 June 2018), p. 245401. DOI: 10.1103/PhysRevB.97.245401. URL: https://link.aps.org/doi/10.1103/PhysRevB.97.245401.

[31] Frederik Nathan et al. “Anomalous Floquet insulators”. In: Phys. Rev. B 99 (19 May 2019), p. 195133. DOI: 10.1103/PhysRevB.99.195133. URL: https://link.aps.org/doi/10.1103/PhysRevB.99.195133.

[32] Pedro Ponte et al. “Many-Body Localization in Periodically Driven Systems”. In: Phys. Rev. Lett. 114 (14 Apr. 2015), p. 140401. DOI: 10.1103/PhysRevLett.114.140401. URL: https://link.aps.org/doi/10.1103/PhysRevLett.114.140401.

[33] C. W. J. Beenakker. “Universal limit of critical-current fluctuations in mesoscopic Josephson junctions”. In: Phys. Rev. Lett. 67 (27 Dec. 1991), pp. 3836–3839. DOI: 10.1103/PhysRevLett.67.3836. URL: https://link.aps.org/doi/10.1103/PhysRevLett.67.3836.

[34] Lucas Casparis et al. “Superconducting gatemon qubit based on a proximitized two-dimensional electron gas”. In: Nature Nanotechnology 13.10 (Oct. 2018), pp. 915–919. ISSN: 1748-3395. DOI: 10.1038/s41565-018-0207-y. URL: https://doi.org/10.1038/s41565-018-0207-y.

[35] Elliott Lieb, Theodore Schultz, and Daniel Mattis. “Two soluble models of an antiferromagnetic chain”. In: Annals of Physics 16.3 (1961), pp. 407–466. ISSN: 0003-4916. DOI: https://doi.org/10.1016/0003-4916(61)90115-4. URL: https://www.sciencedirect.com/science/article/pii/0003491661901154.

[36] Piers Coleman. Introduction to Many-Body Physics. Cambridge University Press, 2015. DOI: 10.1017/CBO9781139020916.

[37] G. Floquet. “Sur les équations différentielles linéaires à coefficients périodiques”. fr. In: Annales scientifiques de l’École Normale Supérieure 2e série, 12 (1883), pp. 47–88. DOI: 10.24033/asens.220. URL: http://www.numdam.org/articles/10.24033/asens.220/.

[38] G. E. Santoro. Introduction to Floquet. SISSA, Trieste, 2017.

[39] N. W. Ashcroft and N. D. Mermin. Solid State Physics. Holt-Saunders, 1976.

[40] Martin Holthaus. “Floquet engineering with quasienergy bands of periodically driven optical lattices”. In: Journal of Physics B: Atomic, Molecular and Optical Physics 49.1 (Nov. 2015), p. 013001. DOI: 10.1088/0953-4075/49/1/013001. URL: https://doi.org/10.1088%2F0953-4075%2F49%2F1%2F013001.

[41] Mark S. Rudner and Netanel H. Lindner. “The Floquet Engineer’s Handbook”. In: (2020). arXiv: 2003.08252 [cond-mat.mes-hall].

[42] Takashi Oka and Sota Kitamura. “Floquet Engineering of Quantum Materials”. In: Annual Review of Condensed Matter Physics 10.1 (2019), pp. 387–408. DOI: 10.1146/annurev-conmatphys-031218-013423. eprint: https://doi.org/10.1146/annurev-conmatphys-031218-013423. URL: https://doi.org/10.1146/annurev-conmatphys-031218-013423.

[43] Michael Lohse et al. “Exploring 4D quantum Hall physics with a 2D topological charge pump”. In: Nature 553.7686 (Jan. 2018), pp. 55–58. ISSN: 1476-4687. DOI: 10.1038/nature25000. URL: https://doi.org/10.1038/nature25000.

[44] M. M. Wauters. Adiabatic approaches to non-equilibrium systems: Topology, Optimization and learning. SISSA, Trieste, 2020.

[45] A. L. C. Hayward et al. “Effect of disorder on topological charge pumping in the Rice-Mele model”. In: Phys. Rev. A 103 (4 Apr. 2021), p. 043310. DOI: 10.1103/PhysRevA.103.043310. URL: https://link.aps.org/doi/10.1103/PhysRevA.103.043310.

[46] G. E. Santoro. Introduction to topological insulators. SISSA, Trieste, 2017.

[47] Y. Aharonov and D. Bohm. “Significance of Electromagnetic Potentials in the Quantum Theory”. In: Phys. Rev. 115 (3 Aug. 1959), pp. 485–491. DOI: 10.1103/PhysRev.115.485. URL: https://link.aps.org/doi/10.1103/PhysRev.115.485.

[48] Mark S. Rudner and Netanel H. Lindner. “Band structure engineering and non-equilibrium dynamics in Floquet topological insulators”. In: Nature Reviews Physics 2.5 (May 2020), pp. 229–244. ISSN: 2522-5820. DOI: 10.1038/s42254-020-0170-z. URL: https://doi.org/10.1038/s42254-020-0170-z.

[49] Netanel H. Lindner, Erez Berg, and Mark S. Rudner. “Universal Chiral Quasisteady States in Periodically Driven Many-Body Systems”. In: Phys. Rev. X 7 (1 Feb. 2017), p. 011018. DOI: 10.1103/PhysRevX.7.011018. URL: https://link.aps.org/doi/10.1103/PhysRevX.7.011018.

[50] Paolo A. Erdman et al. “Fast and accurate Cooper pair pump”. In: Phys. Rev. B 100 (23 Dec. 2019), p. 235428. DOI: 10.1103/PhysRevB.100.235428. URL: https://link.aps.org/doi/10.1103/PhysRevB.100.235428.

[51] Raffaello Bianco and Raffaele Resta. “Mapping topological order in coordinate space”. In: Phys. Rev. B 84 (24 Dec. 2011), p. 241106. DOI: 10.1103/PhysRevB.84.241106. URL: https://link.aps.org/doi/10.1103/PhysRevB.84.241106.

[52] Yi-Zhuang You et al. “Wave Function and Strange Correlator of Short-Range Entangled States”. In: Phys. Rev. Lett. 112 (24 June 2014), p. 247202. DOI: 10.1103/PhysRevLett.112.247202. URL: https://link.aps.org/doi/10.1103/PhysRevLett.112.247202.

[53] Luca Lepori et al. “Strange correlators for topological quantum systems from bulk-boundary correspondence”. In: (2022). arXiv: 2209.04283 [cond-mat.str-el].

[54] Haruki Watanabe. “Insensitivity of bulk properties to the twisted boundary condition”. In: Phys. Rev. B 98 (15 Oct. 2018), p. 155137. DOI: 10.1103/PhysRevB.98.155137. URL: https://link.aps.org/doi/10.1103/PhysRevB.98.155137.

[55] Mikko Möttönen et al. “Measurement scheme of the Berry phase in superconducting circuits”. In: Phys. Rev. B 73 (21 June 2006), p. 214523. DOI: 10.1103/PhysRevB.73.214523. URL: https://link.aps.org/doi/10.1103/PhysRevB.73.214523.

[56] W. P. Su, J. R. Schrieffer, and A. J. Heeger. “Solitons in Polyacetylene”. In: Phys. Rev. Lett. 42 (25 June 1979), pp. 1698–1701. DOI: 10.1103/PhysRevLett.42.1698. URL: https://link.aps.org/doi/10.1103/PhysRevLett.42.1698.